Photoproduction of the $K^+K^-(1750)$

A Dissertation

Presented for the

Doctor of Philosophy Degree

The University of Tennessee, Knoxville

Ryan Edward Mitchell

December 2003

Acknowledgments

This work benefited greatly from the help, the time, the effort, and the thoughts of many people. I would first like to thank my dissertation committee – Tom Handler, Ted Barnes, Bill Bugg, Yuri Kamyshkov, and Hap McSween – for their time and interest and for their patience in seeing this project through to its end. I would especially like to thank Tom for his patience over the years, his willingness to give advice on any subject, and for his confidence in me, giving me the freedom, whenever I have wanted it, to pursue things in my own sometimes nontraditional way.

Almost needless to say, this work wouldn't have amounted to anything without the FOCUS Collaboration at Fermilab, who had already nearly completely gathered such an impressive and clean and well-understood data sample when I was only beginning my graduate studies. The many suggestions during collaboration meetings have proved invaluable, and have, in fact, laid the foundations for much of this work. I especially need to thank John Cumalat and the paper committee – Med Webster, Stefano Bianco, Peter Garbincius, and Hector Mendez – for their help and for their special interest in this type of diffractive physics.

I should also single out a few theorists who I have worked with most closely, especially Ted Barnes. I wouldn't have been brave enough to take on such a project as this without knowing that Ted's expertise was only a few steps down the hall. I would also like to thank Philip Page, whose brief stay in Tennessee was during one of the most formative periods of the evolution of this work; and I shouldn't forget Noel Black, who was once

forced to give me a lecture on the Flux Tube on the way to the mountains.

Much of the research presented here on the history of photoproduction was done on the floor of the physics library at the University of Milan. I'm grateful to the physics group there, especially Luigi Moroni, Daniele Pedrini, Dario Menasce, and Sandra Malvezzi, for the invitation to work with them, for teaching me something about the K-Matrix, and for the hospitality while I was there. I would also like to thank the Frascati group – Stefano Bianco, Rinaldo Baldini, and Adriano Zallo – for fruitful discussions during my short stay in Frascati. The Frascati enthusiasm for light quark physics served as a sort of inspiration at a time when I needed it.

As for the many friends who have made bearable some of the hardest times of these past few years, I can't begin to express my gratitude. I could write pages and say nothing. So, confining myself to whatever I can manage to write during the course of one very long, overexaggerated, dedicatory sigh, I remember a few fragments... coming home to the lights on and finding Banu and David still awake; sampling peppermint and watermelon on the fifth floor, not bad; a wine glass thrown from my balcony with tears; Tuesdays with Sara; the red wine and chocolate cake of roommate night Wednesdays; study parties turned study caravans, trudging down Cumberland at three in the morning; running up Lead Cove and Tomato Head afterwards; Max Patch on a whim with a girl in a skirt, reading Sylvia Plath; wine on Gardner; breakfast at Cosmo's; Poe at Jake's; the side of a highway in Georgia; hiking with Mitra; sleeping in Ezzy; picking Gingko leaves; looping always, morning, night, afternoons, alone, or with

you; the particular retardedness and stupidity of certain p's and q's; and road trips unending, Athens with Lara, Florida with David, Charleston with Adriel, New York City with Jake, Boone with Sara, "camping" with Keith and Banu, San Francisco with Noel, Portland with Demet, Philadelphia with Shana, Chapel Hill with Kim, Chicago with Curtis, Minneapolis with Devora... I owe more than I can give.

Finally, I would like to thank my parents, who have always been there, and who have always supported me no matter what path I have chosen, however roundabout it might be.

Abstract

While photoproduction has often been advertised as an important environment in which to study light meson spectroscopy, solid experimental results are sparse. In fact, beyond the relatively straightforward photoproduction of the ρ, ω, and ϕ mesons, the few results of exclusive photoproduction that do exist are poorly understood, and several, perhaps, have even been misinterpreted. After extensively reviewing the sometimes tenuous history of the exclusive photoproduction of the "$\rho'(1600)$," the "$\omega\pi^0(1250)$," the "$\omega(1650)$," and the "$K^+K^-(1750)$," new results from the E831/FOCUS photoproduction experiment at Fermilab are presented which address the interpretation of the $K^+K^-(1750)$. This enhancement in low-p_T K^+K^- pairs at a mass near $1750\,\mathrm{MeV/c^2}$ has been observed by several previous photoproduction experiments, but, despite several apparent inconsistencies, it has always been interpreted as the $J^{PC} = 1^{--}$ $\phi(1680)$ meson. With nearly two orders of magnitude more events than any previous observation of the $K^+K^-(1750)$, and based on precise measurements of its mass and width, and its absence from the K^*K final state, the FOCUS data can finally render this interpretation implausible. In addition, several steps have been taken towards establishing a new interpretation. Based on limited angular analyses of its decay and the beam energy dependence of its production, we argue that, in the absence of any wild interference scenarios, the $K^+K^-(1750)$ has $J^{PC} \neq 1^{--}$, and, in fact, the most likely assignment appears to be 2^{++}. It is hoped that this work can help set the stage for future reevaluations and new insights in photoproduction.

Contents

List of Tables

List of Figures

Chapter 1

Introduction

The spectroscopy of light mesons has always held a special place in the evolution of particle physics, that branch of physics aiming to understand the elementary particles and the forces between them. From the discovery of pions in the 1940's and their role in the initial articulations of the strong force to the advent of the idea of quarks in the 1960's to the current push to understand the mechanisms of quark confinement, light mesons have continuously played a fundamental role in extending the frontiers of physics. The past few years have seen enormous progress with the potential discoveries of the first glueball and hybrid meson states, including the $f_0(1500)$ glueball candidate and the $\pi_1(1600)$ hybrid with exotic $J^{PC} = 1^{-+}$, states explicitly manifesting gluonic degrees of freedom. Further discoveries in this vein are expected to shed even more light on the perpetual problems associated with the very non-linear aspects of the gluonic fields of the strong force.

For years, photoproduction has been touted as potentially fertile ground for new discoveries in light meson spectroscopy. It is often cited as an ideal mechanism for the production of the important hybrid meson states, for example. Unfortunately, experimental knowledge concerning photoproduction is incredibly sparse, and, in fact, it appears that much of the historical work done in photoproduction has been misinterpreted. This dissertation aims to expose and remedy one such misinterpretation, hopefully setting the stage for future reevaluations and new insights in photoproduction.

Using data from the E831/FOCUS experiment at Fermilab, we report on an enhancement at a mass of 1750 $\mathrm{MeV/c^2}$ seen in the exclusive photoproduction of low-p_T K^+K^- pairs. This enhancement has been observed by several previous photoproduction experiments during the 1980's, but, despite several apparent inconsistencies, it has always been interpreted as the $J^{PC} = 1^{--}$ $\phi(1680)$ meson, a radial excitation of the $\phi(1020)$ meson. With nearly two orders of magnitude more events than any previous observation, and based on precise measurements of the mass and width of the enhancement and its absence from the K^*K final state, the FOCUS data can finally render this interpretation implausible. Until a new interpretation is established, we will refer to the enhancement as the "$K^+K^-(1750)$."

Assuming CP conservation in the production process $\gamma N \to K^+K^-(1750)N \to K^+K^-N$, we can immediately limit the J^{PC} quantum numbers of the $K^+K^-(1750)$ to 0^{++}, 1^{--}, 2^{++}, 3^{--}, and so on. Further limiting the possible J^{PC} of the $K^+K^-(1750)$ requires either an angular analysis of the $K^+K^-(1750) \to K^+K^-$ decay or more detailed

information on the production mechanism $\gamma N \to K^+K^-(1750)N$. Unfortunately, the particular design of the FOCUS detector, a detector designed primarily for the study of charmed particles, has imposed several limitations towards this end. First, because of the inherent nature of the bremsstrahlung process in which the photon beam was generated, the direction of the incoming photon on an event by event basis contains enough uncertainty to affect our ability to measure certain important features of the production of the $K^+K^-(1750)$. Second, largely because of a vertical gap in one of the triggering elements, the angular acceptances of the detector are far from uniform, greatly complicating attempts at a full angular analysis of the $K^+K^-(1750)$ decay.

Despite these limitations imposed by the FOCUS detector, several important statements concerning the nature of the $K^+K^-(1750)$ can be made:

1. Because of inconsistencies in mass and branching ratios to K^*K, the $K^+K^-(1750)$ cannot be the $\phi(1680)$.

2. The beam energy dependence of the photoproduction of the $K^+K^-(1750)$ differs from the beam energy dependence of the photoproduction of the $\phi(1020)$.

3. Several different methods for probing the angular structure of the $K^+K^-(1750)$ decay show results inconsistent with a 1^{--} assignment for the $K^+K^-(1750)$, and point more towards a 2^{++} assignment.

These three statements, combined with the non-observation of the $K^+K^-(1750)$ state in e^+e^- annihilation, lead us to conclude that, in the absence of any wild interference

scenarios, the $K^+K^-(1750)$ has $J^{PC} \neq 1^{--}$, and, in fact, it appears likely that the correct J^{PC} assignment is 2^{++}.

How such a 2^{++} state could be photoproduced is yet to be understood. Also uncertain is the status of the $K^+K^-(1750)$ state within the quark model. Both questions lie outside the scope of this work, and remain open for future discussions.

*****

Before presenting the details of the photoproduction of the $K^+K^-(1750)$, some general introductions must be made. Chapter 2 will serve as an introduction to the field of light meson spectroscopy, providing an outline of its history and its importance for the larger program of understanding the strong force and the confinement of quarks. Special attention will be given to the quark model and QCD and the way they have interacted to inspire a range of hadronic models, nearly all of which predict non-conventional meson states with gluonic degrees of freedom, the hybrid mesons and the glueballs.

After being briefly introduced in chapter 2, exclusive photoproduction and its importance for light meson spectroscopy will be discussed in more detail in chapter 3. Historical results in the exclusive photoproduction of light mesons, and how these results present problems for anyone attempting to interpret them, will be considered at length. The history of the photoproduction of the $K^+K^-(1750)$ and how it came to be erroneously known as the $\phi(1680)$ will be introduced as one of four case studies in the history of exclusive photoproduction.

Chapter 4 will then introduce the E831/FOCUS experiment at Fermilab, an experi-

ment which has the potential to greatly improve our currently incomplete understanding of exclusive photoproduction. Aspects of the FOCUS spectrometer that are relevant to the study of the $K^+K^-(1750)$ will be presented in some detail, e.g., the excellent particle identification capabilities and precise tracking system. In addition, important aspects of the triggering system and data collection will be explained.

General properties of the photon beam will be presented in chapter 5. Knowing the parameters of the photon beam with some precision is crucial for several parts of the $K^+K^-(1750)$ analysis. How these parameters are measured and estimates for their uncertainties will be covered exhaustively.

Once the beam parameters and their uncertainties are known, chapter 6 will then present the results of a variety of Monte Carlo simulations aiming to understand the resolutions and acceptances of the FOCUS detector. Resolutions of all the basic parameters of the $K^+K^-(1750)$ analysis will be presented. While the mass resolution is superb, it will be found that the uncertainty in beam direction greatly affects the p_T^2 (transverse momentum squared) distributions of K^+K^- events, as well as effectively smearing the azimuthal angle distribution of the $K^+K^-(1750)$ decay. After resolutions are presented, acceptances will be considered, where we will find uniform acceptances in all of the K^+K^- parameters except the decay angles, which will be found to be sculpted quite dramatically by the vertical slit in the H$\times$V trigger.

Finally, after all of the above preliminaries, chapter 7 will show striking evidence for the $K^+K^-(1750)$ in the FOCUS data. The mass and width of the $K^+K^-(1750)$ will

be measured to be $1753.5 \pm 1.5 \pm 2.3\,\mathrm{MeV/c^2}$ and $122.2 \pm 6.2 \pm 8.0\,\mathrm{MeV/c^2}$, respectively. In addition, a search for the $K^+K^-(1750)$ in the K^*K final state will be conducted and tight upper limits for the branching ratio $\Gamma(K^+K^-(1750) \to K^*K)/\Gamma(K^+K^-(1750) \to K^+K^-)$ will be set. Based on the dramatic inconsistencies between their masses and branching ratios, it will be concluded that the $K^+K^-(1750)$ cannot be the $\phi(1680)$, arguing against the standard interpretation and opening the door to a variety of different possibilities.

Chapter 8 then takes up the description of the production characteristics of the $K^+K^-(1750)$, showing that the $K^+K^-(1750)$ is only produced at very low transverse momentum, and presenting evidence that the beam energy dependence of the production of the $K^+K^-(1750)$ rises with respect to the $\phi(1020)$ production. This beam energy dependence will serve as an important indication that the $K^+K^-(1750)$ is most likely not being produced in the same manner as the well-understood ground state vectors, the $\rho(770)$, $\omega(782)$, and $\phi(1020)$, and will further validate the suspicion that the $K^+K^-(1750)$ has $J^{PC} \neq 1^{--}$.

The question of the J^{PC} quantum numbers of the $K^+K^-(1750)$ is taken up more directly in chapter 9, where various methods will be used to tackle the angular structure of the $K^+K^-(1750)$ decay. While a full partial wave analysis is not feasible due to various limitations of the FOCUS detector, many suggestive results with limited angular analyses will be found. Two different methods will point towards a 2^{++} interpretation for the $K^+K^-(1750)$.

Chapter 2

Light Meson Spectroscopy

The Standard Model of particle physics[1], describing the elementary particles and their interactions, has survived, relatively unscathed, over twenty years of testing, articulation, and criticism. In fact, Quantum Electrodynamics (QED), the Standard Model theory of the electromagnetic force, has often been hailed as the most successful, most precise, and best tested theory ever to be constructed by mankind. And not far behind QED, the Standard Model description of the weak force, while harder to test than QED because of the relative weakness of the weak force, has shown equally few vulnerabilities.

By contrast, the strong force, the force responsible for binding quarks into hadrons and hadrons into nuclei, has proved more difficult to describe, at best, and nearly intractable, at worst. The strong force has not only proved problematic in itself, but has

[1]For a brief introduction to the Standard Model and for tables of properties of the elementary particles, refer to appendix A. For more detailed information on the Standard Model and the field of particle physics in general, see references [1, 2, 3, 4, 5].

also posed problems for the study of the other forces whenever those studies encounter hadrons, e.g., in non-leptonic weak decays. The problems stem precisely from the fact that the Standard Model describes the strong force on the level of quarks and gluons, while experiments only observe composites of quarks and gluons, hadrons. Thus, a good understanding of hadrons and their quark and gluonic content is invaluable. While the Standard Model theory of the strong force, Quantum Chromodynamics (QCD), has been reasonably successful at describing higher momentum phenomena where quarks are effectively free within hadrons and perturbative expansions in α_s are valid[2], the nonperturbative regime is plagued by complexity. In this regime, quarks and gluons are tightly bound within hadrons, and QCD becomes so nonlinear that one most often must resort to specific hadronic models.

It is in this complex nonperturbative regime of QCD that light meson spectroscopy contributes. If one is to have a full understanding of the strong force, one must know the physical states, the hadrons, into which the strong force binds quarks and gluons. The most basic role of experimental hadron spectroscopy is simply to observe and classify these states. Light meson spectroscopy is a branch of hadron spectroscopy that deals with mesons composed of the three lightest quarks (the up, down, and strange quarks) and their antiparticles. This chapter will serve as a brief introduction to light meson spectroscopy, its history and origins, its methodology, and how it hopes to contribute to a fuller understanding of the strong force and QCD.

[2]The coupling constant of the strong force, α_s, must be significantly less than one for a perturbative expansion to be meaningful. At small distances, or large momenta, α_s satisfies this perturbative requirement.

2.1 The Quark Model

Ever since its origins in the early 1960's, the quark model has stood at the heart of hadron spectroscopy, classifying hadrons according to their quark content. Mesons in the quark model (e.g., pions and kaons) are quark-antiquark ($q\overline{q}$) pairs; baryons (e.g., protons and neutrons) are composed of three quarks (qqq). Even after the emergence of the more general and currently accepted theory of the strong force, QCD, which predicts hadron states beyond the quark model, the quark model has continued to play a fundamental role as a simple guide, a template, for the classification of hadrons. Discrepancies with the quark model serve as a powerful indicator for more "non-conventional" states, like the hybrid mesons – conventional mesons with an extra gluonic degree of freedom ($q\overline{q}g$), or the glueballs – meson states composed only of gluons (gg), both types of non-$q\overline{q}$ meson states being predicted by QCD and the models inspired by it.

To appreciate the functionality of the quark model, a model that has remained remarkably stable in its main features over the past 40 years, it will be useful to briefly trace its historical evolution[3]. Before the era of QCD, the quark model evolved in roughly three stages: an era of classification (1960 – 1964), culminating in the triumphant discovery of the Ω^- baryon; a period of dynamics (1967 – 1974), where the internal structure of hadrons was probed with high energy beams of leptons, and through which Feynman's parton model emerged and was gradually amalgamated into the quark model; and the dramatic discovery of charmonium (1974 – 1975), where the quark model

[3]For more thorough introductions to the development of the quark model and the idea of quarks and the place of quarks within the broader field of particle physics, see [6, 7, 8].

found its first real successes in quantitatively accounting for the spectrum of a given quark-antiquark system by using a simple potential model.

It was Murray Gell-Mann and George Zweig who, in 1964, realized that the rapidly growing list of "elementary particles" being discovered at the newly commissioned particle accelerators could be reduced to three, more elementary particles Gell-Mann named "quarks." While Gell-Mann and many others did not initially believe in the real material existence of the quarks, the idea of quarks was natural given the patterns emerging among the hadrons. In a manner completely analogous to the move made in the mid-nineteenth century from the periodic table of the elements to the idea of more fundamental atoms, the apparent patterns among the multifarious hadrons naturally suggested an underlying layer of more fundamental particles, the quarks[4].

A typical example of the discovery of a meson is shown in figure 2.1. Here, the K^* is seen decaying to $\overline{K}^0\pi^-$, with the $\overline{K}^0$ in turn decaying to $\pi^+\pi^-$ [10]. The momenta and energies of the decay particles, in this case the three pions $\pi^+\pi^-\pi^-$, have been measured within a detector. By the conservation of energy and momentum, the energy and momentum of the decaying particle can be calculated from the energy and momenta of the decay particles, and knowing this energy and momentum enables one to calculate mass[5]. An excess of values around a particular mass is indicative of a resonance state[6].

[4] A compilation of the early, formative theoretical papers on the quark model can be found in reference [9].

[5] Recall that the mass of a particle, m, is given by $m = (E^2 - p^2)^{\frac{1}{2}}$, where E is the energy of the particle, and p its momentum.

[6] Mesons with a very short lifetime are often called "resonances," a term that originated with scattering phenomena in atomic physics.

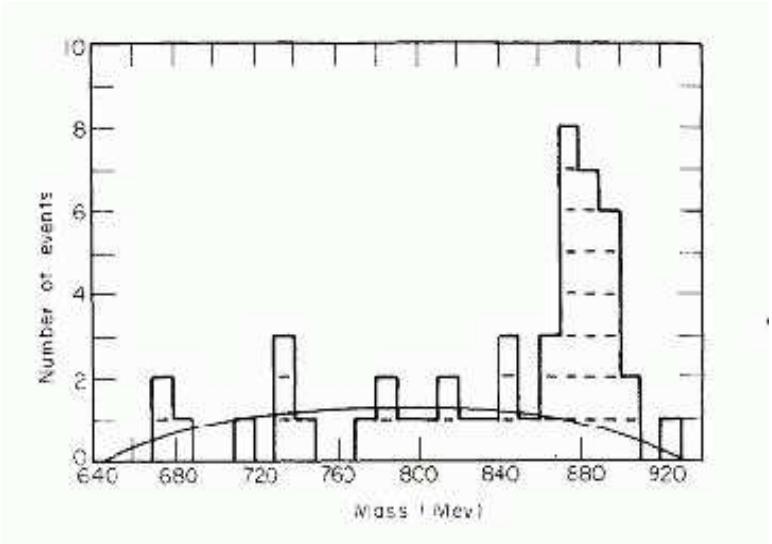

Figure 2.1: The discovery of the K^* meson. Shown is the first observation of the K^* meson (from [10]) as it was seen at the Bevatron in the reaction $K^- p \to \overline{K}^0 \pi^- p$. The mass is calculated from the measured energies and momenta of the $\overline{K}^0$ and π^- mesons. The peak in the mass spectrum signals the existence of the $K^* \to \overline{K}^0 \pi^-$ decay.

The peak in figure 2.1 is the first evidence for the K^* resonance. The width of the peak originates from Heisenberg's uncertainty principle, which states that there is a lower limit to the uncertainty in energy (in this case the meson's mass) times the uncertainty in time (in this case the meson's lifetime). So, if a particle is very short-lived – the typical lifetime of a resonance is 10^{-24} seconds – then there is inherent uncertainty in the mass of the resonance. This uncertainty in mass manifests itself as a width in the mass spectrum. In most cases, the mass shape of a decaying resonance can be described by a Breit-Wigner distribution:

$$BW(M) = \frac{\Gamma/2\pi}{(M - M_0)^2 + \Gamma^2/4}, \tag{2.1}$$

where M_0 is the mass of the resonance, and Γ is its width.

The growing list of hadrons could first be sorted according to their intrinsic spin and parity. Exploiting the conservation of angular momentum, the spin of a particle can be inferred through the angular distribution of its decay products. Hadrons with integral spin are called mesons (e.g., the spin–0 pions), and those with fractional spin are baryons (e.g., the spin–$\frac{1}{2}$ nucleons). In addition to intrinsic spin, an intrinsic parity is assigned to hadrons in order to conserve the overall parity of interactions, which is the symmetry of reflecting a coordinate system in a mirror. Thus, each hadron could be assigned a particular J^P where J is the spin of the hadron and P is its intrinsic parity. Pions, for instance, have $J^P = 0^-$ and nucleons have $J^P = \frac{1}{2}^+$.

Well before 1950, it had already been realized that there are groups of particles with

the same J^P and very similar mass but different electric charge. The proton and neutron, for example, have masses of 938.3 and 939.6 MeV/c^2, respectively. Similarly, the three pions ($\pi^{\pm}$ and π^0) differ in mass only by a few percent. Although the underlying reasons for this were yet to be understood, the concept of the isospin quantum number, which follows the same formalism as the spin quantum number, was devised to describe this phenomenon. Here, for example, protons and neutrons are particular manifestations of the same isospin-$\frac{1}{2}$ ($I = \frac{1}{2}$) particle, the nucleon. The proton has an isospin z-component of $+\frac{1}{2}$ ($I_z = +\frac{1}{2}$), and the neutron has $I_z = -\frac{1}{2}$, but other than their isospin z-components the proton and the neutron are the same with respect to the strong force, and the difference in their mass stems only from their different electric charges and thus their electromagnetic interactions. Similarly, the π^+, π^0, and π^- mesons are the $I_z = +1$, 0, and -1 manifestations of the $I = 1$ pion, respectively.

In the 1950's, when the first particle accelerators began to take data and new particles began to emerge, yet another quantum number (in addition to J^P and isospin) called strangeness was invented to describe a new class of particles that includes the kaons (mesons) and the lambda baryons. With a pion beam incident on a nucleon target, for example, kaons and lambdas could be produced, but they could only be produced in pairs. Every final state that included a kaon had to include another kaon or a lambda. For example, the reactions $\pi^- p \to \pi^- K^+ \Lambda$ and $\pi^- p \to K^+ K^- p$ were observed, but a reaction like $\pi^- p \to \pi^+ \pi^- \Lambda$ was apparently forbidden. The phenomenon became known as "associated production" and was explained by a new conservation law, the conser-

vation of strangeness. Pions and nucleons were assigned strangeness $S = 0$, and kaons and lambdas were given strangeness $S = \pm 1$, with the sign determined by convention[7]. The idea that strangeness had to be conserved in a strong reaction, as well as the fact that the number of baryons remains constant in any reaction, could accurately describe the phenomenon of associated production. When even more strange particles were discovered, e.g., the cascade baryons (Ξ), the conservation of the strangeness quantum number could be extended to them in a straightforward way.

The concepts of isospin and strangeness set the stage for the early 1960's when experimentalists were nearly overcome by new resonances (like the K^* meson discussed earlier). Grouping together particles by their J^P quantum numbers, and plotting particles according to their isospin and strangeness, definite patterns began to emerge. The 0^- and 1^- mesons, for example, appeared to come in groups of nine, called nonets. The $\frac{1}{2}^+$ and $\frac{3}{2}^+$ baryons looked like they came in groups of eight (octets) and ten (decuplets), respectively. In 1960 it was realized that the different groupings correspond to different representations of the SU(3) group of group theory[8]. Murray Gell-Mann initially called this idea the "eightfold way." The SU(3) symmetry proved useful not only for classification purposes but also to provide simple numerical relations between related processes. The origins of SU(3), however, and why hadrons appear in representations of SU(3) remained obscure.

[7]Positive kaons were given strangeness $+1$; negative kaons strangeness -1. To conserve strangeness, Λ baryons were given strangeness -1. Working from these initial assignments, and observing which reactions were experimentally allowed and which forbidden, a unique strangeness quantum number could be given to all mesons and baryons.

[8]For a compilation of theoretical papers on this idea, see reference [11].

Building on the idea that all SU(3) representations can be constructed out of the fundamental representation, Gell-Mann and Zweig, in 1964, postulated the quarks as a way to understand the groupings [9]. Three quarks were needed: up, down, and strange. Each have spin–$\frac{1}{2}$. Mesons were postulated to be combinations of a quark and an antiquark, thus capable of having intrinsic angular momentum of spin–0 or spin–1 (see figure 2.2); baryons were composed of three quarks and thus either spin–$\frac{1}{2}$ or spin–$\frac{3}{2}$ (see figure 2.3). Up quarks had an electric charge of $+2/3$; down and strange quarks had a charge of $-1/3$.

With these basic postulates, all of the patterns among the different SU(3) groupings had straightforward interpretations. The strangeness quantum number simply counted the number of strange quarks[9], and the conservation of strangeness could be interpreted as saying the number of strange quarks minus the number of antistrange quarks has to remain constant in strong interactions. Similarly, isospin became a measure of the difference between numbers of up quarks and down quarks:

$$I_z = \frac{(N_u - N_{\overline{u}}) - (N_d - N_{\overline{d}})}{2}. \tag{2.2}$$

The proton, then, became a uud composite and the neutron udd. The similarity in their masses is due to the similarity of the up and down quark masses. Similarly, the pions received the quark model assignments of $u\overline{d}$, $(u\overline{u} - d\overline{d})/\sqrt{2}$, and $d\overline{u}$ for the π^+, π^0,

[9]Technically, the strangeness of a hadron is the number of antistrange quarks it possesses minus the number of strange quarks. The sign was fixed by convention before the advent of the idea of quarks.

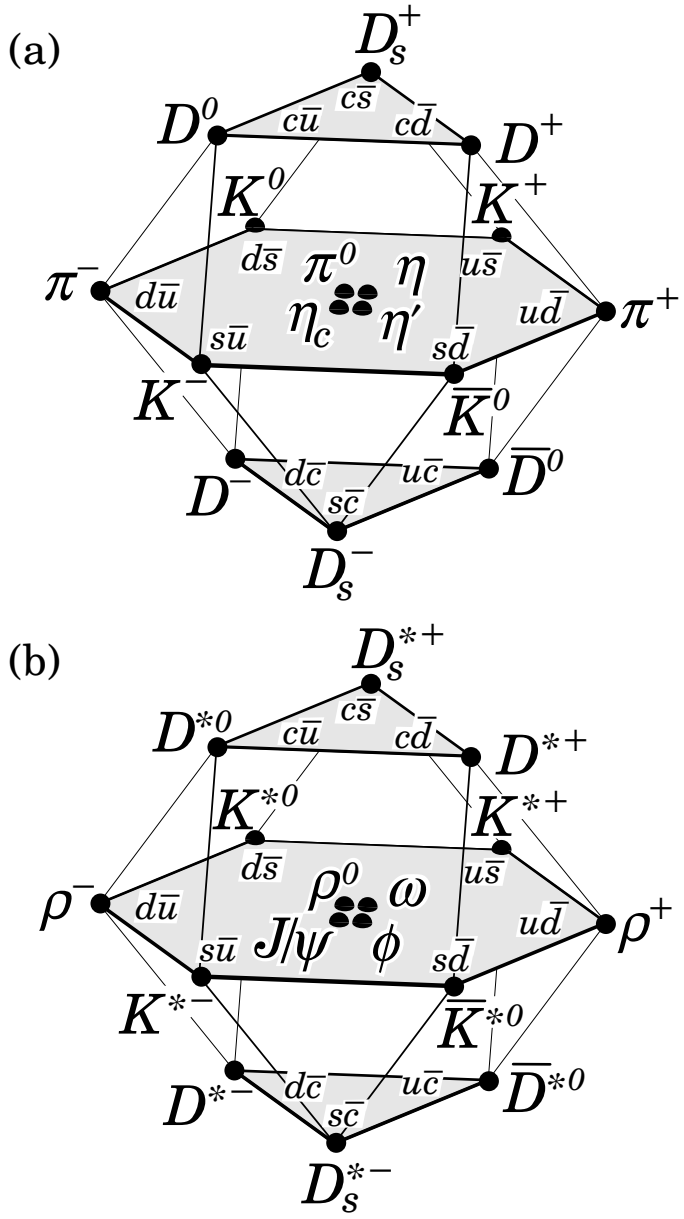

Figure 2.2: The modern mesons composed of the up, down, strange, and charm quarks. (a) The 0^- group. The original 0^- SU(3) nonet discussed in the text, which includes the pions and the kaons, is the middle level of this more general SU(4) representation. (b) The 1^- group. The original 1^- SU(3) nonet, which includes the $\rho(770)$, $\omega(782)$, and the $\phi(1020)$ to be discussed extensively in chapter 3, is the middle level of this figure.

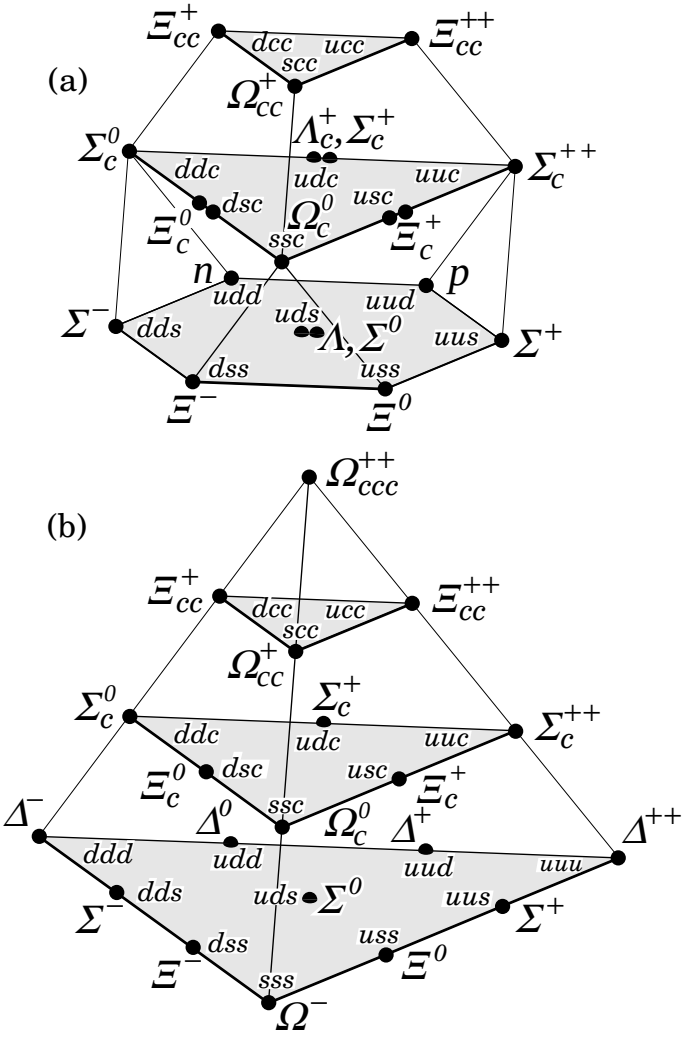

Figure 2.3: The modern baryons composed of the up, down, strange, and charm quarks. (a) The $\frac{1}{2}^+$ group. The original $\frac{1}{2}^+$ SU(3) octet that was discovered in the early 1960's, which includes the neutron and the proton, is the bottom level of this more general SU(4) representation. (b) The $\frac{3}{2}^+$ group. The original $\frac{3}{2}^+$ SU(3) decuplet, which includes the Ω^- baryon discovered in 1964, appears at the bottom level.

and π^-, respectively. The groupings of eight, nine, or ten could be understood simply by counting quarks. The meson nonets, for example, could be understood by the fact that there are nine unique ways to combine three different quarks and antiquarks into a quark-antiquark pair.

By 1964, most of the particles included in the 0^- and 1^- meson nonets, in the $\frac{1}{2}^+$ baryon octet, and in the $\frac{3}{2}^+$ baryon decuplet had been discovered experimentally. Missing states could be easily identified by experimentalists as states to look for, and were usually rapidly found. The situation resembled that of the search for new elements after the inauguration of Mendeleev's periodic table. The prediction and discovery of the Ω^- baryon in 1964 [12] with a quark assignment of sss, which was the last particle of the $\frac{3}{2}^+$ baryon decuplet to be observed, is often hailed as the first major triumph of the quark model (see figure 2.4).

A further consequence of the quark model, in addition to the classification of the ground state hadrons, is that quarks can combine into excited states, which are formed if orbital angular momentum exists between the quarks or if the quarks are in a state of radial excitation. For example, the $\phi(1020)$ meson with an $s\overline{s}$ quark assignment can exist in a state where the s and $\overline{s}$ quarks are radially excited. This form of the $\phi(1020)$ is called the $\phi(1680)$. In general, like the whole range of excited states accessible to the hydrogen atom, a given quark and antiquark will have a range of excited states. "Strangeonium" is the term employed to describe the spectrum of $s\overline{s}$ states (see figure 2.5). Also, like in the quantum mechanical description of the hydrogen atom, potential models, where some

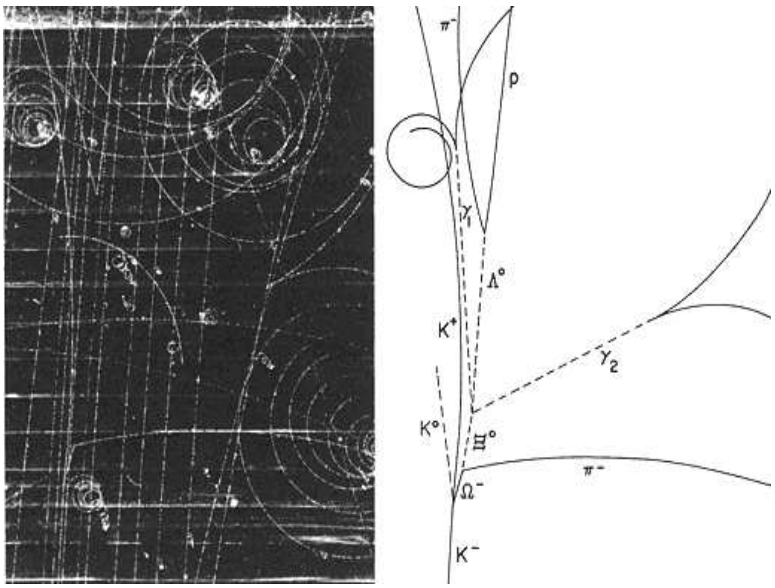

Figure 2.4: The discovery of the Ω^- baryon in 1964 (from [12]). The Ω^- appears as a very short track in a bubble chamber photograph taken at the Brookhaven National Laboratory.

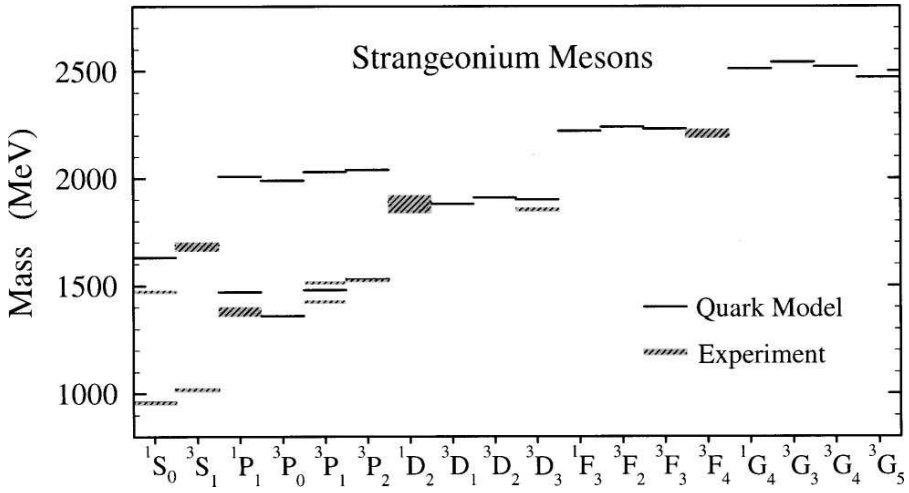

Figure 2.5: The spectrum of $s\overline{s}$ states (also known as "strangeonium," from [13]). The spectroscopic notation $^{2S+1}L_J$ is used to describe the orbital excitations between the s and $\overline{s}$ quarks. The solid lines are predictions from the relativized quark model [14, 15, 16]; and the dashed lines are experimental results.

potential exists between the s and $\overline{s}$ quarks and a Schrodinger-like equation is solved, can be used to describe the strangeonium spectrum with some qualitative success.

Given the success of the quark model in classifying the growing numbers of resonances, many groups of experimentalists set out to detect the quarks directly. If quarks existed, so experimentalists reasoned, then detecting them wouldn't be hard since their fractional electric charges would serve as a unique signature one could search for. Over twenty groups devised extensive searches using a wide variety of different techniques, but all came up empty. No free quarks could be found. Either quarks do not exist, or they only exist tightly bound within hadrons. The second option seemed unreasonable. At that time, before the concepts of confinement or QCD, tightly bound quarks could only mean that the quarks were extremely massive and had very large binding energies. In fact, several quark searches set lower limits of over 5 GeV/c^2 (over five times the proton mass) on the quark masses. By 1969, the idea of quarks, except as a pedagogical tool for understanding the formalism of SU(3), fell into disrepute.

The second stage in the pre-QCD evolution of the quark model took place from 1969 to around 1974, when the idea of quarks slowly began resurfacing in a new form within Richard Feynman's parton model. Beginning with inelastic electron-proton scattering at the Stanford Linear Accelerator, protons began to look more and more like composites of point particles, particles Feynman called "partons." As the properties of the partons were measured during the early 1970's, the partons slowly began to resemble the quarks. For example, partons were found to have spin–$\frac{1}{2}$ and fractional electric charges. These

developments softened the general resistance to the idea of quarks and added enormously to our understanding of the internal dynamics of the hadrons, but had little real direct impact on hadron spectroscopy.

The third era of the quark model began in November of 1974 with the so-called November Revolution. The J/ψ was unexpectedly discovered simultaneously by the Stanford Linear Accelerator (who called it the ψ [17]) and Brookhaven National Laboratory (who called it the J [18]). It was an extremely narrow resonance, narrower than either experiment's mass resolution, at a higher mass than anyone had ever expected to find anything so narrow, over 3 GeV/c^2. The striking discovery inspired a surge of theoretical interpretations, but the immediate favorite was that the J/ψ was a $q\overline{q}$ meson composed of a new fourth quark, the charm quark (c), and its antiquark ($\overline{c}$).

Within a year of the November Revolution a whole series of states was discovered. All were interpreted as different $c\overline{c}$ excited states, and the spectrum was called "charmonium" (figure 2.6). Potential models had been used since the first days of the quark model [9], but here, for the first time, potential models found real quantitative success. The radial part of the potential models look like:

$$V(r) \propto -\frac{4}{3}\frac{\alpha_s}{r} + br, \tag{2.3}$$

where the first term is a Coulomb-like potential and the second term is like the potential of a string, increasing the force between the quarks the farther apart they are and effectively confining them within hadrons. The constant b is the string tension. At

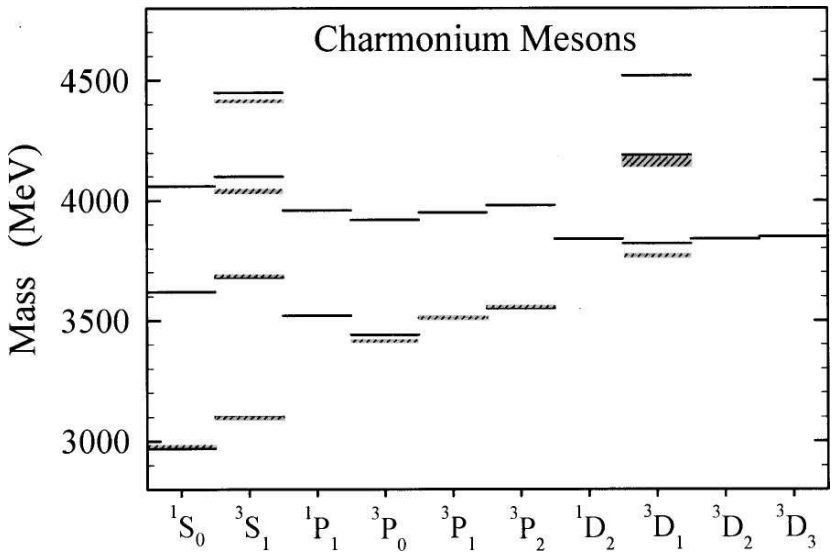

Figure 2.6: The spectrum of $c\overline{c}$ states (also known as "charmonium," from [13]). The spectroscopic notation $^{2S+1}L_J$ is used to describe the orbital excitations between the c and $\overline{c}$ quarks. The solid lines are predictions from the relativized quark model [14, 15, 16]; and the dashed lines are experimental results.

small distances between the quarks, the first term dominates and the quarks are called asymptotically free due to the weakness of the force associated with the Coulomb-like potential. At large distances, the second term holds and the quarks are confined. In addition to the radial terms, angular terms are used that can be derived in a variety of ways[10]. The mass predictions for the $c\overline{c}$ excited states from the potential models found satisfying verification from experiment.

Combined with the earlier success of SU(3) in classifying the light quark hadrons, and the newer success of the parton model, the discovery of charmonium solidified the existence of the quarks. Within ten years of the November Revolution an additional, even heavier quark was discovered, the bottom quark (b), and there was increasing confidence that a sixth quark, the top quark (t), would soon be discovered (as it was in 1995), but these discoveries did not fundamentally change the formalities of the quark model, they only added more quarks with which to work. Ever since the discovery of charm and the first real successes of the potential models, the quark model has remained substantially unchanged.

2.2 QCD

When QCD came on stage around 1973, the field of spectroscopy began to change. Rather than just considering the quarks of any hadron, there now existed a sea of gluons – the bosons mediating the strong force – and a sea of virtual quark-antiquark

[10]For much more detail on the phenomenology of light meson spectroscopy, see [13].

pairs within any hadron. The proton, for example, in addition to its three "valence" quarks uud, became a complicated swarm of strongly interacting gluons and non-valence quarks. The existence of gluons, with their properties as articulated by QCD, led to the possibility of hadrons with gluonic degrees of freedom in addition to the conventional states predicted by the quark model. As the light meson $q\overline{q}$ spectrum from the quark model began to be more and more experimentally complete, the focus of light meson spectroscopy gradually began turning towards the identification of these non-conventional states. Two large classes of non-conventional mesons have become the most sought after in light meson spectroscopy: the hybrid mesons, with a "valence" gluon in addition to the conventional $q\overline{q}$ pair; and the glueballs, states composed solely of gluons.

Before QCD, when more and more hadronic models based on the quark model were appearing, one apparent paradox was always left unresolved. No free quarks had ever been detected despite numerous searches, suggesting that quarks, if they existed, were tightly bound within hadrons. Yet, from the deep inelastic scattering experiments, it was known that quarks act essentially as if they are free inside hadrons. The $q\overline{q}$ potential of equation 2.3 described the two phenomena, confinement and asymptotic freedom, respectively, but the origins of such a potential, with a force that grows with distance, remained entirely obscure.

In 1973, it was discovered that some gauge field theories, theories based on the successful theory of QED, actually predict asymptotic freedom. This, combined with

the general resurgence of confidence in quantum field theories stemming from t'Hooft's work on renormalization and the observation of the neutral currents predicted by the new electroweak theory, led to increased optimism that a gauge field theory could be found that describes the strong force.

Around the same time, quark "color" emerged as an important idea. Quarks, according to this idea, come in three colors, and it is this "color charge" that dictates a quark's strong interactions in the same way that the electric charge of a particle is responsible for its electromagnetic interactions. Among other contemporary puzzles, the idea of color charge explained certain difficulties with π^0 decays, which had always appeared to have a cross section three times larger than predicted by theory. Furthermore, by postulating that hadrons must always be "colorless," the basic $q\overline{q}$ and qqq structure of mesons and baryons could be understood. A meson is a quark and an antiquark of the same color (a color-anticolor pair), and a baryon is a composite of three quarks of three different colors, both combinations resulting in colorless composites.

Translating color into the language of quantum field theories, we have a picture of colored quarks exchanging colored gluons. Early predictions of quantum field theories based on this rough idea were borne out in the observation of scaling violations, slight variations with Feynman's parton model when it is applied to deep inelastic scattering. These scaling violations were taken to be indicative of high momentum quarks radiating away some of their energy through the emission of gluons.

After these initial breakthroughs, the current QCD structure was quickly developed.

The modern Lagrangian of QCD is[11]:

$$\mathcal{L}_{QCD} = \overline{q_i}(i\partial_\mu \gamma^\mu \delta_{ij} - g\frac{\lambda^a_{ij}}{2} A^a_\mu \gamma^\mu - m\delta_{ij})q_j - \frac{1}{4}F^a_{\mu\nu}F^{a\mu\nu}, \tag{2.4}$$

where

$$F^{\mu\nu}_a \equiv \partial^\mu A^\nu_a - \partial^\nu A^\mu_a - g f_{abc} A^\mu_b A^\nu_c. \tag{2.5}$$

Here, q_i represents the quark fields and A^μ_a are the gluons. The structure of the QCD Lagrangian is similar to the QED Lagrangian of equation A.1 with one crucial difference: equation 2.5 contains a non-linear term in the gluon fields, whereas the corresponding QED equation, equation A.2, contains no such term for photon fields. The appearance of this non-linear term in the QCD Lagrangian allows gluons to interact with one another, making QCD a theory that is much harder to manage than QED, where the photon is incapable of interacting with other photons.

Because the coupling between quarks varies with quark momenta, becoming weaker as a quark's momentum increases (or the distance scale decreases), which accounts for asymptotic freedom, calculations based on QCD can be divided into two different regimes: perturbative, where the coupling is small enough to allow for perturbative expansions in α_s; and non-perturbative, where the coupling is large and the complicated interactions among the gluons make the theory extremely non-linear. The first dramatic evidence bearing out perturbative calculations, aside from the prediction and observa-

[11] A good introduction to the formalism of non-Abelian gauge field theories and QCD can be found in reference [5].

tion of scaling violations, came with the observation of three-jet events at the PETRA e^+e^- accelerator at the DESY laboratory in 1979 (see figure 2.7) [19, 20, 21, 22]. Two of the jets, or cones of hadrons, are the materialization of a quark and antiquark originating from the original e^+e^- annihilation of DESY. The third jet results from a gluon radiated by either the quark or antiquark. Thus, the radiated gluon, as predicted by perturbative QCD, is in a sense being directly observed.

While perturbative QCD is even presently meeting success after success in the regions where asymptotic freedom holds, progress in non-perturbative QCD, where quarks are tightly confined within hadrons, is harder to come by. Even now, nearly thirty years after the first articulations of QCD, the mechanism of quark confinement still poses problems for theorists. Although substantial progress is being made with Lattice Gauge Theory [23], a method for solving the QCD Lagrangian on a discrete space-time lattice, this method requires enormous amounts of computing time and is often used in conjunction with more phenomenological models, to be described in the next section.

Because Lattice Gauge Theory starts with the full QCD Lagrangian, lattice calculations are considered the most precise reflection of the true nature of QCD in the non-perturbative regions. One important prediction of Lattice Gauge Theory is the existence of glueball states, mesons composed entirely of gluons [24, 25]. The predicted spectrum of glueball states from a recent calculation is shown in figure 2.8. The unambiguous observation and classification of these states would greatly enhance our understanding of QCD and the non-perturbative mechanisms of quark confinement.

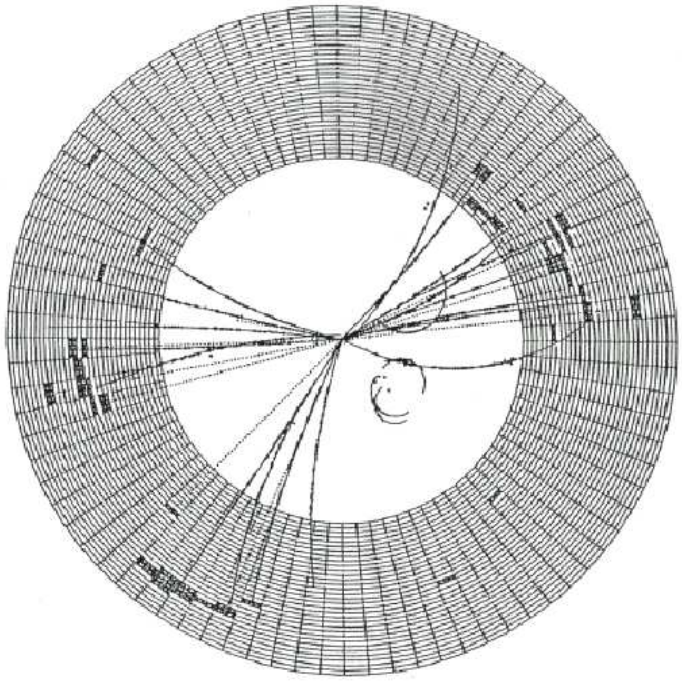

Figure 2.7: A three-jet event from the JADE detector at DESY. The electron and positron beams annihilate in the center of the detector. The three jets correspond to a quark, an antiquark, and a radiated gluon. Such events validate calculations made in perturbative QCD.

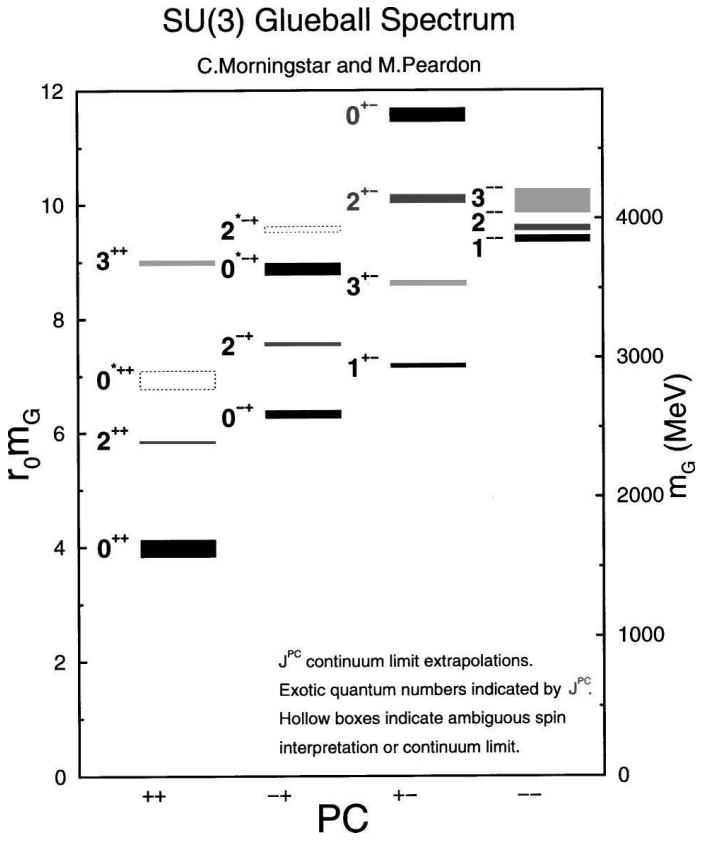

Figure 2.8: Lattice gauge theory predictions for the glueball spectrum (from [25]).

2.3 QCD-Inspired Models

Combining insights from QCD with the older quark model, a wide range of phenomenological models have been devised to improve predictions concerning light $q\overline{q}$ mesons and to study the hybrid and glueball mesons[12]. A few of these phenomenological models include the bag model [27, 28, 29, 30, 31], the constituent glue model [32], and the flux tube model [33, 34, 35]. All hadronic models have their own strengths and weaknesses, and there is little consensus among the field concerning which models are most reliable. Two different models, however, warrant special attention here because of their relevance for the work to be presented in later chapters.

The relativized quark model [14, 15, 16] is one of the oldest and perhaps most reliable of the models that describes the light $q\overline{q}$ meson spectrum. It starts with the quark model and uses a Schrodinger-like equation with a QCD-inspired potential between quark-antiquark pairs to predict the masses of the $q\overline{q}$ mesons. The radial part of the potential is the traditional one of equation 2.3. The angular part is obtained by supposing that the quark and antiquark of the meson exchange a gluon, a method termed "one-gluon exchange." The agreement between theory and experiment is generally good – see, for example, figure 2.5 – though there is certainly room for improvement.

The $^3P_0$ model is another model based on a combination of the quark model and QCD [36, 37, 38]. It has been successfully used to describe many light $q\overline{q}$ meson decays [39]. In this model, a meson decays into two other mesons through the formation of

[12]Many reviews exist that survey the vast amounts of theoretical work that has gone into understanding hadrons. See, for example, [26].

a $q\overline{q}$ pair with the quantum numbers of the vacuum[13]. When this new $q\overline{q}$ pair materializes between the original quark and antiquark of the decaying meson, the original quark of the decaying meson combines with the new antiquark and the original antiquark combines with the new quark, forming two new mesons. One recent set of calculations based on the $^3P_0$ model, predicting the decay patterns of all of the $s\overline{s}$ states [40], could be particularly relevant for the work of later chapters. Here, the $a_2(1750)$ meson is predicted to decay dominantly to K^+K^-, which could potentially inform future interpretations of the photoproduced $K^+K^-(1750)$ to be presented in chapter 7.

2.4 The Role and Methods of Spectroscopy

The role of meson spectroscopy then is simply to observe and classify meson states. A meson state can be considered understood experimentally when its mass and width have been measured precisely; its quantum numbers are known, including its J^{PC}, isospin, strangeness, etc.; the branching ratios to all of its different decay modes have been measured; and its production cross sections have been determined for all the production mechanisms in which it is produced. Other information, e.g., whether a state is a conventional $q\overline{q}$ state or a hybrid or a glueball, is gained by interpreting the above experimental results. There are several methods through which this interpretation can be done.

[13]For mesons, $P = (-1)^{L+1}$ and $C = (-1)^{L+S}$ so the quantum numbers $^{2S+1}L_J = {}^3P_0$ correspond to a J^{PC} of 0^{++}.

First, once the J^{PC} of a meson has been determined by an angular analysis[14], it can be grouped into a multiplet with other mesons of the same J^{PC}. Since the quark model predicts the nonets into which $q\overline{q}$ states ought to fall, any inconsistency can be taken as an indication of a non-$q\overline{q}$ nature of the meson. For example, according to the quark model there ought to be two isoscalar states in the 0^{++} nonet, one with $n\overline{n}$ quark content ($n\overline{n}$ is short for the appropriate combination of $u\overline{u}$ and $d\overline{d}$) and one composed of $s\overline{s}$. However, three 0^{++} isoscalar states have been observed experimentally, the $f_0(1370)$, $f_0(1500)$, and $f_0(1710)$. Combined with other information, like their branching ratios to $\pi^+\pi^-$ and K^+K^-, this overpopulation has been taken as an indication that the $f_0(1500)$ is a glueball state.

A more direct indication that a meson state is non-$q\overline{q}$ occurs when the J^{PC} of a particle is "exotic," meaning that the J^{PC} cannot possibly correspond to a $q\overline{q}$ state. The existence of exotic J^{PC} is made possible by requirements imposed by conservation laws on the J^{PC} of $q\overline{q}$ mesons:

$$P = (-1)^{L+1}$$

$$C = (-1)^{L+S},$$

where L and S are the orbital and intrinsic angular momenta of the $q\overline{q}$ pair, respectively. Certain J^{PC} cannot possibly be obtained by following the above relations, like $J^{PC} = 1^{-+}$, and these J^{PC} are a sure indicator that the meson state is non-$q\overline{q}$. Many hybrid

[14]Conservation of angular momentum requires that, in general, particles of different J^{PC} have different angular decay distributions (see chapter 9).

mesons ($q\overline{q}g$) are expected to have exotic J^{PC}. The $\pi_1(1600)$ with $J^{PC} = 1^{-+}$ is an example of a recently discovered exotic state [41].

Third, branching ratios to different final states reveal valuable information. For example, glueballs are expected to have a property called "color blindness," meaning a glueball will not prefer to decay into one allowed final state over another. If the branching ratios of a certain meson decay follow this property, the meson could be a glueball candidate. Branching ratios among radiative decays are also used extensively to interpret meson states.

Fourth, the production mechanism in which a meson state is produced contains information on the nature of the meson. Some production mechanisms are "gluon-rich" like J/ψ radiative decays, while others have little or no coupling to gluons, like $\gamma\gamma$ collisions. If a state is produced dominantly in a gluon-rich environment, and appears weakly or not at all in other environments, then such information adds to the likelihood that the meson state is a glueball.

Other interpretation schemes also exist, like the glueball filter of the WA102 collaboration at CERN based on the momentum transfer with which a meson state is produced [42]. In general, the interpretation of a given meson is based on some combination of all of the above methods and by trying to fit the meson state within a much larger picture. For this reason, the discovery of every individual state provides valuable impetus for the whole field of light meson spectroscopy, tightening the constraints on new interpretations of new mesons.

2.5 Producing Mesons

There are many types of experiments in which light mesons can be produced and studied. Each contributes in its own way to the larger project of light meson spectroscopy. This section describes a few of the methods through which mesons are produced, paying special attention to exclusive photoproduction and those production mechanisms that are most closely related to photoproduction.

2.5.1 Meson Beams

Experiments with a pion or kaon beam, usually with beam energies of around several GeV, have been the most common type of experiment to study the spectroscopy of light mesons. In this production mechanism, the beam particle glances off a nuclear target through the exchange of some particle and is excited to a resonance state X (figure 2.9). The nucleon of the target either recoils as it is or is itself excited into some baryon resonance state. With a π^- beam, for example, meson resonances are produced according to $\pi^- N \to XN$ or $\pi^- N \to XN^*$, where N is a nucleon (proton or neutron) and N^* denotes an excited nucleon (e.g., Δ^+).

Typically, traditional quark model resonances are produced with meson beams, but it should also be possible to produce hybrid mesons or even glueballs. The first strong evidence, in fact, for a hybrid meson with exotic quantum numbers has come from E852 at Brookhaven, an experiment which used an 18 GeV π^- beam incident on a proton target [41]. The J^{PC} that are accessible to the produced resonance depends on the type

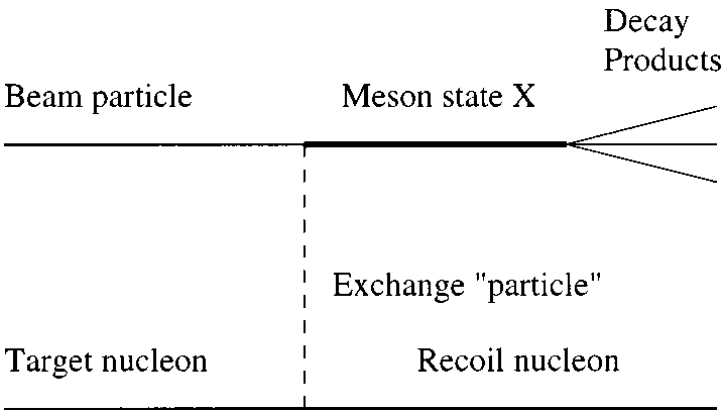

Figure 2.9: Illustration of the exclusive hadroproduction of a resonance (from [13]). In most cases, the beam particle is either a π^- or K^-.

of particle exchanged. The exchange particle can either be a traditional meson, like a 0^{-+} π meson or, more rarely, a 1^{--} ρ meson, or a more phenomenological "particle" like the Pomeron.

The resonance X is produced at small angles characterized by the momentum transfer: $t \equiv (P_{BEAM} - P_X)^2$, where P_{BEAM} and P_X are the four-momenta of the beam and produced resonance, respectively[15]. The momentum transfer distribution depends on the type of particle exchanged. With a pion as the exchange particle, for example, the distribution falls rather steeply with the momentum transfer, falling exponentially like e^{-bt}, where b is typically on the order of $5\,\mathrm{GeV}^{-2}\mathrm{c}^2$.

[15] As it is defined, the momentum transfer t is less than zero.

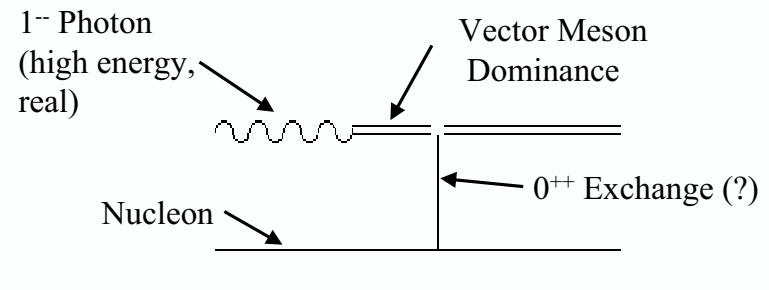

Figure 2.10: An illustration of exclusive photoproduction. When interacting strongly with the target nucleon, the beam photon can behave as if it were a vector meson.

2.5.2 Photoproduction

In photoproduction ($\gamma N \rightarrow XN$), a beam of high energy photons interacts with a nuclear target [43]. As in the production with meson beams, a beam particle glances off a nucleon of the nucleus at small angles by the exchange of an exchange particle and is excited into a resonance state (figure 2.10). In the case of photoproduction, however, we begin with a 1^{--} photon rather than a 0^{-+} pion or kaon, thus potentially providing access to a series of mesons with different J^{PC}. Furthermore, by the Vector Dominance Model (see section 3.1), a high energy photon can fluctuate into a virtual quark-antiquark pair, effectively becoming a 1^{--} vector meson, like a $\rho(770)$, $\omega(782)$, or $\phi(1020)$. In other words, the photon beam can act as if it were a beam of vector mesons.

If a Pomeron is exchanged between the nucleon and the beam photon, a process called diffraction, the virtual $\rho(770)$, $\omega(782)$, or $\phi(1020)$ of the beam can be knocked

on-shell, becoming a real $\rho(770)$, $\omega(782)$, or $\phi(1020)$. It is by this method that copious numbers of ground state vector mesons are photoproduced. The photoproduction of ground state vectors has been studied for many years and is well-understood. However, diffraction is also expected to result in excited state vectors, but this situation is far from clear, as will be discussed extensively in section 3.3.

Particles other than the Pomeron can also be exchanged, e.g., the π or ρ mesons, but these processes are supposed to become less significant with increasing beam energies. Another possibility is Primakoff production [44], where the beam photons interact with the photons of the nuclear Coulomb field, resulting in $\gamma\gamma$ collisions. Primakoff production has been studied at lower energies, but is generally assumed to be insignificant at higher energies. High energy photoproduction of meson resonances, with photon energies greater than around 30 GeV, is expected to be dominated by diffraction.

In addition to producing vectors and other conventional mesons, there have been predictions that photoproduction is an ideal way to produce hybrid mesons [33]. Unfortunately, experimental progress has lagged considerably far behind theory. The state of exclusive photoproduction will be discussed in more detail in chapter 3.

2.5.3 e^+e^- Annihilation

Perhaps the most efficient way of studying the vector meson spectrum is through e^+e^- annihilation ($e^+e^- \to \gamma^* \to V$). When an electron and positron annihilate, they produce a virtual photon with a mass equal to the center of mass energy of the e^+e^- system. The virtual photon, having $J^{PC} = 1^{--}$, is then free to materialize into hadrons

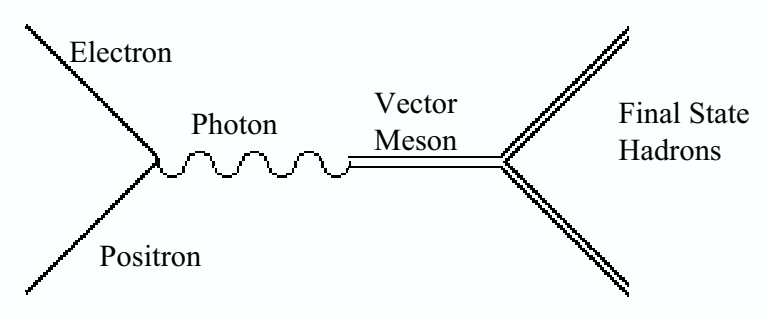

Figure 2.11: A diagram of e^+e^- annihilation. The incoming electron and positron annihilate into a virtual photon, which can then materialize into a vector meson.

(figure 2.11). If the center of mass energy is equal to the mass of a vector meson, the photon will often materialize into that vector meson, and a peak will be seen in the cross section. By scanning through center of mass energies, the entire vector meson spectrum can be mapped out. Since this method only produces 1^{--} states directly, there is no need for complicated angular analyses, and, except for interferences among the different 1^{--} mesons, the analyses are straightforward. For this reason, and because photoproduction is directly related to e^+e^- annihilation through the involvement of the photon, e^+e^- annihilation is often used as a standard to which photoproduction results can be compared. While the comparisons between photoproduction and e^+e^- annihilation have often proved useful, occasionally they have led to misguided interpretations of the photoproduction results, as will be seen in section 3.3.

2.5.4 $\gamma\gamma$ Collisions

Two photon collisions can be studied at e^+e^- accelerators. Rather than annihilating, an electron and positron can each emit a photon. The photons collide and result in a meson state ($\gamma\gamma \to X$). Combining two 1^{--} particles leads to another set of possible J^{PC} for the meson, in particular 0^{++} and 2^{++}. Two photon collisions can be used in conjunction with other production mechanisms to study the probability that a particular resonance should be interpreted as a glueball, since glueballs are not expected to couple to photons and thus should be absent from any two photon collision.

2.5.5 Radiative J/ψ Decays

Radiative J/ψ decays ($J/\psi \to X\gamma$) are another way to study 0^{++} and 2^{++} states, but unlike two-photon collisions, radiative J/ψ decays are likely to produce glueballs because of the large gluonic component of the decay. Before the c and $\overline{c}$ quarks of the J/ψ annihilate, a photon is radiated, leaving the $c\overline{c}$ system with the right quantum numbers to annihilate into two gluons. The two 1^{--} gluons combine (like the two photons of the $\gamma\gamma$ collisions) to form either a conventional $q\overline{q}$ state or a glueball. J/ψ decays can be studied at e^+e^- colliders that have their center of mass energies fixed at the J/ψ mass.

Chapter 3

The Background and History of Exclusive Photoproduction

In exclusive photoproduction[1], a photon interacts with a nucleon to produce a resonance X, $\gamma N \rightarrow XN$. A brief overview of this production mechanism has already been given in section 2.5.2. This chapter will provide more detail on the theory of photoproduction, and will present a short summary and history of the contributions of exclusive photoproduction to light meson spectroscopy. As we will see, while the exclusive photoproduction of the light quark ground state vectors, the $\rho(770)$, $\omega(782)$, and $\phi(1020)$ mesons, has been studied and understood rather successfully, the exclusive photoproduction of nearly everything else remains fraught with difficulties.

[1] A popular introduction to photoproduction can be found in [45]. More detailed information is in [43].

3.1 Theoretical Overview

When a photon passes near matter, such as the nucleus of an atom, it can occasionally materialize into an e^+e^- pair through the electromagnetic coupling between photons and the electric charge of electrons and positrons. This is the well-known phenomenon of pair creation in QED. At higher energies, in exactly the same manner as the coupling to e^+e^-, the photon can fluctuate into quarks and antiquarks through their electric charge. When the $q\overline{q}$ pair has the right mass, e.g., the mass of the ρ or ω or ϕ meson, this fluctuation allows the photon to behave as if it were a $q\overline{q}$ vector meson. The fluctuations of the photon into vector mesons is generally described by the Vector Dominance Model (VDM) [46, 47]. Several features of VDM will be important for what follows.

First, VDM predicts the ratios of the hadronic components of the photon. Using the fact that the cross section for a photon coupling to a $q\overline{q}$ pair is proportional to the square of the charge of the quark, and assuming the masses of the light quarks to be equal, which becomes a better approximation as the energy of the photon increases, the ratio of the couplings of the different vector mesons to the photon can be obtained simply by counting charges. According to the quark model, the quark compositions of the ground state vectors ρ, ω, and ϕ are:

$$\rho = \frac{1}{\sqrt{2}}[u\overline{u} - d\overline{d}]$$

$$\omega = \frac{1}{\sqrt{2}}[u\overline{u} + d\overline{d}]$$

$$\phi = s\overline{s}.$$

The square of the quark charges follows immediately:

$$(e_\rho)^2 = [\frac{1}{\sqrt{2}}(\frac{2}{3} - (-\frac{1}{3}))]^2 = \frac{1}{2}$$

$$(e_\omega)^2 = [\frac{1}{\sqrt{2}}(\frac{2}{3} + (-\frac{1}{3}))]^2 = \frac{1}{18}$$

$$(e_\phi)^2 = (-\frac{1}{3})^2 = \frac{1}{9}.$$

The ratio of the ρ to ω to ϕ components of the photon is then:

$$\rho : \omega : \phi = 9 : 1 : 2. \tag{3.1}$$

Among other methods, this ratio can be tested in the exclusive photoproduction of the ground state vectors, as will be discussed in section 3.2.

Second, VDM, again combined with assumptions from the quark model, relates the cross section for photoproducing a vector, $\sigma(\gamma p \to Vp)$, with the cross section for producing the same vector in e^+e^- annihilation, $\sigma(e^+e^- \to V)$:

$$\sigma_{peak}(e^+e^- \to V) = \frac{64\pi^2\alpha b}{m_V\Gamma_V}\frac{\sigma(\gamma p \to Vp)}{\sigma^2_{tot}(Vp)}. \tag{3.2}$$

Here, m_V and Γ_V are the mass and width of the vector, respectively; α is the fine struc-

ture constant of QED; b is the slope of the t' distribution[2]; and $\sigma_{tot}(Vp)$ is the total vector-proton cross section, which can be measured independently. Since vector meson production in e^+e^- annihilation is generally cleaner than in photoproduction, equation 3.2 is often combined with results from e^+e^- annihilation experiments in attempts to interpret photoproduction results.

Both of these two features of VDM, the ratios of vector mesons constituting the photon and the relationship between photoproduction and e^+e^- annihilation, have commonly been assumed to carry over in a straightforward way from the case of the ground state vectors (ρ, ω, and ϕ) to the case of the excited state vectors (ρ', ω', and ϕ'). For example, the ratios with which the excited state vectors are found within the photon is supposed to follow $\rho' : \omega' : \phi' = 9 : 1 : 2$, as in the case of the ground state vectors. Similarly, equation 3.2 has been assumed to hold equally well for excited state vectors as for ground state vectors simply by replacing V with V'. These assumptions are an extension of VDM, sometimes called the Generalized Vector Dominance Model, or GVDM [48]. As we will see later in section 3.3, the assumptions of GVDM have generally proved unsuccessful in disentangling the results of the photoproduction of higher mass mesons.

Another important feature of the exclusive photoproduction of mesons is s-Channel Helicity Conservation (SCHC) [49], which describes the spin polarization of the produced meson. According to SCHC, a photoproduced meson will retain the helicity of the beam

[2]The t' distributions of photoproduction generally fall like $ae^{-bt'}$ (see appendix B).

photon, i.e., it will be polarized along the beam direction. To accommodate this, the Gottfried-Jackson coordinate system is often used to analyze decaying resonances, where the z-axis of the particle decay is taken to be the beam direction (see appendix B). The SCHC assumption has been found to work well in the exclusive photoproduction of vector mesons, but is often violated in the case that $J^{PC} \neq 1^{--}$.

In fact, as will be discussed extensively in section 3.3, while there is strong evidence for the photoproduction of non-vector states, very little about the photoproduction of these states is understood. In addition, many theoretical models predict that photoproduction is the ideal way to study the hybrid meson spectrum (e.g., [33]), but no work is yet to be done experimentally.

3.2 Photoproducing Ground State Vectors

The photoproduction of the $\rho(770)$, $\omega(782)$, and $\phi(1020)$ vector mesons was first studied more than thirty years ago [48]. The mechanism behind their production can easily be understood through VDM, where the photon fluctuates into a $q\overline{q}$ pair and glances off a nucleon through the exchange of a Pomeron. This peripheral interaction provides the necessary energy to materialize the $q\overline{q}$ pair, which is then the physical $\rho(770)$, $\omega(782)$, or $\phi(1020)$ vector meson.

Studying the ratios of the photoproduction of the ground state vectors, some deviation from the basic ratio predicted by VDM, $\rho{:}\omega{:}\phi = 9{:}1{:}2$, has been found [50, 51]. The cross section for $\phi(1020)$ production ($\gamma p \to \phi p$) appears to be a factor of four too

low. However, recent work has shown the VDM ratio is valid when the photon becomes virtual, i.e., when the photon has a mass approaching the masses of the vector mesons.

Figure 3.1 shows a compilation of experimental results on the photoproduction of all the ground state vector mesons as a function of center of mass energy[3] [50]. In addition to showing the ratios of the productions of the vector mesons, this figure also shows that the energy dependences of the production of each light vector meson has the same general shape. This will be important for what follows later in chapter 8.

3.3 Photoproducing Higher Mass Mesons

Besides the $\rho(770)$, $\omega(782)$, and $\phi(1020)$ ground state vectors, four additional light quark meson states have been produced and studied in exclusive photoproduction. Unlike the ground state vectors, however, the interpretations of these higher mass states still present many difficulties. In the following, we refer to the four states as the "$\rho'(1600)$," the "$\omega\pi^0(1250)$," the "$\omega(1650)$," and the "$K^+K^-(1750)$." After describing the state of the field of exclusive photoproduction in 1978, and introducing the photoproduction experiments that have been performed since, these four states will be presented as four different case studies.

[3]Recall that the center of mass energy is related to the photon beam energy through equation B.1. In figure 3.1, the center of mass energy, $\sqrt{s}$, is referred to as W.

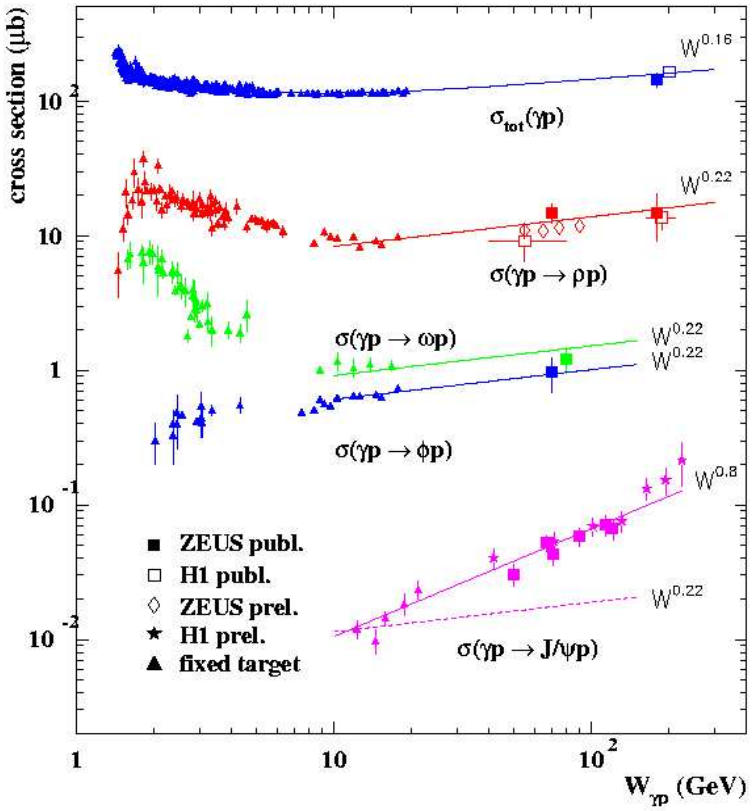

Figure 3.1: A compilation of experimental results on the exclusive photoproduction of ground state vectors (from [50]). W is the center of mass energy, referred to elsewhere as $\sqrt{s}$. The E831/FOCUS results, to be presented later, fall in the range from $W \approx 8\,\mathrm{GeV}$ to $W \approx 16\,\mathrm{GeV}$.

3.3.1 The State of the Field in 1978

A comprehensive review article of photoproduction was written by Bauer, Spital, and Yennie in 1978 [48]. Because of the large uncertainty that was still present in the higher mass states, the majority of the article was spent describing the photoproduction of the ground state vectors. The higher mass states were described as "undoubtedly important," but "still only imperfectly understood."

The 1978 article presented evidence for the two very broad high mass states that had been reported by photoproduction experiments up to that time. These states were first referred to as the $\rho'(1250)$ [52] and the $\rho''(1600)$ [53, 54] (see figures 3.2, 3.3, and 3.4). Without any angular analyses, both were assumed to be vectors, radial excitations of the $\rho(770)$. The lower mass state, the $\rho'(1250)$, was reported to have a mass near $1200\,\mathrm{MeV/c^2}$ and a width somewhere between 150 and $310\,\mathrm{MeV/c^2}$. It was seen in the $\pi^+\pi^-\pi^0\pi^0$ final state by several experiments, and remained predominantly present after an ω cut, signifying its major decay mode was $\omega\pi^0$. In the following, this state will be referred to as the "$\omega\pi^0(1250)$" (see section 3.3.4). The higher mass state, the $\rho''(1600)$, was seen by several experiments in the $\pi^+\pi^-$ and $\pi^+\pi^-\pi^+\pi^-$ final states. Experiments reported its mass to be $1600\,\mathrm{MeV/c^2}$ with an uncertainty of around $20\,\mathrm{MeV/c^2}$ and a very large width of around $300\,\mathrm{MeV/c^2}$. The $\rho''(1600)$, later referred to as the "$\rho'(1600)$," will be discussed in section 3.3.3. Besides brief descriptions of these results, the 1978 article reported nothing else concerning the higher mass states.

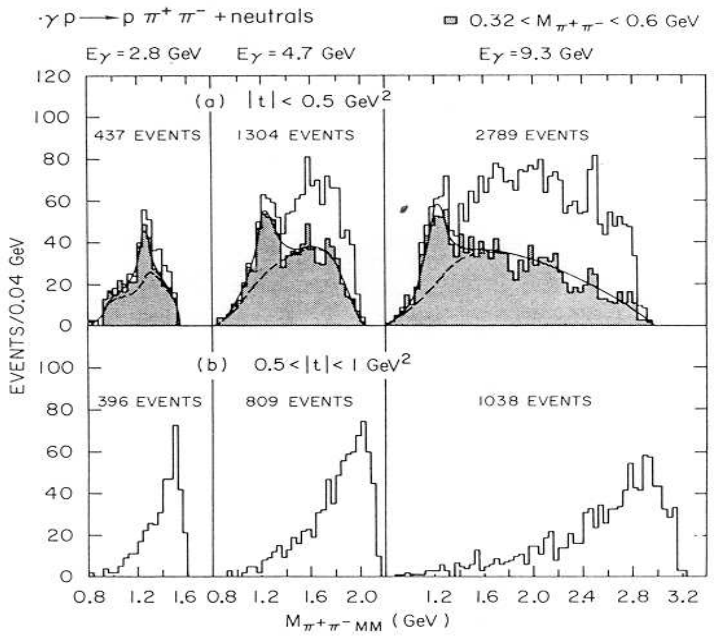

Figure 3.2: First observation of the $\rho'(1250)$ in 1974; from a collaboration between the Lawrence Berkeley Laboratory (LBL) and SLAC [52]. The $\rho'(1250)$ was later found to decay only to $\omega\pi^0$, and even later it was found to be non-1^{--} and has been equated with the $b_1(1235)$ (see section 3.3.4).

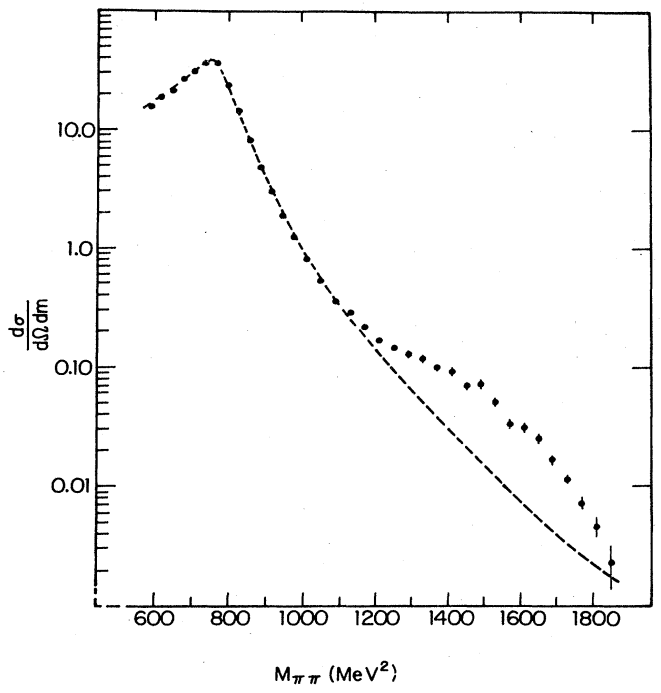

Figure 3.3: The $\rho''(1600)$ in $\pi^+\pi^-$ as seen in 1971; from a collaboration between MIT and DESY [53]. The $\rho''(1600)$ was later renamed the $\rho'(1600)$ and is now thought to be a combination of two resonances, the $\rho(1450)$ and the $\rho(1700)$.

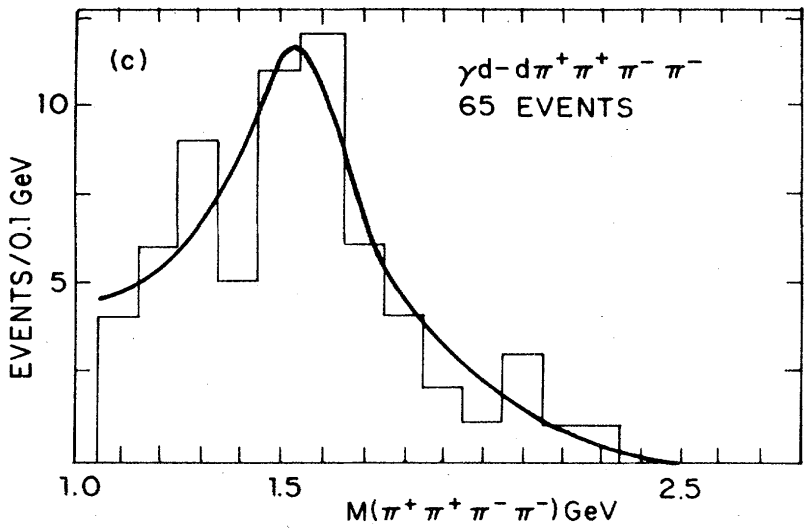

Figure 3.4: The $\rho''(1600)$ in $\pi^+\pi^-\pi^+\pi^-$ as seen in 1975. This is from an early photoproduction experiment at SLAC [54].

3.3.2 Photoproduction Experiments Between 1978 and 1990

Since 1978, there have been several photoproduction experiments that have contributed to the study of light meson spectroscopy. In addition to the resonances included in the 1978 review article, then called the $\rho'(1250)$ and $\rho''(1600)$, enhancements have been reported in the $\pi^+\pi^-\pi^0$ and K^+K^- final states. Four photoproduction experiments during the 1980's are noteworthy for their contributions. Since around 1990, however, very little progress has been made in the exclusive photoproduction of meson states.

The most noteworthy of the photoproduction experiments of the 1980's is the Omega Spectrometer Collaboration at CERN [55]. This experiment used bremsstrahlung photons of energies between 20 and 70 GeV, which derived from an 80 GeV electron beam originating from the CERN Super Proton Synchrotron (SPS). The photons were incident on a 60 cm liquid hydrogen target. The Omega Spectrometer Collaboration published results on all four of the higher mass exclusively photoproduced states to be discussed later and led the way for the other photoproduction experiments.

The LAMP2 (Large Aperture Magnet Spectrometer) experiment at the 5 GeV electron synchrotron at Daresbury Laboratory also used bremsstrahlung photons derived from an electron beam [56]. The photon energy range was between 1 and 5 GeV. The target was liquid hydrogen. With such small energies for the photon beam, however, the experiment was susceptible to backgrounds stemming from nucleon excitations, for example backgrounds from Δ states, backgrounds that are not present with higher beam energies.

The third photoproduction experiment to make contributions to light meson spectroscopy during the 1980's is the SLAC Hybrid Facility (SHF) at the Stanford Linear Accelerator (SLAC) [57]. The SLAC Hybrid experiment used 20 GeV photons obtained by Compton back-scattering 4.7 eV laser photons from the 30 GeV electron beam at SLAC. A one meter long hydrogen bubble chamber was used as a target.

Finally, Fermilab began contributing to photoproduction physics with E401 [58]. Photon energies ranged all the way from 35 to 225 GeV depending on the acceptances of the final state being studied and were incident on either a deuterium or hydrogen target. The photon beam was generated mostly from high energy π^0 decays, which were created after 350 GeV protons from the Fermilab proton accelerator collided with a beryllium target. In addition to the creation of π^0, however, some K_L contamination resulted from this method.

3.3.3 The Story of the "$\rho'(1600)$"

The $\rho'(1600)$ (originally referred to as the $\rho''(1600)$ in the 1978 photoproduction review article [48]) is the oldest of the higher mass "resonances" to be photoproduced (see figures 3.3 and 3.4). The current interpretation of the older photoproduction experiments is that the signal once known as the $\rho'(1600)$ is actually composed of two ρ states, the $\rho(1450)$ and the $\rho(1700)$. The photoproduced $\rho'(1600)$ has been observed decaying to three final states: $\pi^+\pi^-$, $\pi^+\pi^-\pi^+\pi^-$, and $\pi^+\pi^-\pi^0\pi^0$.

Shortly after its first observations, the photoproduced $\rho'(1600)$ was found to be in excellent agreement with the results of e^+e^- annihilation experiments. This agreement

was supported by the relationship between the cross sections of the processes $e^+e^- \rightarrow V$ and $\gamma p \rightarrow Vp$ (equation 3.2) [59]. Because this agreement was established early in the history of photoproducing higher-mass mesons (1981), the $\rho'(1600)$ was often considered to be the best-established of all the higher-mass photoproduced resonances. The statement from the introduction of an Omega Spectrometer paper is typical: "The search for radial recurrences of the ρ, ω, and ϕ vector mesons has so far produced only one well-established resonance, the $\rho'(1600)$" [60].

In 1980, LAMP2 performed a fit on their $\pi^+\pi^-\pi^+\pi^-$ mass spectrum using two interfering Breit-Wigners (figure 3.5) [61]. They found they could reproduce the mass spectrum well if the masses and widths of the Breit-Wigners corresponded to the masses and widths of the $\omega\pi^0(1250)$ and the $\rho'(1600)$ (then known as the $\rho'(1250)$ and $\rho''(1600)$, respectively), and if the interference were completely destructive. However, the statistics were very poor, and apart from this early attempt to incorporate two resonances into a fit of the $\rho'(1600)$ mass spectrum, all subsequent photoproduction experiments have reported only one very broad resonance.

The further progression of our understanding of the $\rho'(1600)$ can be traced through a series of Omega Spectrometer analyses. In 1980, the Omega Spectrometer published results in $\pi^+\pi^-$ [62]; in 1981, the $\pi^+\pi^-\pi^+\pi^-$ spectrum was studied [59]; and in 1985, the $\pi^+\pi^-\pi^0\pi^0$ spectrum [63]. The corresponding mass spectra can be seen in figures 3.6, 3.7, and 3.8. The mass and width of the $\rho'(1600)$ varies substantially from final state to final state. The mass goes from $1.59\pm0.02\,\mathrm{GeV/c^2}$ to $1.52\pm0.03\,\mathrm{GeV/c^2}$ to $1.66\pm0.03\,\mathrm{GeV/c^2}$

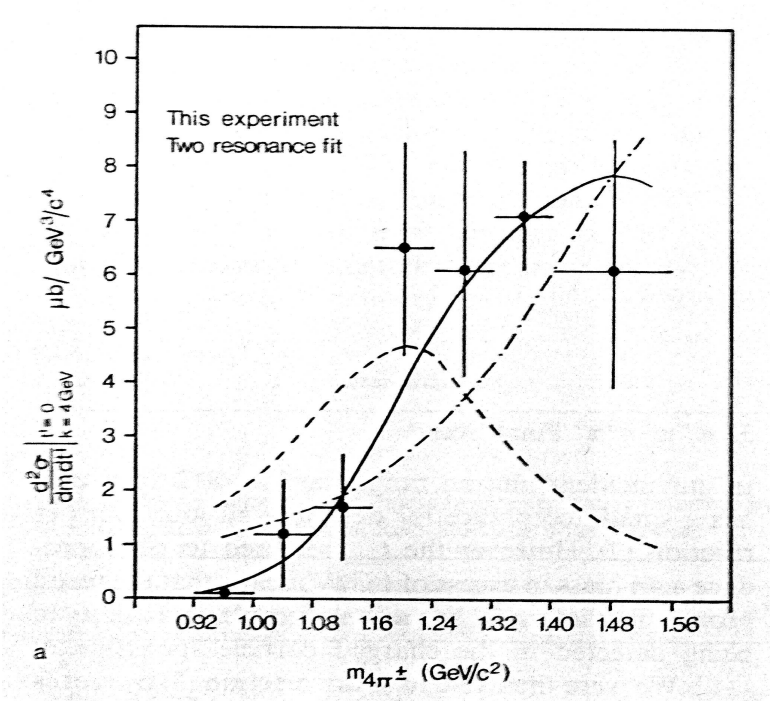

Figure 3.5: The photoproduced $\pi^+\pi^-\pi^+\pi^-$ mass spectrum from LAMP2 in 1980 (from [61]). This is an early attempt to fit the $\pi^+\pi^-\pi^+\pi^-$ mass spectrum with two resonances. The fit shown represents destructive interference between a resonance at 1200 MeV/c^2 and the $\rho'(1600)$. Subsequent fits use only the $\rho'(1600)$.

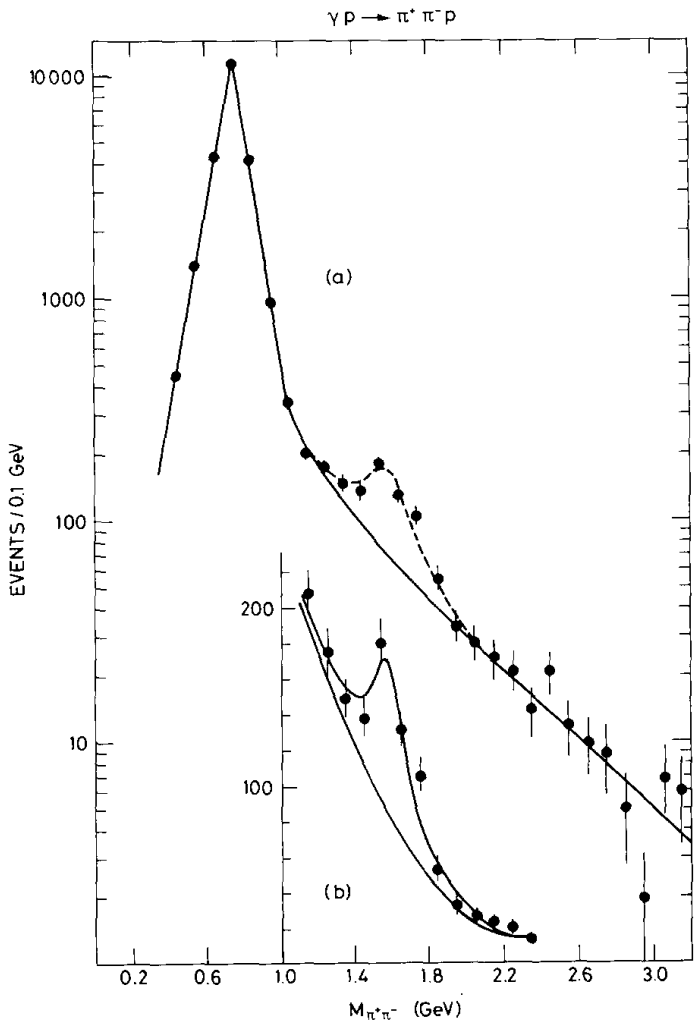

Figure 3.6: The photoproduced $\rho'(1600)$ decaying to $\pi^+\pi^-$ as seen by the Omega Spectrometer in 1980 (from [62]). The mass and width were measured to be $1590 \pm 20\,\mathrm{MeV/c^2}$ and $230 \pm 80\,\mathrm{MeV/c^2}$, respectively.

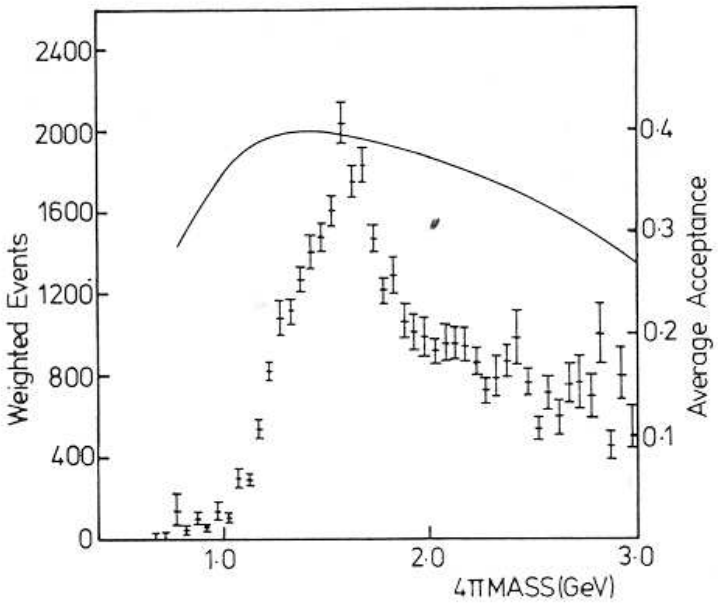

Figure 3.7: The photoproduced $\rho'(1600)$ decaying to $\pi^+\pi^-\pi^+\pi^-$ as seen by the Omega Spectrometer in 1981 (from [59]). The mass and width were measured to be $1520 \pm 30\,\mathrm{MeV/c^2}$ and $400 \pm 50\,\mathrm{MeV/c^2}$, respectively.

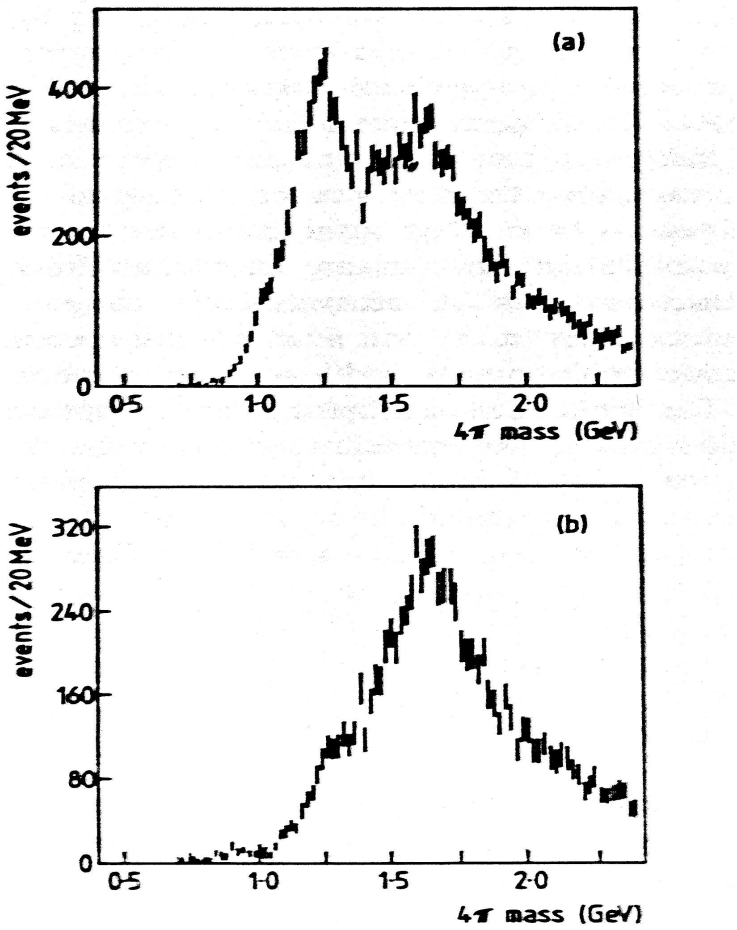

Figure 3.8: The photoproduced $\rho'(1600)$ decaying to $\pi^+\pi^-\pi^0\pi^0$ as seen by the Omega Spectrometer in 1985 (from [63]). (a) The total $\pi^+\pi^-\pi^0\pi^0$ mass spectrum. (b) The $\pi^+\pi^-\pi^0\pi^0$ mass spectrum after excluding the $\omega(782) \to \pi^+\pi^-\pi^0$ decay. After excluding the $\omega(782)$, the spectrum is dominated by the $\rho'(1600)$. The mass and width were measured to be $1660 \pm 30\,\mathrm{MeV/c^2}$ and $300 \pm 50\,\mathrm{MeV/c^2}$, respectively.

in $\pi^+\pi^-$, $\pi^+\pi^-\pi^+\pi^-$, and $\pi^+\pi^-\pi^0\pi^0$, respectively. Similarly, the width varies from $0.23\pm0.08\,\mathrm{GeV/c^2}$ to $0.40\pm0.05\,\mathrm{GeV/c^2}$ to $0.30\pm0.05\,\mathrm{GeV/c^2}$. Among other difficulties, the inconsistencies among the masses and widths of the final states were taken to be indicative of some sort of interference phenomenon. Either the $\rho'(1600)$ was interfering with the background or a second interfering resonance was present, but no compelling scenarios could be found.

In 1987, a paper was published by Donnachie and Mirzaie [64] arguing that the $\rho'(1600)$ is actually composed of two interfering ρ resonances. They performed a simultaneous fit to all $\pi^+\pi^-$ and $\pi^+\pi^-\pi^+\pi^-$ data from photoproduction and e^+e^- annihilation based on the relationship between cross sections discussed above (equation 3.2). In order for the fit to be satisfactory, they found that contributions to the photoproduction data coming from states other than 1^- were essential. After working through several difficulties, the fit showed excellent agreement with the data when two resonances were used. The lighter of the two ρ resonances had a mass of $1.465\pm0.025\,\mathrm{GeV/c^2}$ and width of 0.235 ± 0.025 GeV/c^2. The heavier resonance had a mass of 1.700 ± 0.025 GeV/c^2 and width of 0.220 ± 0.025 GeV/c^2. These two resonances soon became known as the $\rho(1450)$ and $\rho(1700)$.

Later in 1987, Donnachie and Clegg fit the $\eta\rho$ mass spectrum from photoproduction and e^+e^- annihilation simultaneously and found that interference between the $\rho(1450)$ and $\rho(1700)$ was necessary in order to explain the appearance of an enhancement at $1600\,\mathrm{MeV/c^2}$ in the e^+e^- data and the absence of any enhancement in the photopro-

duction data [65]. The photoproduction data, however, was very weak, the $\eta\rho$ mass plot having bins of 200 MeV/c^2. Donnachie and Clegg later extended the scope of their simultaneous e^+e^- and photoproduction fits in 1988 [66], 1990 [67], and again in 1994 [68]. Each extension provided additional support for the existence of two separate resonances constituting the $\rho'(1600)$ signal.

Further solidifying the two resonance interpretation, DM2 in 1988 fit the $e^+e^- \to \eta\pi^+\pi^-$ mass spectrum with two resonances and found excellent agreement with the original mass and width parameters of Donnachie and Mirzaie [69]. More recent evidence for the separate existences of the $\rho(1450)$ and $\rho(1700)$ has come from the Crystal Barrel experiment using proton-antiproton annihilation at rest [70]. A Dalitz analysis was performed on the $\pi^-\pi^0\pi^0$ channel and the $\rho(1450)$ and $\rho(1700)$ could be easily isolated.

The modern interpretation is now very stable. The $\rho(1450)$ is the first radial excitation of the ground state $\rho(770)$; and the $\rho(1700)$ is the $^3D_1$ orbital excitation of the $\rho(770)$. The masses and widths agree well with the quark model predictions of Godfrey and Isgur [14].

While the current understanding is satisfactory, the last photoproduction results were published in 1985, at a time when the $\rho(1450)$ and $\rho(1700)$ were still considered a single $\rho'(1600)$. In fact, this leaves photoproduction in an awkward situation: the "best-established" of the photoproduced higher mass resonances is now no longer a resonance at all. Clearly, the region ought to be revisited with our present understanding and with an increase in statistics.

3.3.4 The Story of the "$\omega\pi^0(1250)$"

The second of the higher mass mesons to be discussed, referred to here as the "$\omega\pi^0(1250)$," also appeared in the comprehensive 1978 review article by Bauer, Spital, and Yennie. There it was assumed to be the $\rho'(1250)$, a $J^{PC} = 1^{--}$ recurrence of the $\rho(770)$. In 1978, the most accurate measurements of its mass could only state that it was around 1.2 GeV/c^2; and its width was even less well measured, somewhere between 150 and 310MeV/c^2 (figure 3.2). Since 1978, four photoproduction analyses have been published on this resonance. The contemporary understanding of the photoproduced $\omega\pi^0(1250)$ is that it is not a vector meson at all, but that it is almost certainly the $J^{PC} = 1^{+-}$ $b_1(1235)$.

In 1980, the LAMP2 experiment published an analysis of the $\omega\pi^0$ final state along with their analysis of the $\rho'(1600)$ [61]. They performed an angular analysis by considering the hypotheses that the $\omega\pi^0(1250)$ was either a $J^P = 1^+$ or a $J^P = 1^-$ state, and assumed that either of these states would be polarized along the direction of the photon beam according to s-Channel Helicity Conservation (SCHC). They found that the SCHC-conserving 1^- contribution dominated their $\omega\pi^0$ spectrum and concluded that the $\omega\pi^0(1250)$ must be a recurrence of the $\rho(770)$ and not the $b_1(1235)$ (then called the $B(1250)$). The measured mass and width were 1.29±0.04GeV/c^2 and 0.32±0.10GeV/c^2, respectively.

However, because of the low energy of their photon beam, the experiment had a large background from events where the proton was excited into a Δ^+. In particular,

they suffered from the background $\gamma p \to \omega\Delta^+$, where the Δ^+ then decays to $\pi^0 p$, thus mimicking the $\omega\pi^0$ final state. In addition, the analysis had less than 200 events in the signal region and had very non-uniform detector acceptances.

Later in 1980, the Omega Spectrometer Collaboration performed an analysis similar to the LAMP2 analysis, but without the problems associated with the Δ^+ and with a more uniform detector acceptance [71]. A lack of statistics was still a problem, however, with less than 100 events in the signal (figure 3.9). Again SCHC was assumed and again only the 1^+ and 1^- hypotheses were considered. They found that the $\omega\pi^0(1250)$ decays isotropically in both sets of decay angles – the angles associated with $\omega\pi^0(1250) \to \omega\pi^0$ and those associated with $\omega \to \pi^+\pi^-\pi^0$. This was inconsistent with both the 1^+ and 1^- hypotheses, and they concluded that the $\omega\pi^0(1250)$ must be a mixture of both possibilities, in fact mostly 1^- over 1^+ in the ratio of about 2:1. Combining this angular analysis with their large width measurement of ≈ 300 MeV/c^2, which is substantially larger than the $b_1(1235)$ width of ≈ 150 MeV/c^2, they agreed with LAMP2 in concluding that the $\omega\pi^0(1250)$ is not the $b_1(1235)$.

In 1984, however, the Omega Spectrometer Collaboration revisited the question of the 1^+ or 1^- nature of the $\omega\pi^0(1250)$, this time reversing their conclusion [72]. With more than five times the statistics of their previous analysis (figure 3.10), they were not forced to impose the assumption of SCHC. Instead they performed an angular analysis with 25 different moments[4], some of which obeyed SCHC and some which did not. They

[4]For a discussion of moments and their importance for angular analyses, see section 9.4.

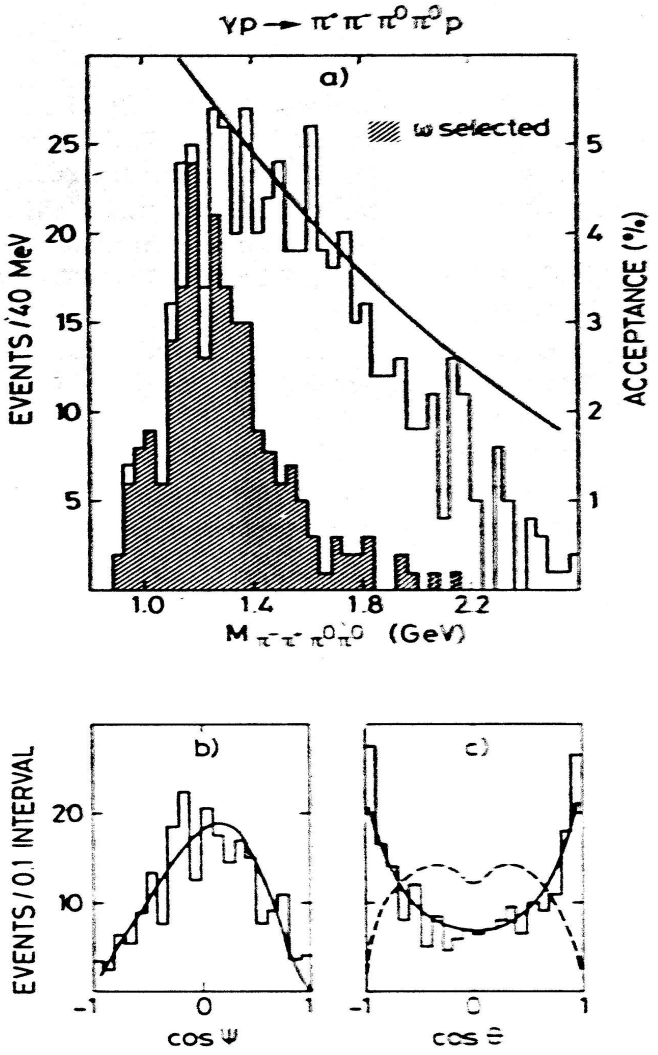

Figure 3.9: The $\omega\pi^0(1250)$ as seen by the Omega Spectrometer in 1980 (from [71]). (a) The clear portion of the histogram is the total $\pi^+\pi^-\pi^0\pi^0$ mass spectrum. The darkened portion results when an $\omega(782) \to \pi^+\pi^-\pi^0$ decay is required. (b) The decay angle for the $\omega\pi^0(1250) \to \omega\pi^0$ decay. The solid line is the expectation for an isotropic decay after the acceptance of the detector has been simulated. (c) The decay angle for the $\omega(782) \to \pi^+\pi^-\pi^0$ decay. Again, the solid line is the isotropic decay expectation. While the isotropic decays are inconsistent with both the 1^{--} and 1^{+-} interpretations, it was concluded that the $\omega\pi^0(1250)$ is primarily 1^{--}, in the ratio 2 : 1.

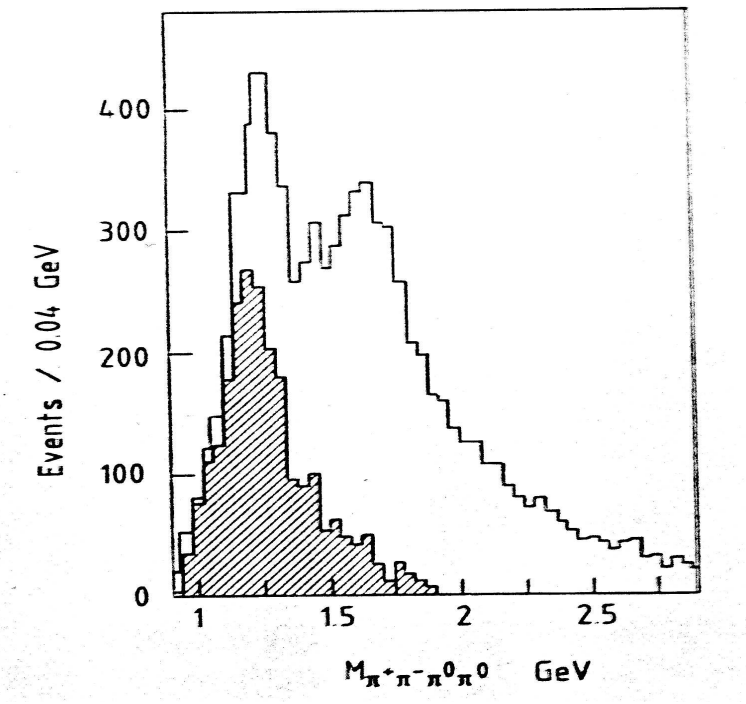

Figure 3.10: The $\omega\pi^0(1250)$ as seen by the Omega Spectrometer in 1984 (from [72]). The clear portion of the histogram is the total $\pi^+\pi^-\pi^0\pi^0$ mass spectrum. The darkened portion results when an $\omega(782) \to \pi^+\pi^-\pi^0$ decay is required. A full angular analysis of this spectrum showed the $\omega\pi^0(1250)$ to be consistent with the 1^{+-} $b_1(1235)$.

found that the non-SCHC contributions of the 1^+ decay could reproduce the angular spectrum better than the SCHC 1^- contributions. They concluded that their data was consistent with the non-SCHC photoproduction of the $J^P = 1^+$ $b_1(1235)$ with a small SCHC-conserving 1^- background, which they argued originated from the high mass tail of the $\rho(770)$. Furthermore, their width measurement shrunk from the $\approx 300\,\mathrm{MeV/c^2}$ measurement of the 1980 analysis to $\approx 200\,\mathrm{MeV/c^2}$, which was also more consistent with the $b_1(1235)$ parameters.

The SLAC Hybrid photoproduction experiment confirmed the Omega Spectrometer results in 1988 [73]. They used the same angular formalism with the same 25 moments as the 1984 Omega analysis. With a more uniform detector acceptance, they also concluded that the $\omega\pi^0(1250)$ has $J^P = 1^+$ and is thus consistent with the non-SCHC photoproduction of the $b_1(1235)$.

As we now understand the photoproduced $\omega\pi^0(1250)$, it appears to be completely consistent with the $b_1(1235)$. First, the mass and width of the $\omega\pi^0(1250)$ agree with those of the $b_1(1235)$ as it is produced in other production mechanisms. Second, as we have seen, the most recent angular analyses favor 1^+. And finally, no corresponding $\omega\pi^0(1250)$ resonance has ever been reported in e^+e^- annihilation, where all vector mesons ought to be produced. While the interpretation has stabilized, there is still uncertainty with regards to its production. How is such a non-1^{--} state diffractively photoproduced?

3.3.5 The Story of the "$\omega(1650)$"

A third higher mass meson reported in photoproduction appears in the $\pi^+\pi^-\pi^0$ final state at a mass near $1670\,\mathrm{MeV/c^2}$. Apart from a very low statistics study at Rutherford Laboratory in 1980 [74], the only published observation of the photoproduced enhancement comes from the Omega Spectrometer Collaboration in 1983 [60]. The standard interpretation is that it is an orbital excitation of the $\omega(782)$, the $\omega(1650)$ [75], but this interpretation has several difficulties stemming from inconsistencies with both VDM and e^+e^- annihilation.

The 1983 Omega Spectrometer observation of the enhancement in $\pi^+\pi^-\pi^0$ is shown in figure 3.11. Using a Breit-Wigner over a non-interfering third degree polynomial, the mass and width were measured to be $1670\pm20\mathrm{MeV/c^2}$ and $160\pm20\mathrm{MeV/c^2}$, respectively. In addition, the enhancement was found to come mostly through $\rho\pi$. While the natural interpretation of the enhancement appeared to be that it is a recurrence of either the $\omega(782)$ or $\phi(1020)$, making it an SU(3) partner of the $\rho'(1600)$, the cross section for the photoproduction of the $\pi^+\pi^-\pi^0$ enhancement was found to be comparable to the cross section of the photoproduction of the $\rho'(1600)$. This is drastically inconsistent with the ratios of cross sections predicted by GVDM of 9:1:2 for ρ', ω', and ϕ' production. Trying various interference scenarios between the enhancement and the background, the Omega group could pull the cross section down some, but it was still too large.

Further difficulties came in 1984, when the Omega Spectrometer Collaboration published a re-analysis of the $\pi^+\pi^-\pi^0$ data [76]. Rather than comparing to the $\rho'(1600)$,

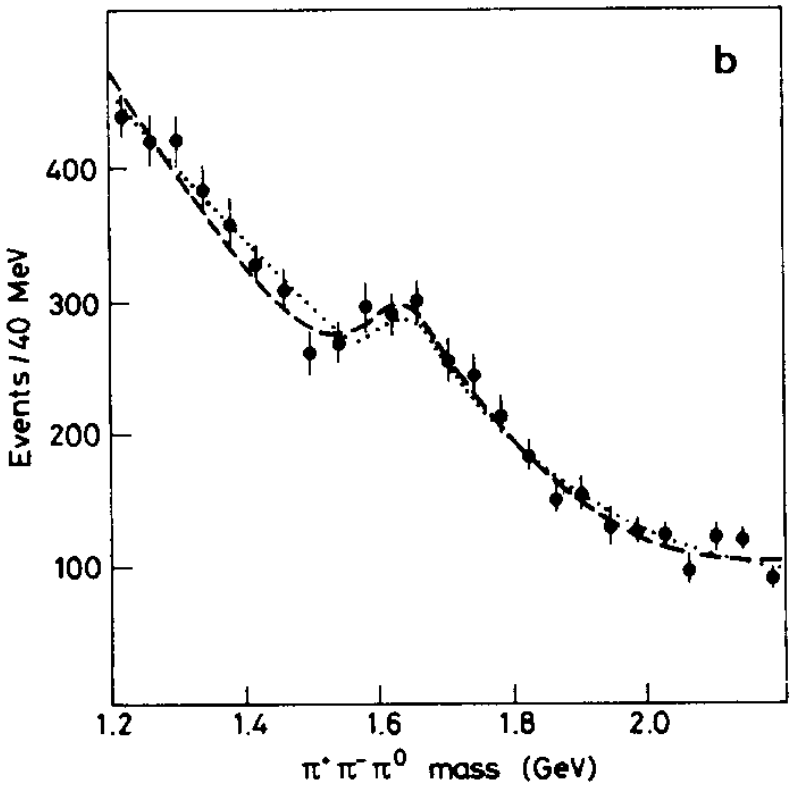

Figure 3.11: Evidence for a photoproduced $\omega(1650)$ decaying to $\pi^+\pi^-\pi^0$ by the Omega Spectrometer in 1983 (from [60, 76]). This is the only published evidence for a photoproduced enhancement in $\pi^+\pi^-\pi^0$. The mass is 1670 ± 20 MeV/c^2. The dashed and dotted lines are two different interference scenarios between the Breit-Wigner signal and the polynomial background. The interferences were introduced to provide consistency, unsuccessfully, with the e^+e^- cross section.

this time the photoproduction of the "$\omega(1650)$" was compared to the $e^+e^- \to \pi^+\pi^-\pi^0$ results. Using the relationship between photoproduction and e^+e^- annihilation cross sections (equation 3.2), the photoproduction cross section was again found to be too large.

In fact, it is difficult to reconcile the photoproduced $\pi^+\pi^-\pi^0$ enhancement with any aspect of the e^+e^- results. The $\omega(1650)$ of e^+e^- annihilation is seen primarily in the $\omega\pi\pi$ final state [75], but a search in the photoproduced $\omega\pi\pi$ spectrum by the Omega Spectrometer Collaboration in 1983 [77] came up empty. Figure 3.12 shows the results of the search. The dotted line is calculated from equation 3.2 and is the expected yield if the $e^+e^- \to \omega\pi\pi$ resonance were a $\phi(1020)$ recurrence. The dashed line is the $\omega(782)$ recurrence expectation. Clearly, the photoproduced $\omega\pi\pi$ spectrum is inconsistent with the expectations from e^+e^- annihilation.

For comparison, figures 3.13 and 3.14 show the results of a 1992 DM2 analysis of the $\omega(1650)$ in e^+e^- annihilation [78]. The $\omega(1650)$ is seen clearly in $\omega\pi\pi$, but the $\pi^+\pi^-\pi^0$ spectrum is questionable. Assuming there is an $\omega(1650)$ signal in $\pi^+\pi^-\pi^0$, a simultaneous fit between the two final states gives a mass and width of $1662 \pm 13\,\mathrm{MeV/c^2}$ and $280 \pm 24\,\mathrm{MeV/c^2}$, respectively, in reasonable agreement with the photoproduction measurement. However, the branching fractions of the $\omega(1650)$ to the $\omega\pi\pi$ and $\pi^+\pi^-\pi^0$ final states is completely reversed between photoproduction and e^+e^- annihilation.

To sum up, while the standard interpretation of the photoproduced $\pi^+\pi^-\pi^0$ enhancement is that it is the $\omega(1650)$, several outstanding difficulties with this inter-

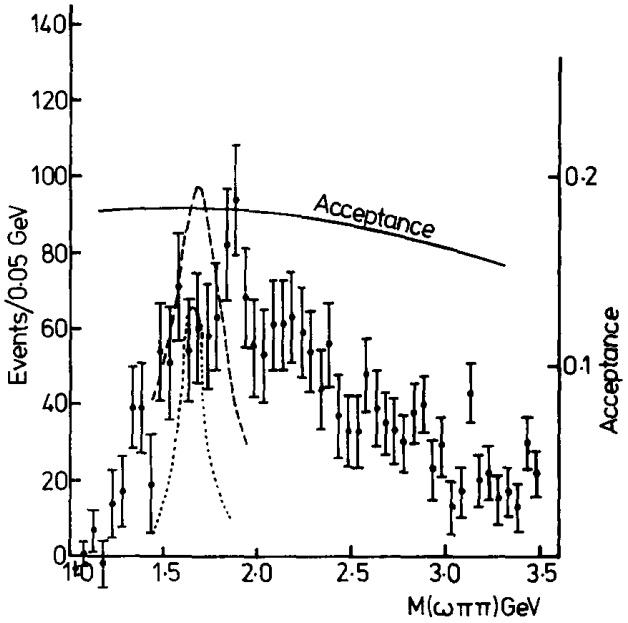

Figure 3.12: A search for the $\omega(1650) \to \omega\pi\pi$ decay by the Omega Spectrometer in 1983 (from [77]). Nothing is seen. The dashed line is the prediction from e^+e^- assuming that the e^+e^- signal (figure 3.13) is a recurrence of the $\omega(782)$ and using equation 3.2; the dotted line is the prediction assuming the e^+e^- signal is a $\phi(1020)$ recurrence.

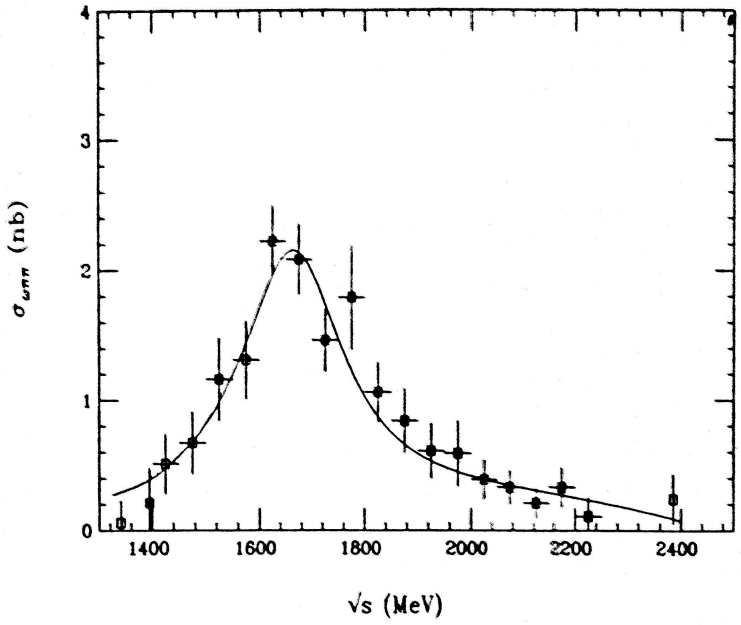

Figure 3.13: DM2 results for $e^+e^- \to \omega\pi\pi$ (from [78]). The $\omega(1650)$ decay dominates the spectrum.

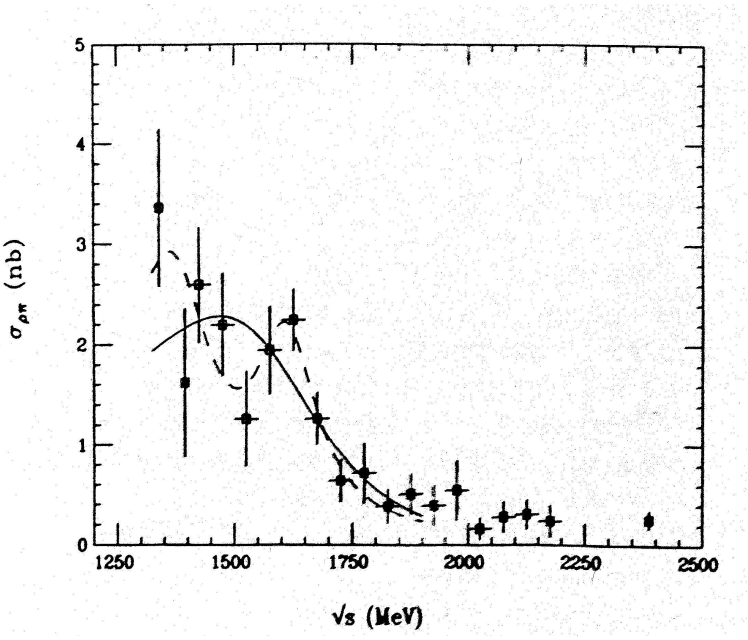

Figure 3.14: DM2 results for $e^+e^- \to \pi^+\pi^-\pi^0$ (from [78]). The solid line is a fit with a very broad Breit-Wigner with a mass around $1500\,\mathrm{MeV/c^2}$. The dashed line is the result of a fit with two interfering Breit-Wigners, the first with a mass around $1400\,\mathrm{MeV/c^2}$, and the second with a mass of $1650\,\mathrm{MeV/c^2}$. This second Breit-Wigner has been argued to be evidence for the $\omega(1650) \to \pi^+\pi^-\pi^0$ decay.

pretation are left unresolved. First, the cross section for photoproducing the $\pi^+\pi^-\pi^0$ enhancement is too large when it is compared to the VDM predictions based on $\rho'(1600)$ (or the modern $\rho(1450)$ or $\rho(1700)$) photoproduction. Second, the cross section for the reaction $e^+e^- \to \pi^+\pi^-\pi^0$ is too small to be consistent with the photoproduction results. Finally, and perhaps most importantly, e^+e^- annihilation observes the $\omega(1650)$ primarily in the $\omega\pi\pi$ final state and weakly, if at all, in the $\pi^+\pi^-\pi^0$ final state, while the photoproduced enhancement has only been observed in $\pi^+\pi^-\pi^0$.

3.3.6 The Story of the "$K^+K^-(1750)$"

The last of the exclusively photoproduced higher mass mesons to be discussed is a K^+K^- state appearing at a mass of $1750\,\mathrm{MeV/c^2}$. Traditionally, this photoproduced enhancement (referred to here as the "$K^+K^-(1750)$") has been interpreted as the $\phi(1680)$, a radial excitation of the $\phi(1020)$ that has been clearly established in e^+e^- annihilation. However, this interpretation has suffered from multiple difficulties ever since the first observation of the $K^+K^-(1750)$ in photoproduction in 1981. In fact, the difficulties with this interpretation have grown with every observation. The analyses of later chapters, based on data from the E831/FOCUS experiment, show conclusively that the $K^+K^-(1750)$ is not the $\phi(1680)$.

The first observation of a high-mass K^+K^- enhancement in photoproduction came in 1981 from the Omega Spectrometer Collaboration [79]. Only a year earlier, DM1 had reported strong evidence for a ϕ' resonance at a mass of $1680\,\mathrm{MeV/c^2}$ in $e^+e^- \to K_S K^\pm\pi^\mp$ [80], and there was some weak evidence for structure at the same mass in

$e^+e^- \to K^+K^-$. Results on both e^+e^- final states were soon published [81, 82] and the state was named the $\phi'(1680)$. The 1981 Omega Spectrometer analysis of the K^+K^- enhancement was strongly influenced by these findings in e^+e^- annihilation. Fitting the K^+K^- mass spectrum using a simple Breit-Wigner for the enhancement and a polynomial for the background gave a mass and width for the $K^+K^-(1750)$ of 1748 ± 11 MeV/c^2 and 80 ± 33 MeV/c^2, respectively. Since this mass was significantly too large to be consistent with the $\phi(1680)$ of e^+e^- annihilation, a more complicated fit was used that incorporated Deck-type effects and interferences to pull the mass down to 1690 ± 10 MeV/c^2 (see figure 3.15). Ever since this first conflation, and in the face of growing inconsistencies, the $K^+K^-(1750)$ has continued to be identified with the $\phi(1680)$, even in the most recent listings of the Particle Data Group [75].

In 1984, the Omega Spectrometer Collaboration performed a search for the $\phi(1680)$ in $K_S K^\pm \pi^\mp$ [83], because the $\phi(1680)$ was seen by e^+e^- annihilation dominantly in $K_S K^\pm \pi^\mp$. Nothing was found. Calculating the expected photoproduced cross section from the $e^+e^- \to \phi(1680) \to K_S K^\pm \pi^\mp$ cross section using equation 3.2, serious inconsistencies with e^+e^- annihilation surfaced (see figure 3.16). The Omega Collaboration was forced to conclude that in order to support the $\phi(1680)$ interpretation of the $K^+K^-(1750)$ one either requires a dramatic breakdown of the VDM relation of equation 3.2 or one must invoke very complicated and implausible interference scenarios.

In 1985, the Omega Spectrometer Collaboration performed another analysis of the K^+K^- final state, this time with more statistics [84]. Fitting with a simple Breit-

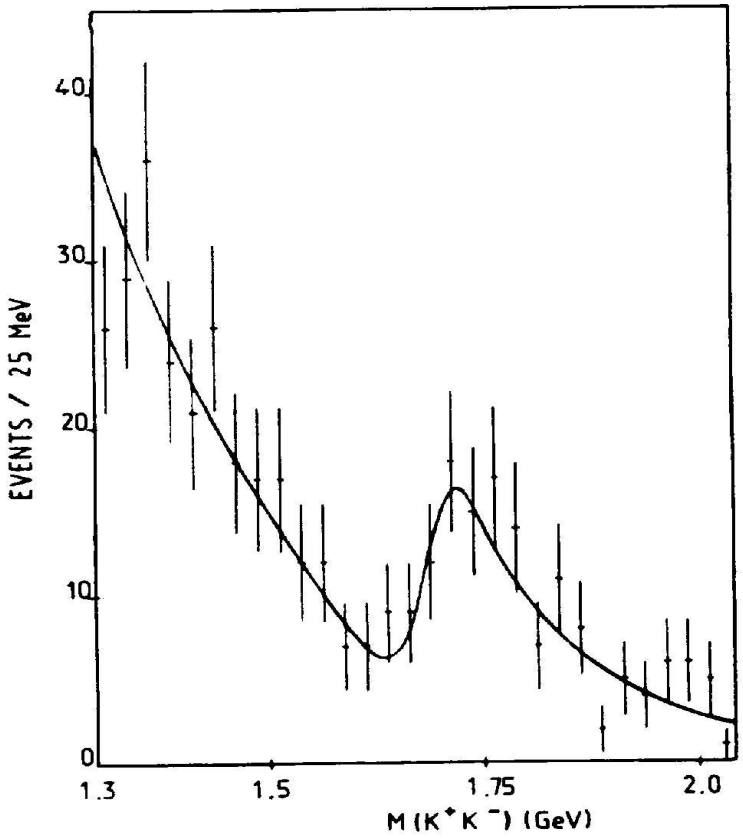

Figure 3.15: Photoproduction of the $K^+K^-(1750)$ as seen by the Omega Spectrometer in 1981 (from [79]). The mass spectrum is fit with a complicated shape that uses interferences with other vector mesons and Deck-like final state interactions, giving a mass measurement of $1690 \pm 10\,\mathrm{MeV/c^2}$. Using a simple Breit-Wigner shape for the fit, the mass is $1748 \pm 11\,\mathrm{MeV/c^2}$.

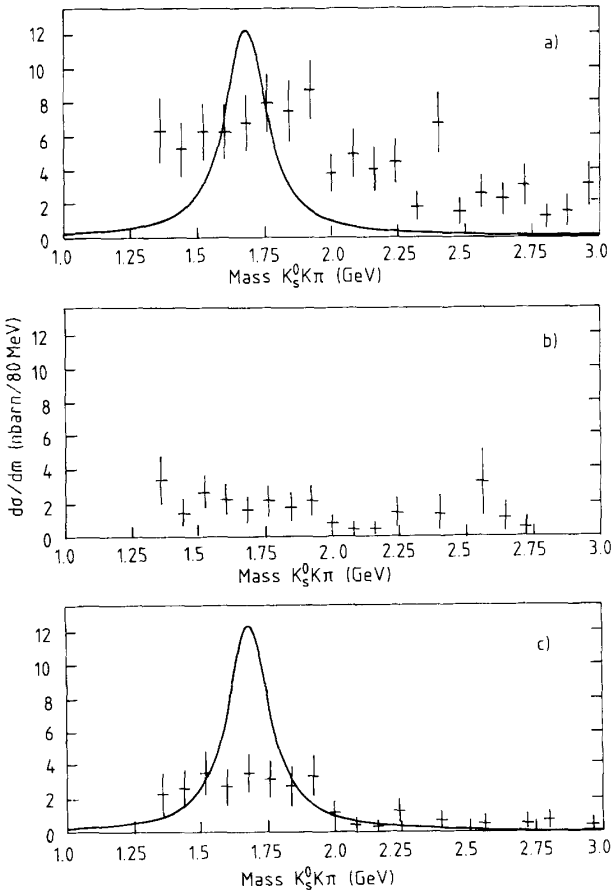

Figure 3.16: A search for the $K^+K^-(1750) \rightarrow K_S K^{\pm}\pi^{\mp}$ decay by the Omega Spectrometer in 1984 (from [83]). Nothing is seen. The solid lines are the predictions from e^+e^- assuming that the $K^+K^-(1750)$ is the same as the $\phi(1680)$ and using equation 3.2. (a) The total $K_S K^{\pm}\pi^{\mp}$ mass spectrum. (b) The $K^{*\pm}K^{\mp}$ spectrum. (c) The $K^{*0}K_S$ spectrum.

Wigner, they found the high-mass K^+K^- enhancement to have a mass of 1760 ± 20 MeV/c^2 (see figure 3.17), again too high to be consistent with the $\phi(1680)$. Furthermore, with these statistics, the complicated 1981 fit was no longer credible.

The final observation of the photoproduced $K^+K^-(1750)$ (until the results of the FOCUS collaboration presented in later chapters) was in 1989 by the E401 experiment at Fermilab [58]. Again the mass was significantly higher than 1680MeV/c^2. With a Breit-Wigner fit, they found the mass and width to be 1726 ± 22MeV/c^2 and 121 ± 47MeV/c^2, respectively (see figure 3.18). With only 123 ± 41 events, E401 was the first to attempt an angular analysis. Based on comparing the t_{20} and t_{40} moments (see chapter 9), they concluded that the $K^+K^-(1750)$ likely had $J^{PC} = 1^{--}$, although the results had almost no statistical significance.

Results from e^+e^- annihilation obtained by the DM2 Collaboration are shown in figures 3.19 and 3.20 for comparison to the photoproduction results. The e^+e^- data is very strong in the $K_SK^\pm\pi^\mp$ final state, coming dominantly through K^*K [85], but is extremely weak in K^+K^- [86], where there is supposed to be a small shoulder at a mass of 1680 MeV/c^2. This is entirely inconsistent with the photoproduced $K^+K^-(1750)$, which appears very strongly in K^+K^- but has never been reported in $K_SK^\pm\pi^\mp$.

Based on inconsistencies between the mass of the $K^+K^-(1750)$ and the $\phi(1680)$, and the dramatic differences in their respective branching ratios to $K_SK^\pm\pi^\mp$ and K^+K^-, it appears unreasonable to identify the $K^+K^-(1750)$ with the $\phi(1680)$. However, despite years of growing inconsistencies, the light meson spectroscopy findings of exclusive

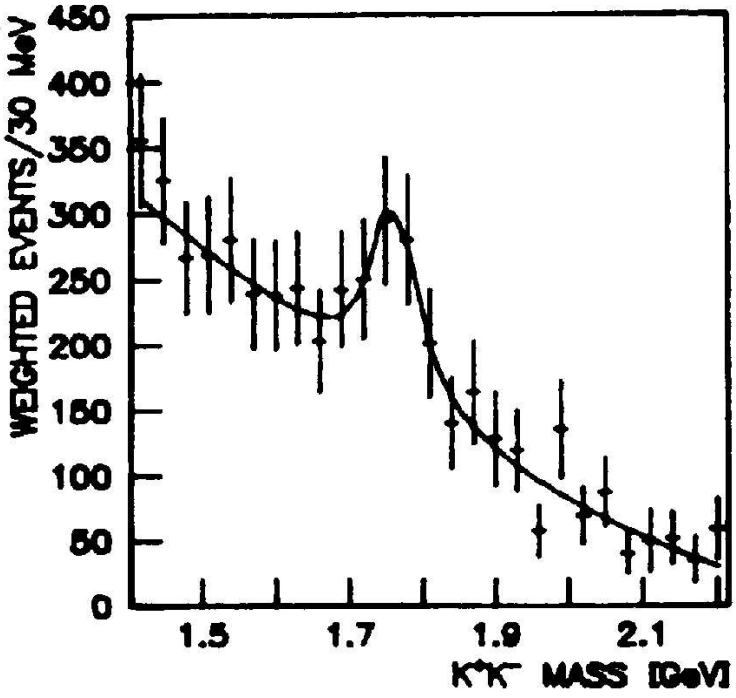

Figure 3.17: Photoproduction of the $K^+K^-(1750)$ as seen by the Omega Spectrometer in 1985 (from [84]). The mass and width were measured to be $1760 \pm 20\,\mathrm{MeV/c^2}$ and $80 \pm 40\,\mathrm{MeV/c^2}$, respectively.

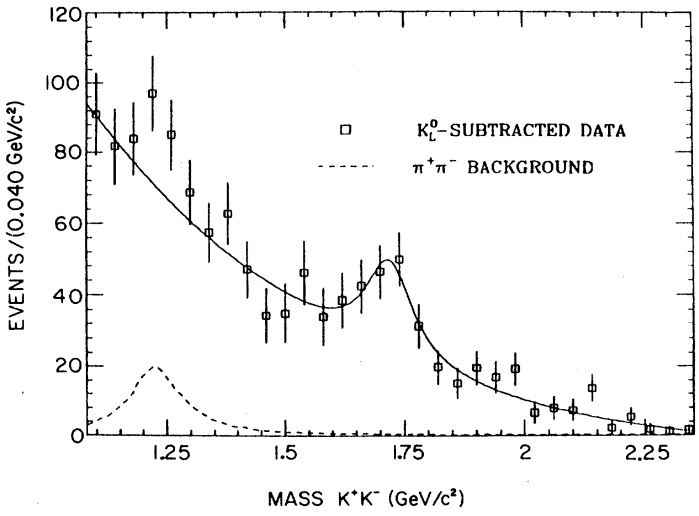

Figure 3.18: Photoproduction of the $K^+K^-(1750)$ as seen by the E401 experiment in 1989 (from [58]). The mass and width were measured to be $1726 \pm 22\,\mathrm{MeV/c^2}$ and $121 \pm 47\,\mathrm{MeV/c^2}$, respectively.

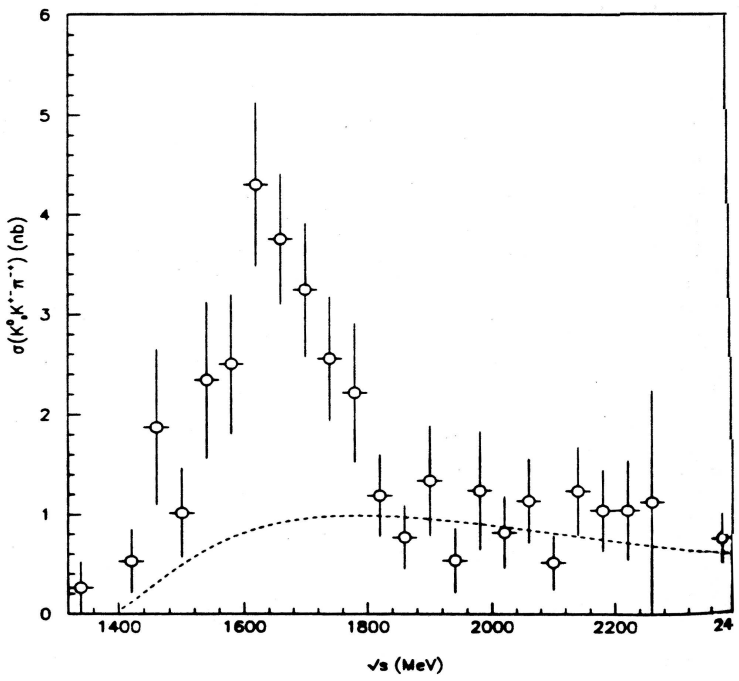

Figure 3.19: DM2 results for $e^+e^- \to K_S K^\pm \pi^\mp$ (from [85]). The $\phi(1680)$ decay dominates the mass spectrum.

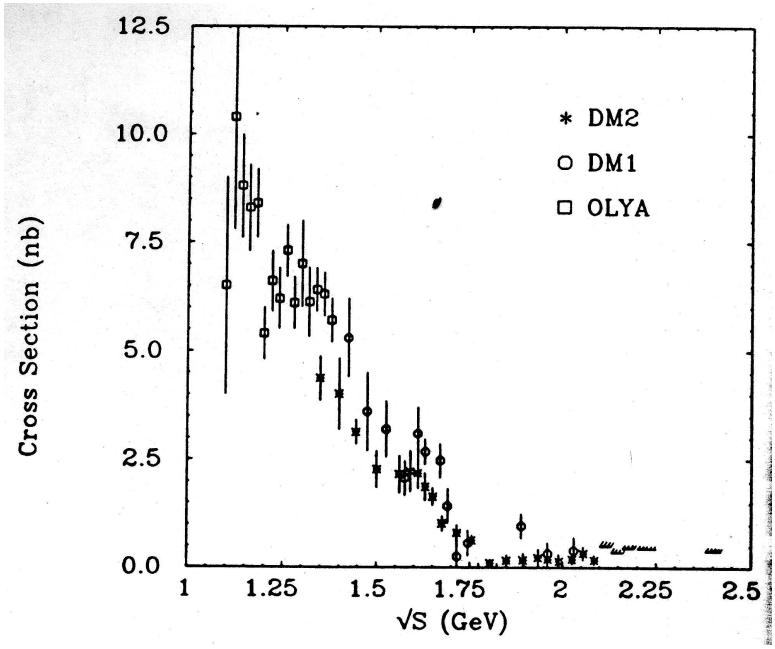

Figure 3.20: DM2 results for $e^+e^- \to K^+K^-$ (from [86]). The $\phi(1680)$ decay appears as a small shoulder around 1680 MeV/c^2.

photoproduction are generally considered to be supplementary to those of e^+e^- annihilation.

3.3.7 Summary

As we have seen, there is much that is left to be understood in the exclusive photoproduction of higher mass mesons. The four photoproduced states discussed above, the $\rho'(1600)$, the $\omega\pi^0(1250)$, the $\omega(1650)$, and the $K^+K^-(1750)$ (previously thought to be the $\phi(1680)$) each present various difficulties. (i) The photoproduced $\rho'(1600)$, in the past often hailed as the best established of all the photoproduced higher mass resonances, is now no longer a resonance at all, but two, the $\rho(1450)$ and the $\rho(1700)$. (ii) The $\omega\pi^0(1250)$ state was first thought to be a vector, as one would initially expect from diffractive photoproduction, but it now appears likely that it is the 1^{+-} $b_1(1235)$. How such a state is photoproduced remains an unanswered question. (iii) The photoproduced enhancement in $\pi^+\pi^-\pi^0$ at a mass near 1650 MeV/c^2 has been naturally interpreted as the $\omega(1650)$ of e^+e^- annihilation, but the absence of the $\omega(1650)$ in the photoproduced $\omega\pi\pi$ final state seriously undermines this interpretation. The nature of the $\pi^+\pi^-\pi^0$ enhancement remains unclear. (iv) The $K^+K^-(1750)$ has long been recognized as having properties inconsistent with the $\phi(1680)$ of photoproduction. The nature of the $K^+K^-(1750)$ will be examined in later chapters, but from the above, it already appears to be inconsistent with any known 1^{--} state.

3.4 Prospects

Fortunately, there are several prospects for understanding the difficulties presented above, and for going beyond them. The E831/FOCUS experiment at Fermilab, to be discussed extensively in later chapters, holds an enormous data sample of exclusive light meson events that lies relatively untouched. While there are limitations within the FOCUS experiment, like non-uniform angular acceptances and poor beam energy resolution, the experiment has an excellent mass resolution and good particle identification capabilities, making it an ideal place to at least study mass spectra. Much more could be said about the $\rho(1450)$ and $\rho(1700)$, for instance, in the $\pi^+\pi^-$, $\pi^+\pi^-\pi^+\pi^-$, and $\pi^+\pi^-\pi^0\pi^0$ final states with more than an order of magnitude more statistics than the last Omega Spectrometer analysis in 1985. Furthermore, the mass and width parameters of the $\omega\pi^0$ state could be more firmly pinned down, agreeing or disagreeing with the parameters of the $b_1(1235)$; and the Omega Spectrometer results in $\pi^+\pi^-\pi^0$ could be confirmed. The analysis that follows in later chapters is an attempt to use the FOCUS data to say more about the photoproduction of the $K^+K^-(1750)$.

The GlueX/Hall-D collaboration[5] at the Continuous Electron Beam Accelerator Facility (CEBAF) of Jefferson Laboratory has plans to exhaustively study photoproduction with a beam energy of 9 GeV. In addition to providing much needed light on older problems, the GlueX/Hall-D collaboration will have the unique capability to

[5]Further information regarding the GlueX/Hall-D experiment currently being planned at the Continuous Electron Beam Accelerator Facility (CEBAF) of Jefferson Laboratory can be found at http://dustbunny.physics.indiana.edu/HallD/

study the spectrum of hybrid mesons. The collaboration plans to use the upgraded 12 GeV electron beam of the CEBAF accelerator to generate 9 GeV photons through the bremsstrahlung process. The beam will be tagged and will have a phenomenal beam energy resolution of 0.1%. Perhaps most promising for the field of light meson spectroscopy, the spectrometer is being designed to have a uniform acceptance over all decay angles, a crucial feature for successful angular analyses. Construction is intended to start in 2004, and physics analyses will begin in 2008.

Chapter 4

The E831/FOCUS Experiment at Fermilab

FOCUS is a high-energy photoproduction experiment that took data during the Fermilab 1996-1997 fixed-target run. A bremsstrahlung-generated photon beam with energies ranging from approximately 20 to 300 GeV was incident on a BeO target. While the primary purpose of the FOCUS experiment is to study the photoproduction of charm and the properties of charmed mesons and baryons, the experiment has also been able to collect an impressive sample of light quark events. This chapter will give a brief overview of the FOCUS experiment and its detector.

4.1 Physics Overview

The FOCUS experiment has been at the forefront of charm physics since its analysis efforts began around 1998. Improving on its predecessor, E687 [87], FOCUS has been able to reconstruct over one million D mesons (see figure 4.1). Over thirty papers have been published on topics such as semileptonic charm decays, charmed baryon lifetimes, CP violation in the charm sector, and the spectroscopy of charmed meson and baryon excited states[1].

In addition to holding one of the world's best samples of charm events, the FOCUS experiment has gathered a sample of light quark events that dominates the samples of earlier photoproduction experiments. In most final states, for example, FOCUS has around ten times the statistics of CERN's Omega Spectrometer [55], one of the last photoproduction experiments to dedicate time to light quark studies. As an example of the FOCUS sample, figure 4.2 shows the $\pi^+\pi^-\pi^0$ mass spectrum, where clear signals for the $\eta(550)$, $\omega(782)$, and $\phi(1020)$ mesons can be seen. The FOCUS experiment thus provides many opportunities to improve upon earlier photoproduction studies.

4.2 The Accelerator

During the Fermilab 1996-1997 fixed-target run, 800 GeV protons from the Fermilab Tevatron were used to feed an array of fixed-target experiments. In the Main Switchyard,

[1] A list of publications and more detail concerning ongoing physics analyses can be found at http://www-focus.fnal.gov/

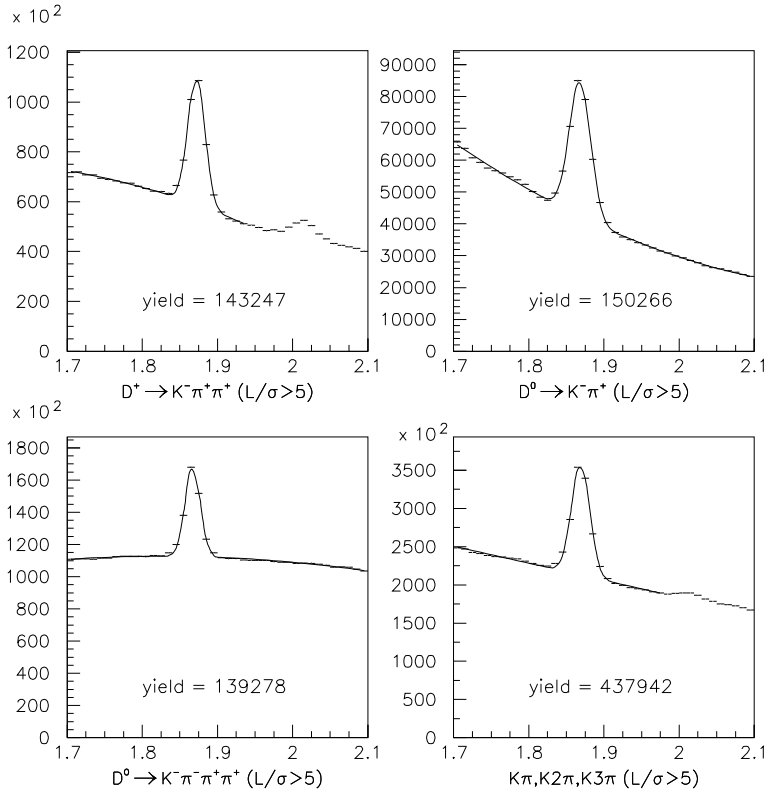

Figure 4.1: The FOCUS D meson signal in three different final states.

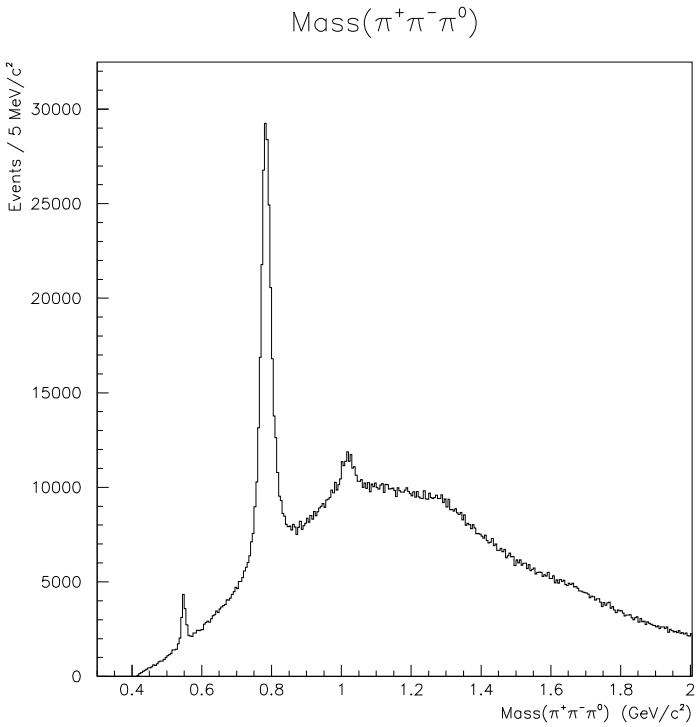

Figure 4.2: The FOCUS $\pi^+\pi^-\pi^0$ mass spectrum from the light quark sample. The $\eta(550)$, $\omega(782)$, and $\phi(1020)$ mesons are clearly visible.

the proton beam extracted from the Tevatron was split into a meson beam line, a neutrino beam line, and a proton beam line. The FOCUS photon beam originated from the proton beam line. Figure 4.3 shows the general layout of Fermilab and the fixed target lines.

The 800 GeV protons of the Tevatron are generated in a series of five stages, each stage increasing the energy of the beam. (1) The process begins with the Cockcroft-Walton, where electrons are added to hydrogen atoms to form negatively charged ions. The negative electric charge allows the H^- ions to be accelerated across an electrostatic gap to an energy of 750 keV. (2) Next, the H^- ions are fed into a linear accelerator (Linac). The Linac accelerates the H^- ions from 750 keV to 400 MeV using a series of RF cavities. Once at the end of the accelerator, the ions are stripped of their electrons in a thin carbon foil, the result of which is a 400 MeV proton beam. (3) From the Linac, the proton beam is picked up by the Booster synchrotron. With a relatively small diameter of 500 feet, the Booster accelerates the protons from 400 MeV to 8 GeV. (4) By way of the Main Injector, the protons are now ready to enter the much larger Main Ring, a synchrotron with a 4 mile circumference housed in the same tunnel as the Tevatron. The Main Ring brings the energy of the protons from 8 GeV up to 150 GeV. (5) In the final stage of acceleration, the protons are transferred from the Main Ring to the Tevatron. Using 1000 superconducting magnets, the Tevatron boosts the proton energy from 150 GeV to its final energy of 800 GeV.

During the fixed-target run period, the Tevatron held 1000 proton bunches sepa-

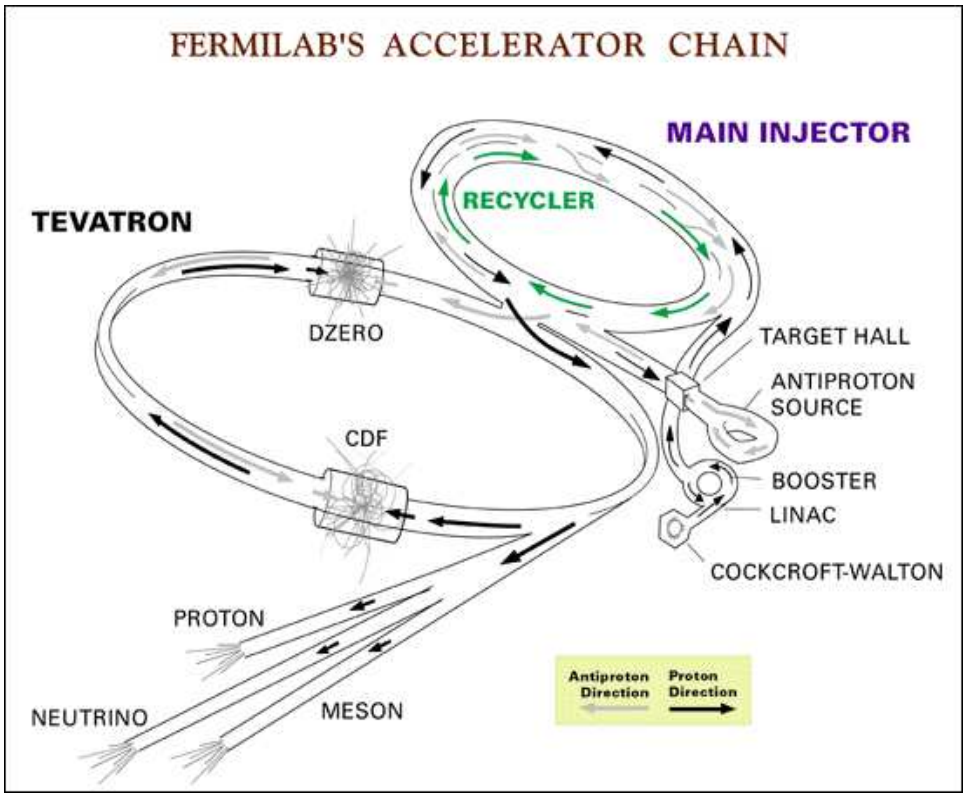

Figure 4.3: A schematic of the layout of the Fermilab accelerator complex.

rated by 20 ns. The acceleration process went through a one minute cycle: 40 seconds were spent filling the Tevatron with 800 GeV protons, and then during the remaining 20 seconds the protons were extracted from the Tevatron and routed through the Main Switchyard. The FOCUS experiment sat in Wideband Hall at the end of the proton fixed target line. Data collection within the FOCUS experiment was divided into separate "runs," periods of roughly one hour of running.

4.3 The Photon Beam

Once the 800 GeV protons have been extracted from the Tevatron and have been sent down the proton fixed target line, the proton beam is converted to a photon beam [88] through a series of stages (see figure 4.4). The process begins 365 meters upstream of the FOCUS experimental target where the 800 GeV proton beam interacts with the 3.6 meter long liquid deuterium production target. This interaction results in a spray of all varieties of charged and neutral particles. The charged particles are swept away by dipole magnets and collimators, leaving only neutral particles, primarily photons, neutrons, and K_L. These neutral particles are sent through a lead converter that converts most of the photons in the neutral beam to e^+e^- pairs. The e^+e^- pairs are guided around a thick beam dump using a series of dipole magnets, and the remaining neutral particles in the beam are absorbed by the dump. The series of dipole magnets leading the e^+e^- pairs around the neutral particle dump consists of (1) the Momentum Dispersing Dipoles, the magnets that initially cause electrons to bend one way

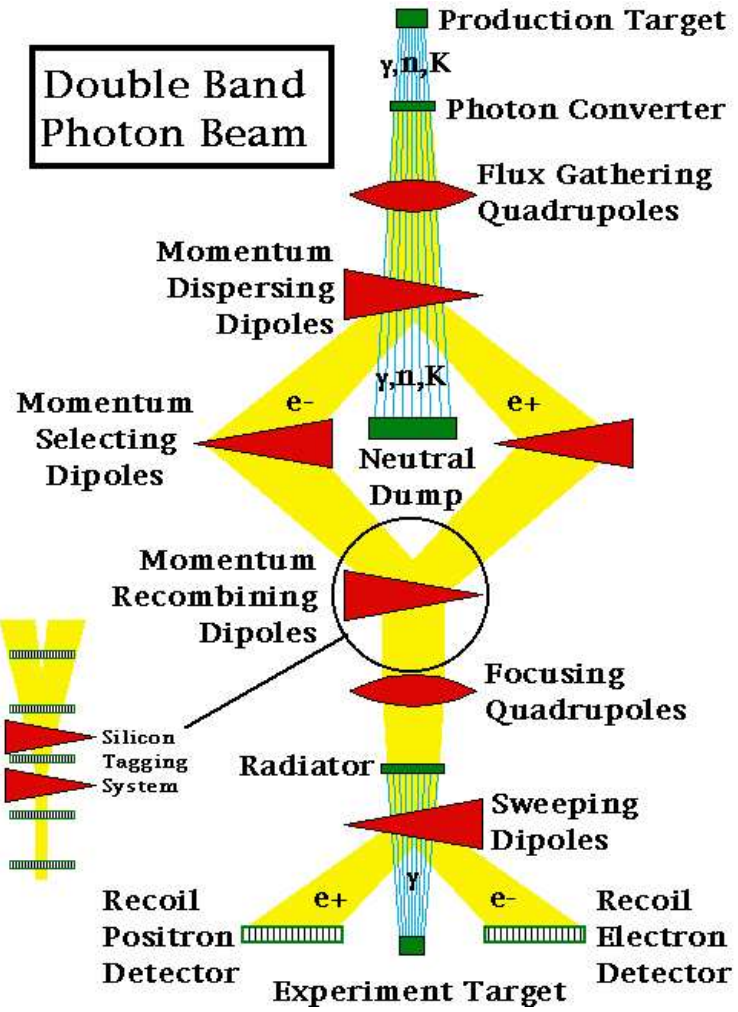

Figure 4.4: Generating the high energy photon beam used by FOCUS.

and positrons the other; (2) the Momentum Selecting Dipoles, which are optimized to select electrons and positrons with momenta around 300 GeV; and (3) the Momentum Recombining Dipoles, the magnets that recombine the electrons and positrons into a single beam. Once around the neutral beam dump, the e^+e^- beam is further focused by the Focusing Quadrupoles.

Now the e^+e^- beam can be used to generate a photon beam using the bremsstrahlung process. About 40 meters upstream from the FOCUS experimental target, the e^+e^- beam is sent through a lead radiator. The individual electrons and positrons radiate photons through bremsstrahlung. Because of the extremely high energy of the e^+e^- beam of around 300 GeV, the radiated photons travel in a direction nearly identical to the original direction of the e^+e^- beam[2]. After radiating, the electrons and positrons are swept into instrumented beam dumps (the Recoil Positron and Recoil Electron detectors) by the Sweeping Dipoles, and only a high energy photon beam remains. The mean photon beam energy is around 150 GeV, but in addition there is a long low energy tail reaching down to around 20 GeV.

Nominally, the energy of each photon in the beam is measured by the beam tagging system. Before entering the Radiator, the energies of the electrons and positrons are measured by a set of five silicon planes interspersed between the Recombining Dipoles. After passing through the Radiator, when the electrons and positrons are swept to opposite sides of the experimental target, their energies are again measured, this time by

[2]The very slight deviations in direction of the resulting photon beam due to the inherent nature of the bremsstrahlung process will later prove to have a significant effect on exclusive light quark studies at low transverse momentum (see chapter 6).

lead-glass calorimeters, the Recoil Electron and Recoil Positron detectors. The energy of the radiated beam photon is then just the difference in energy of the electron (or positron) before and after the Radiator. In the case of a multiple bremsstrahlung event, the energy of the extra noninteracting photons is measured by a small central calorimeter, the Beam Gamma Monitor, and this energy is subtracted from the original measurement. In other words, the tagged photon beam energy (E_{BEAM}) is calculated from:

$$E_{BEAM} = E_{INC} - E_{OUT} - E_{BGM}, \tag{4.1}$$

where E_{INC} is the electron (positron) energy before radiating, E_{OUT} is the electron (positron) energy after radiating, and E_{BGM} is the energy of any additional photons produced in a multiple bremsstrahlung event. The energy resolution of the beam tagging system is around 16 GeV.

4.4 The Spectrometer

The FOCUS detector, building upon the previous E687 photoproduction experiment [87], is a forward multi-particle spectrometer designed to measure the interactions of high energy photons on a segmented BeO target (see figure 4.5). BeO was chosen as the target material in order to maximize the ratio of hadronic interactions to electromagnetic. The target was segmented into four sections to allow for a majority of charmed particles to decay outside of the target material.

Charged particles emerging from the target region are first tracked by two systems

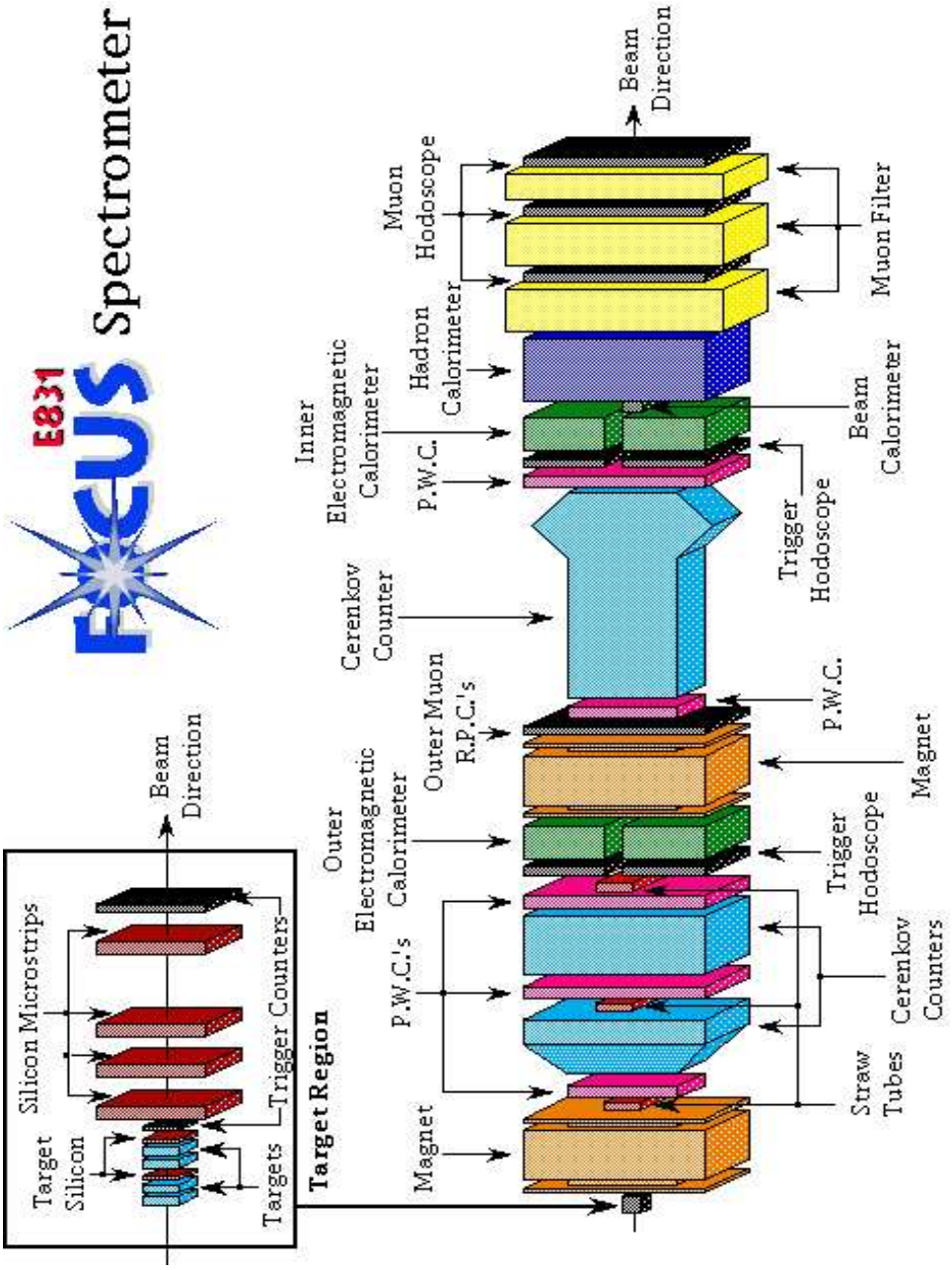

Figure 4.5: The FOCUS spectrometer.

of silicon strip detectors. The upstream system, consisting of four planes (two stations of two views), is interleaved with the experimental target, while the other system lies downstream of the target and consists of twelve planes of microstrips arranged in three views. Once this initial stage of precision tracking is complete, the momentum of a charged particle is determined by measuring its deflections in two analysis magnets of opposite polarity with five stations of multiwire proportional chambers. The measured momentum is used in conjunction with three multicell threshold Cerenkov counters to discriminate between pions, kaons, and protons.

In addition to excellent tracking and particle identification of charged particles, the FOCUS detector provides good reconstruction capabilities for neutral particles. K_S are reconstructed using the "one-bend" approximation described in reference [89]. Photons and π^0 are reconstructed using two electromagnetic calorimeters covering different regions of rapidity.

Three elements of the FOCUS detector are most important for the analysis of the non-charm K^+K^- events. First, the tracking system provides a list of charged tracks and their momenta. Second, the particle identification system classifies the charged tracks as pions, kaons, or protons. Third, the triggering elements require that events satisfy a certain number of requirements before they are recorded. Because of their importance for the K^+K^- analysis in later chapters, these three elements will be described in some detail. Further information on other detector elements (e.g., the calorimeters) can be found elsewhere [90, 91].

4.4.1 Tracking

The purpose of the tracking system is both to reconstruct the paths particles have traveled through the spectrometer and to measure the momenta of these particles. The first task is accomplished by a series of detecting planes normal to the beam direction and placed at advantageous positions throughout the spectrometer. Each plane consists of an array of parallel silicon strips or wires, depending on the detector type, which send out a signal when a charged (ionizing) particle passes in the vicinity. Knowing which wire or strip a particle has passed near or through provides a one-dimensional coordinate of the position of the particle on the detecting plane. By grouping planes at various tilts, or views (see figure 4.6), into stations, an (x,y) coordinate can be calculated at various positions of z, where z is the distance from the target, and x and y are horizontal and vertical coordinates, respectively. Connecting the (x,y) coordinates from station to station (z position to z position) results in a track, the path a charged particle has followed through the spectrometer.

The second task, measuring a track's momentum, is accomplished by observing the deflections of the charged particle in known magnetic fields. In FOCUS, this is accomplished by using two different large aperture dipole magnets. The first magnet (M1) provides a vertical momentum kick of 0.5 GeV/c, while the second magnet (M2) provides a larger vertical momentum kick of 0.85 GeV/c in the opposite direction. Having different strengths for the two magnets allows sensitivity to a larger range of momentum. A low momentum track will be measured well by M1, but may be bent out of

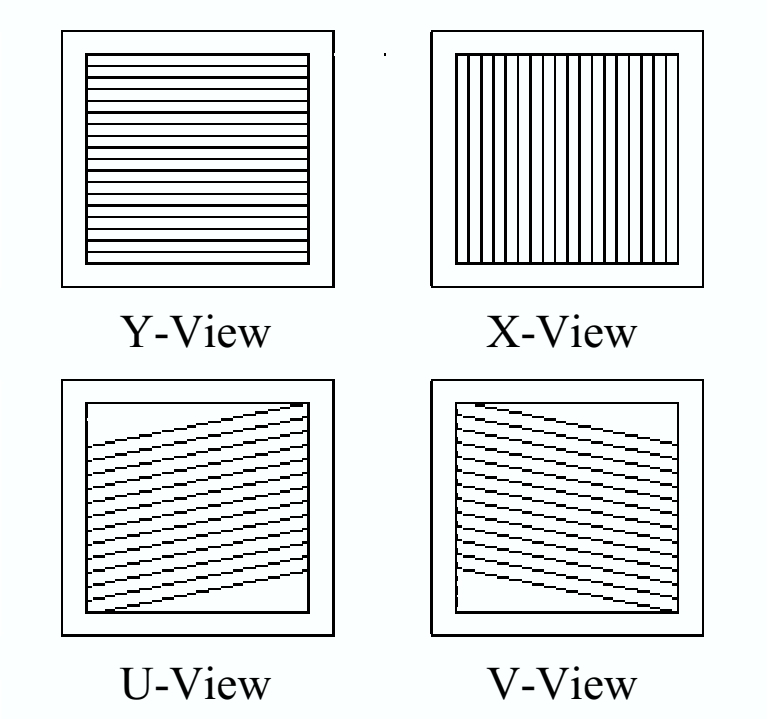

Figure 4.6: A rough sketch of the different PWC views. Charged particles passing through these planes ionize the gas around one of the wires, the charge is collected on the nearest wire, and then recorded, giving a one-dimensional coordinate of the particle. Combining views, the (x,y) position of a particle can be calculated at a given value of z.

the acceptance by M2. A high momentum track may not be deflected enough by M1 for a good momentum measurement, but will be picked up by the stronger M2. The momentum of a track is calculated by using

$$p = \frac{Kick}{\Delta S} \tag{4.2}$$

as the track passes through either magnet, where $Kick$ is the constant momentum kick of one of the magnets and ΔS is the change in vertical slope of the track as it passes through that magnet.

The FOCUS tracking system consists of several distinct subsystems. The upstream system consists of silicon strip detectors placed among the target elements (referred to as the target silicon system [92]) and silicon strip detectors placed just downstream of the target region (referred to as the SSD system). The upstream tracking system is shown in figure 4.7. Charged tracks are followed through the two dipole magnets by the downstream tracking system, which consists of five stations of proportional wire chambers (PWC). Three stations of PWC are between M1 and M2, and two are downstream of M2.

The silicon strip detectors in the upstream system are essentially reverse-biased diodes with charge collecting strips etched on the surface. When a charged particle passes through the interior of the silicon, electron-hole pairs are created. The internal electric field pulls the freed electrons to the surface of the silicon where they are picked up by the conducting strip, amplified, and registered in the data acquisition system.

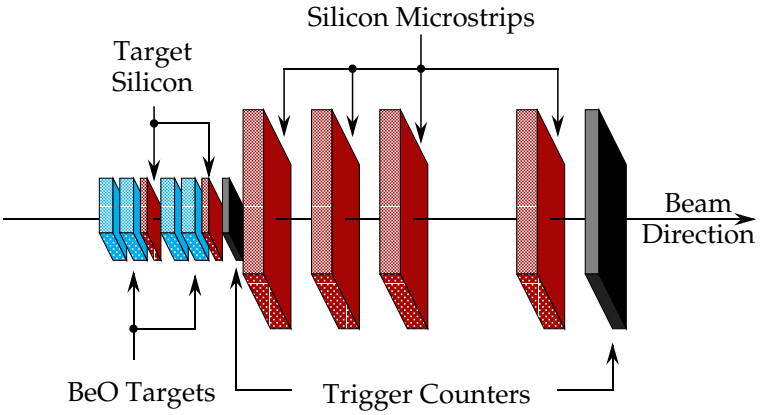

Figure 4.7: The FOCUS target region.

The target silicon system, the silicon strip system placed among the target elements, is composed of two stations of two planes of silicon strip detectors with strips oriented at $\pm 45^\circ$ from the horizontal. The first station is between the second and third target elements, and the second station follows immediately after the last target element (see figure 4.7). The planes are $25 \times 50\,\mathrm{mm}$ in size (the larger dimension is vertical), and the strips have a width of $25\,\mu\mathrm{m}$, giving 1024 different channels per plane.

The SSD system, the second system of silicon strip detectors, begins just downstream of the target system and extends downstream approximately 30 cm, still upstream of the first dipole magnet. It consists of four stations of three planes each with the silicon strips oriented vertically, and $\pm 45^\circ$ from the horizontal. The stations are each 6 cm apart except for the last, which is separated by 12 cm. The first station (i.e., the most upstream) consists of 25 mm long strips. In the central region the strips are $25\,\mu\mathrm{m}$ wide

and in the outer region the strips are 50 μm wide. The other stations consist of 50 mm long strips, with widths of 50 μm in the central region and 100 μm in the outer.

Tracks in the upstream tracking system are found in three steps. First, clusters are formed within each plane. That is, regions where adjacent strips have fired are grouped together. By measuring the amount of charge collected, the cluster is forced to be consistent with having been formed by a single charged track. Second, projections are formed within each station. In other words, clusters within planes are joined to form a very short track segment within a station. Finally, tracks are formed by connecting the station projections. The last step is accomplished by fitting different combinations of station projections with straight lines and taking the best fits to be the tracks.

The downstream tracking system is composed of five stations of proportional wire chambers (PWC). A PWC operates on roughly the same principle as a silicon strip detector. When a charged particle passes through a PWC, the PWC gas is ionized and the ions drift through an electric field and are collected by parallel metal wires. The charge is collected at the end of a wire giving the one-dimensional position of a track. Arranging the PWC planes within a station at various tilts, or views, gives an (x,y) coordinate for a PWC station.

Five stations of four PWC planes each are interspersed throughout the FOCUS spectrometer. The planes within a station are oriented vertically, horizontally, and at $\pm 11.3^\circ$ from the horizontal. The first three stations (most upstream) are placed between M1 and M2, and the last two stations appear downstream of M2 on either side of the last

Cerenkov counter (C3). The first and fourth stations have the dimensions of $76 \times 127\,\mathrm{cm}$ and have a wire spacing of 2 mm. The second, third, and fifth stations are $152 \times 229\,\mathrm{cm}$ and have a wire spacing of 3.3 mm.

Tracks in the downstream system are reconstructed in three steps. First, hits in the planes with vertical strips are connected from station to station with straight lines, referred to as x view tracks. The line segments formed from hits in this view are straight since it is the projection unaffected by the magnetic field, i.e., it is the non-bend view. Second, the other three views (the horizontal wires, and $\pm 11.3^\circ$ wires) are combined within each station to form short projections. Finally, the x view tracks and station projections are combined by fitting to two straight lines, one before M2 and one after, and with a bend parameter to take into account the track's bending through M2.

Once tracks have been found in the upstream and downstream tracking systems, they must be linked together. This is accomplished by refitting all the hits of the upstream and downstream tracks with three straight lines and two bend parameters corresponding to the amount of deflection resulting from M1 and M2. With two opportunities to measure the momentum, tracks can be linked by enforcing consistency. Doubly linked tracks, where one upstream track is linked with two downstream tracks, are allowed to accommodate the possibility of photons converting to e^+e^- pairs that do not significantly separate until after M1.

The momentum resolution for charged tracks depends on the momentum of the track and whether the track has passed through M1 and M2 or just M1. For tracks only

deflected by M1, the resolution is given by:

$$\frac{\sigma_p}{p} = 0.034 * \frac{p}{100\,\mathrm{GeV/c}}\sqrt{1 + (\frac{17\,\mathrm{GeV/c}}{p})^2}. \tag{4.3}$$

For tracks extending through M2 the momentum resolution is:

$$\frac{\sigma_p}{p} = 0.014 * \frac{p}{100\,\mathrm{GeV/c}}\sqrt{1 + (\frac{23\,\mathrm{GeV/c}}{p})^2}. \tag{4.4}$$

For low momentum tracks, the momentum resolution is limited by multiple scattering within the detector material. The momentum resolution for high momentum tracks is limited by the spacing of the wires and strips and uncertainties in the alignment of the detector planes.

4.4.2 Particle Identification

Particle identification in FOCUS is provided by a series of three Cerenkov counters, which are based on the principle that when a particle travels through a medium with a velocity greater than c/n, where c is the speed of light in vacuum and n is the index of refraction of the medium, then the particle will radiate photons. Being sensitive to these radiated photons, a Cerenkov counter can determine whether or not the velocity of a particle is above or below the velocity threshold, c/n. This velocity threshold corresponds to different momenta thresholds for particles of different masses[3], and this is

[3]The momentum of a particle, p, is given by $p = \gamma m v$, where m is the mass of the particle, v is the velocity and $\gamma = (1 - \frac{v^2}{c^2})^{-1/2}$.

Table 4.1: Properties of the three FOCUS Cerenkov detectors.

Counter	Material	$\pi^{\pm}$ Threshold GeV/c	$K^{\pm}$ Threshold GeV/c	$p^{\pm}$ Threshold GeV/c
C1	80% He, 20% N_2	8.4	29.8	56.5
C2	N_2O	4.5	16.0	30.9
C3	He	17.4	61.8	117.0

what allows a Cerenkov counter to distinguish between particle types. For example, if the velocity threshold of a Cerenkov counter were $0.9999\,c$, then the momentum threshold for a pion would be 9.87 GeV/c, while the momentum threshold for a kaon would be 34.9 GeV/c. So, if a track had a momentum of 20 GeV/c, as determined by the tracking system, then the Cerenkov counter would fire if the track were a pion, but would not fire if the track were a kaon. In this particular example, the Cerenkov counter ideally could cleanly distinguish between pions and kaons for all tracks with momenta between 9.87 and 34.9 GeV/c.

By using three different Cerenkov counters filled with gases of different indices of refraction (see table 4.1), FOCUS can cleanly distinguish between pions, kaons, and protons over a wide range of momentum. Now, for example, a 20 GeV/c pion, a 20 GeV/c kaon, and a 20 GeV/c proton will all have different signatures. The pion will fire all three counters C1, C2, and C3; the kaon will only fire C2; and the proton will not radiate at all. Notice that there is ideally a clean separation between pions and kaons with momenta all the way from 4.5 GeV/c to 61.8 GeV/c. E687 used a particle identification system based only on these thresholds and logic tables.

FOCUS has improved on this system by measuring the angle with which photons are

radiated by a particle traveling with a velocity above threshold. This provides additional information about the particle's velocity, v, since the angle of radiation, θ, is given by

$$\cos\theta = \frac{c}{nv}. \tag{4.5}$$

So, the higher the velocity is above threshold, the bigger the ring of the emitted photons will be. The measurement of the angle has been made possible by dividing the back of the Cerenkov counters into arrays of cells, with smaller cells near the center of the counter and larger cells further out from the center.

FOCUS has implemented a system called CITADL for particle identification based on the detected rings in the counters [93]. The CITADL system works by assigning likelihoods to different particle hypotheses. For example, if a particle of given momentum (measured by the tracking system) were a pion, then we can calculate its velocity and the angles of radiation and thus know which cells in which counters should have fired. The likelihood for the pion hypothesis is then calculated based on the status of these cells. If a given cell should be on given the pion hypothesis, and the cell was found to be on, then the total likelihood for the pion hypothesis receives a contribution of

$$L_{\text{cell}} = (1 - e^{-\mu}) + a - a(1 - e^{-\mu}), \tag{4.6}$$

where μ is the expected number of photoelectrons in the cell, a is the accidental firing rate, and Poisson statistics has been assumed. If the cell was found to be off, then the

total likelihood receives a contribution of

$$L_{\text{cell}} = 1 - [(1 - e^{-\mu}) + a - a(1 - e^{-\mu})]. \tag{4.7}$$

The likelihoods are summed over all the cells in the ring of cells that should have fired given the pion hypothesis to give a total likelihood for the pion hypothesis:

$$L_{\pi} = \sum_{\text{cells}} L_{\text{cell}}. \tag{4.8}$$

Similarly, likelihoods are calculated for the $e^{\pm}$, $K^{\pm}$, and $p^{\pm}$ particle hypotheses.

To convert the likelihoods to χ^2-like measures, the CITADL system introduces the variables

$$W_i = -2\ln(L_i), \tag{4.9}$$

where i indicates the hypothesis under consideration, i.e., either $e^{\pm}$, $\pi^{\pm}$, $K^{\pm}$, or $p^{\pm}$. The W_i with the lowest value indicates the most likely particle hypothesis. Since kaons and pions dominate the hadronic final states, useful parameters for particle identification are the pionicity, defined as

$$\text{Pionicity} \equiv \text{W}_\text{K} - \text{W}_{\pi}, \tag{4.10}$$

and the kaonicity, defined as

$$\text{Kaonicity} \equiv \mathrm{W}_{\pi} - \mathrm{W}_{\mathrm{K}}. \tag{4.11}$$

Increasing the kaonicity requirement, for example, decreases the chances a pion will be misidentified as a kaon.

An example of the effect of kaonicity on kaon identification can be seen in figure 4.8 where a sample of putative K^+K^- events has been selected using various kaonicity criteria. Figure 4.8.a shows the mass spectrum of these events plotted as if they were $\pi^+\pi^-$ events. With the loosest kaonicity requirement, kaonicity > 1.4 for both kaons, the $\rho(770) \to \pi^+\pi^-$ decay is clearly visible, indicating that many of the putative K^+K^- pairs are misidentified $\pi^+\pi^-$ pairs. Tightening the kaonicity requirement from 1.4 to 2.6 to 6.0 for both kaons, the pion contamination is greatly reduced and the $\rho(770)$ signal disappears. In the K^+K^- mass spectrum (figure 4.8.b), the $\rho(770)$ signal manifests itself as a broad enhancement at a mass of around $1200\,\mathrm{MeV/c^2}$ for the loosest kaonicity requirement, and disappears as the kaonicity criteria are tightened.

4.4.3 Triggers

Whenever an interesting event occurs in the detector, data must be read out and stored. The trigger system is responsible for discriminating between interesting and uninteresting events. The trigger decision takes place in several stages and there are several different triggers based on different physics questions. The data for the K^+K^- analyses

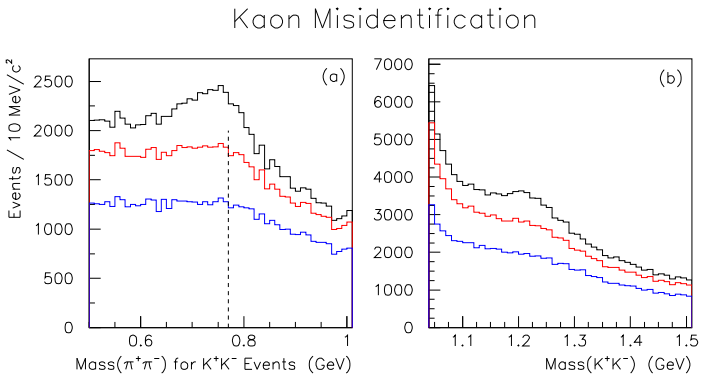

Figure 4.8: The effect of kaonicity on kaon misidentification. (a) The mass spectrum for putative K^+K^- events plotted as if they were $\pi^+\pi^-$ events. The appearance of the $\rho(770) \rightarrow \pi^+\pi^-$ decay indicates misidentification. The dashed line marks the $\rho(770)$ mass. The black line is the mass spectrum for the loosest kaonicity requirement: kaonicity > 1.4 for both kaons. The red and blue lines are for kaonicity greater than 2.6 and 6.0, respectively, for both kaons. (b) The corresponding K^+K^- mass spectrum for the same series of kaonicity requirements.

included in the remaining chapters are obtained through the hadronic trigger. While triggering elements are located throughout the spectrometer and serve various purposes, the hadronic trigger imposes only three simple criteria on events.

First, like all other triggers, the hadronic trigger requires a coincidence in TR1 and TR2. TR1 is just downstream of the target assembly, and TR2 is just downstream of the SSD system. A coincidence in TR1 and TR2 guarantees that at least one charged track has passed through the SSD system (see figure 4.7).

Second, in addition to having tracks in the SSD system, the hadronic trigger requires at least two charged tracks traverse the entire downstream tracking system. The OH and H$\times$V detectors are located just after the last PWC station and are designed to count charged tracks. The H$\times$V detector covers the inner region of the acceptance and the OH detector covers the outer region. The hadronic trigger requires either two charged tracks be detected by the H$\times$V or one charged track register in the H$\times$V and one in the OH. Both the H$\times$V and the OH include a vertical gap from top to bottom to allow e^+e^- pairs to pass. Unfortunately, the presence of this gap has a large influence on shaping the angular acceptances of light quark meson decays (see chapter 6).

Finally, a minimum hadronic energy of 18 GeV as determined by the hadronic calorimeter is an additional requirement imposed by the hadronic trigger. This requirement ensures the presence of hadronic tracks (as opposed to $e^{\pm}$ tracks).

4.5 Data Collection

Over the course of its running, the FOCUS experiment collected 6.5 billion events recorded on 5926 tapes, each tape holding 4.5 Gigabytes of data. The data was collected over approximately 6500 runs, each run corresponding to roughly one hour of running time. The data was processed in four separate stages.

(1) PassOne was where all the major reconstruction was performed, e.g., track reconstruction and particle identification.

(2) Skim1 separated the PassOne output into six large superstreams based on different physics criteria. The light quark superstream was separated from charm superstreams by requiring each track of an event to originate from a vertex within one of the target elements, unless the tracks came from a K_S meson or Λ baryon, each of which can travel some distance before decaying.

(3) In Skim2, the superstreams were separated into separate substreams by requiring more specific physics criteria. No significant new requirements were added to the light quark sample.

(4) In the final stage, the light quark data was compacted into a form that could be stored on the computers at the University of Tennessee. Events were selected that had total electric charge of 0 or ± 1, a balanced strangeness (e.g., every K^+ had a K^- or K_S), a single vertex within one of the four target elements, and greater than or equal to two particles coming from that vertex. In addition, no more than four photons were allowed in an event. To limit the size of the data sample even further, events with only

pions were required to originate from the last target element. This last stage of data collection resulted in 123 tapes holding a total of around 350 million events.

Chapter 5

Measuring the Beam Parameters

A good understanding of both the energy and the direction of the photon beam on an event by event basis is essential for studying the exclusive photoproduction of light mesons. A precise determination of the beam energy distribution associated with the production of a meson, for example, can serve to distinguish between production mechanisms, since different production mechanisms generally have different dependencies on beam energy. Another method for distinguishing between production mechanisms, measuring the transverse momentum (p_T) distribution of meson production, which is the distribution of meson momenta transverse to the photon beam direction, crucially depends on an accurate knowledge of the photon beam direction. Furthermore, both the energy and the direction of the photon beam are used in defining the Gottfried-Jackson coordinate system of resonance decay angles. Small uncertainties in the beam parameters, especially uncertainties in the beam direction, can thus have serious conse-

quences for an angular analysis, as will be shown in chapter 6. This chapter discusses the estimates of beam energy and beam direction and their uncertainties that have been adopted in the FOCUS light meson spectroscopy analyses.

5.1 The Beam Energy

Nominally, the energy of each photon in the beam is determined by the beam tagging system, which gives the energy of the beam photon by measuring the energy of an electron or positron before and after bremsstrahlung (see section 4.3). However, since the efficiency of the tagging system drops severely for beam energies below around 150 GeV, the beam tagging information was rarely available for light quark final states that favor a smaller beam energy. Less than 5% of all K^+K^- events, for example, have beam tagging information. Therefore, in place of the beam tagging system, we have estimated the beam energy (E_{BEAM}) for a given event as the sum of the energies (E_i) of all charged tracks in the event plus the energies found in the inner and outer electromagnetic calorimeters (E_{IE} and E_{OE}, respectively):

$$E_{BEAM} \approx \sum_i E_i + E_{IE} + E_{OE}. \tag{5.1}$$

Figure 5.1 compares the beam energy distributions for K^+K^- events resulting from the beam tagging system with the beam energy distributions obtained from the above estimate. For uniformity, and to simplify efficiency calculations, all analyses use only

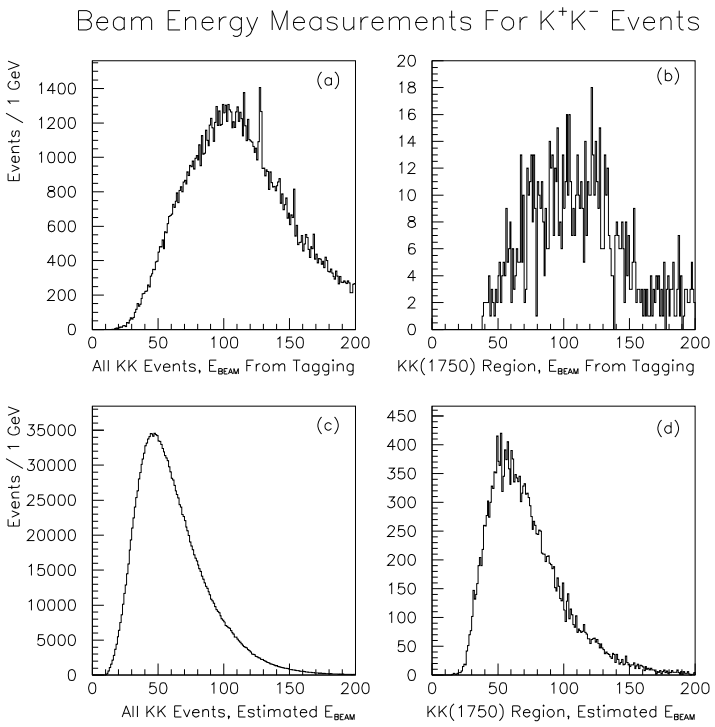

Figure 5.1: Beam energy distributions for exclusive K^+K^- events measured using two different methods. (a) The beam energy from the tagging system for all K^+K^- events. (b) The beam energy from the tagging system for K^+K^- events in the $K^+K^-(1750)$ signal region ($1640 < M(K^+K^-) < 1860\,\mathrm{MeV/c^2}$). (c) The estimated beam energy for all K^+K^- events from equation 5.1. (d) The estimated beam energy for K^+K^- events in the $K^+K^-(1750)$ signal region.

the estimated beam energy.

The mean beam energy for charm analyses is typically around 150 GeV, whereas the mean beam energy is much lower for the exclusive light quark analyses. The K^+K^- sample of events, for example, has a beam energy distribution that peaks around 50 GeV. This difference in mean beam energies primarily results from the criteria used for identification of the charged kaons. If the beam energy is large and the momentum transferred to the target is small, the produced K^+ and K^- mesons carry too large of a momentum to be uniquely identified by the Cerenkov system. Charged kaons can be cleanly separated from pions by the Cerenkov system, for example, only when they have a momentum lying below 61.8 GeV/c (see table 4.1). This then sets an approximate upper limit to the incoming photon beam momentum.

5.2 The Beam Energy Resolution

The resolution of the estimated beam energy (equation 5.1) has been estimated through a Monte Carlo simulation (see chapter 6 for the general Monte Carlo method). A sample of K^+K^- events was generated with beam energy flat between 10 and 160 GeV, transverse momentum between 0.0 and 0.3 GeV/c, and K^+K^- mass between 1.0 and 2.8 GeV/c^2. Figure 5.2 shows the difference between generated and reconstructed beam energies for various beam energy ranges of K^+K^- events. The beam energy is noticeably underestimated at low beam energies (e.g., E_{BEAM} between 40 and 70 GeV) due to missing energy in the detector, but the difference goes away quickly at higher beam

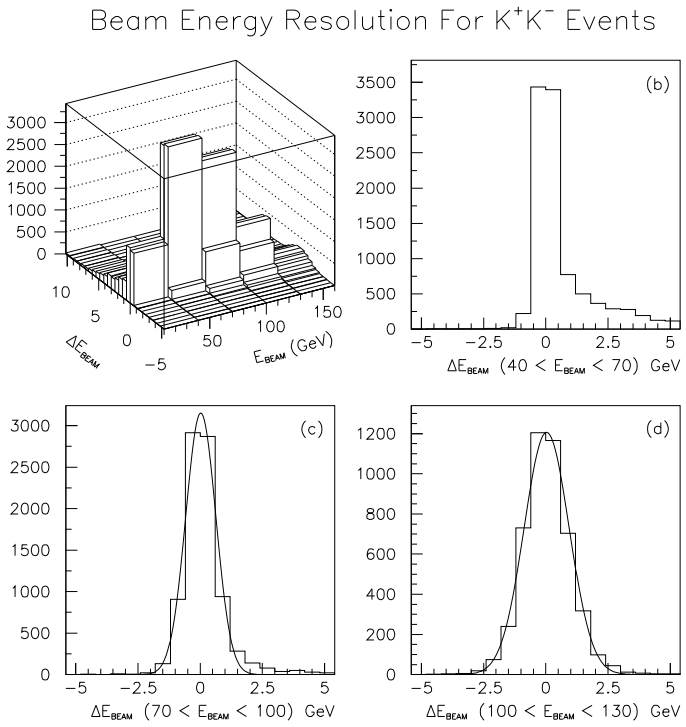

Figure 5.2: The resolution of the estimated beam energy. (a) The generated minus reconstructed beam energy (ΔE_{BEAM}) versus generated beam energy. (b) ΔE_{BEAM} for $40 < E_{BEAM} < 70\,\text{GeV}$. (c) ΔE_{BEAM} for $70 < E_{BEAM} < 100\,\text{GeV}$ fit with a Gaussian distribution of width $0.605 \pm 0.006\,\text{GeV}$. (d) ΔE_{BEAM} for $100 < E_{BEAM} < 130\,\text{GeV}$ fit with a Gaussian distribution of width $0.905 \pm 0.011\,\text{GeV}$.

energies (e.g., E_{BEAM} between 70 and 100 GeV) where the K^+K^- pairs are more forward. Fitting the higher beam energy ranges with Gaussian distributions, we estimate the beam energy resolution to be less than 1 GeV (0.605 ± 0.006 GeV for $70 < E_{BEAM} < 100$ GeV and 0.905 ± 0.011 GeV for $100 < E_{BEAM} < 130$ GeV). The resolution was found to be independent of the K^+K^- mass.

5.3 The Beam Direction

Rather than precisely following the z-direction defined by the detector, the mean photon beam direction has been found to vary slightly from run to run. These variations are in addition to event by event variations due to the inherent nature of the bremsstrahlung process (described in section 4.3). While there is no method available for measuring the beam direction for every event, which thus translates into an overall uncertainty in the beam direction, the mean beam direction for every run can be estimated. For each event in a run, the momenta of all the charged tracks were added together and a unit vector was defined in the direction of the resultant momentum. Then all the unit vectors within a run were averaged and the direction of the average unit vector was used as the direction of the beam for the specific run. This method was followed independently of any specific analyses, and the mean beam directions were determined by using all of the events in the light quark data sample.

Figure 5.3 shows the mean angles (θ is the polar angle and ϕ is the azimuthal angle) for each run as determined by this method. The mean values for the average θ angles

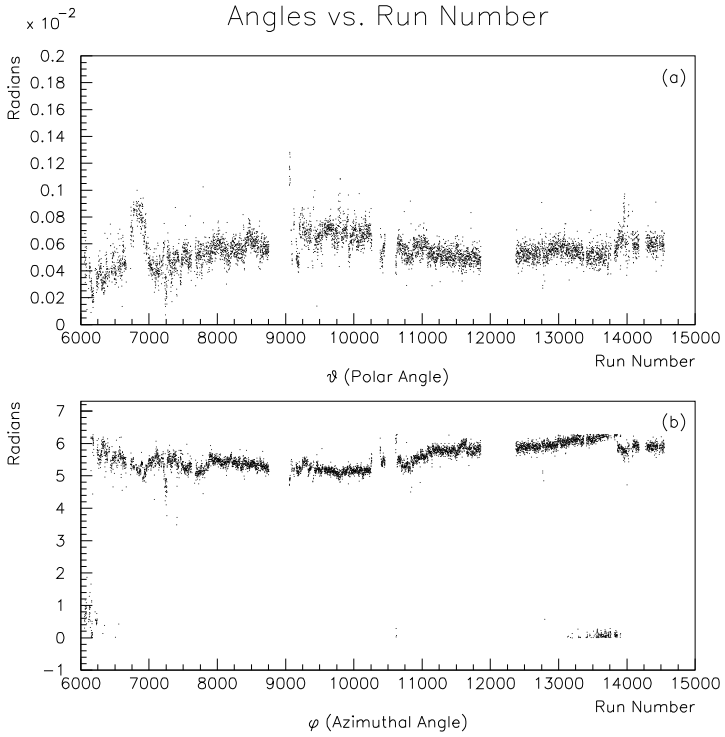

Figure 5.3: Estimates of the beam direction on a run by run basis. (a) The mean θ (polar angle) of the beam direction for each event in a run versus the run number. (b) The mean ϕ (azimuthal angle) of the beam direction versus the run number.

are consistent with the estimate of 600 micro-radians that was determined by using embedded pairs, beam photons that convert to e^+e^- pairs without deflection.

Using the mean beam direction for each run rather than simply using the z-direction of the detector for the beam direction has a noticeable effect on the K^+K^- t' spectrum, serving to steepen the diffractive slope[1]. This is the effect one should expect. If the beam direction used in calculations is inaccurate, then the average transverse momentum of the K^+K^- pairs will be overestimated, and hence the steepness of the t' slope will be underestimated. Using a more accurate value for the beam direction then steepens the K^+K^- t' spectrum. Before the beam direction correction, the t' slope for K^+K^- events in the $\phi(1020)$ region was $75.37 \pm 0.52\,\mathrm{GeV}^{-2}\mathrm{c}^2$; after the correction it is $77.22 \pm 0.42\,\mathrm{GeV}^{-2}\mathrm{c}^2$. Similarly, the slope in the $K^+K^-(1750)$ region steepens from 57.2 ± 2.0 to $66.8 \pm 1.7\,\mathrm{GeV}^{-2}\mathrm{c}^2$. Figure 5.4 shows this effect in the $K^+K^-(1750)$ region.

5.4 Uncertainty in the Beam Direction

The mean direction of the photon beam varies from run to run and this mean direction, as determined above, is used as the beam direction for all events within any run. But in addition to the run to run variations, the beam direction varies slightly from event to event due to the nature of the bremsstrahlung production of the beam. Thus, there is an inherent uncertainty in the beam direction for any given event.

In order to estimate this uncertainty in the beam direction, the following method

[1]The K^+K^- t' distribution is always fit with two exponentials, $a_1 e^{-b_1 t'} + a_2 e^{-b_2 t'}$. The "diffractive" slope is the larger of the two slopes b_1 and b_2. For more information on kinematics, see appendix B.

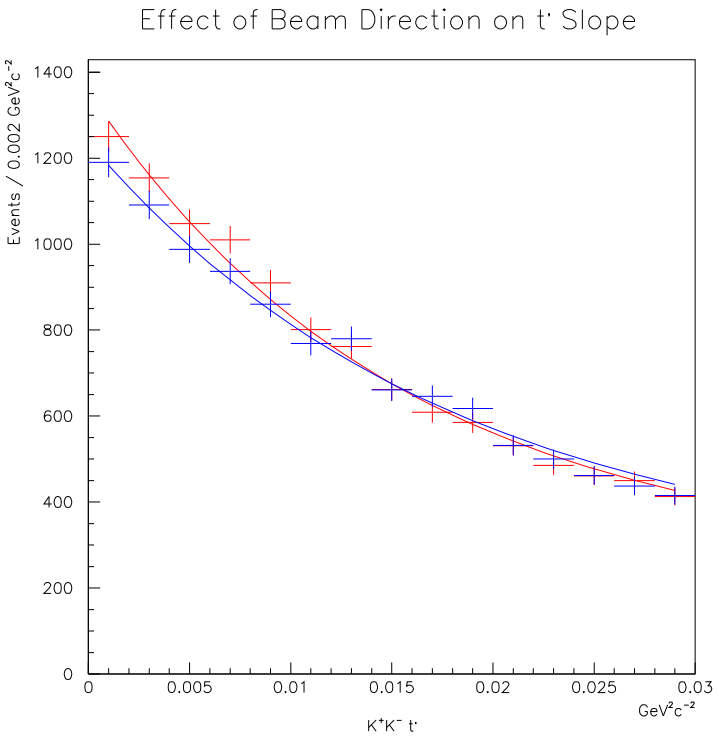

Figure 5.4: The effect of the beam direction corrections on the t' distribution of K^+K^- events in the $K^+K^-(1750)$ mass region. The blue points are the t' distribution using the z-direction as the photon beam direction; the red are the t' distribution obtained by using the mean beam direction for each run. Both distributions are fit with two exponentials. The measured t' distribution becomes noticeably steeper when the mean beam direction is used, the diffractive slope changing from 57.2 ± 2.0 to $66.8 \pm 1.7\,\mathrm{GeV}^{-2}\mathrm{c}^2$.

was used. A unit vector for each event within a run was defined in the direction of the total momentum of all charged tracks and the x and y direction cosines for each of these unit vectors was plotted for a given run. The uncertainty in the beam direction is assumed to be related to the spread in these x and y direction cosines. Figure 5.5 shows the x versus y direction cosines for run number 9500, which is typical of all runs. Notice the sharp peak in the center of the distribution. The width of this peak, 0.001 in both the x and y direction cosines, has been taken to be an estimate of the resolution of the beam direction. This is again consistent with the estimate from embedded pairs and will be used later in chapter 6 where the t' and decay angle resolutions are discussed.

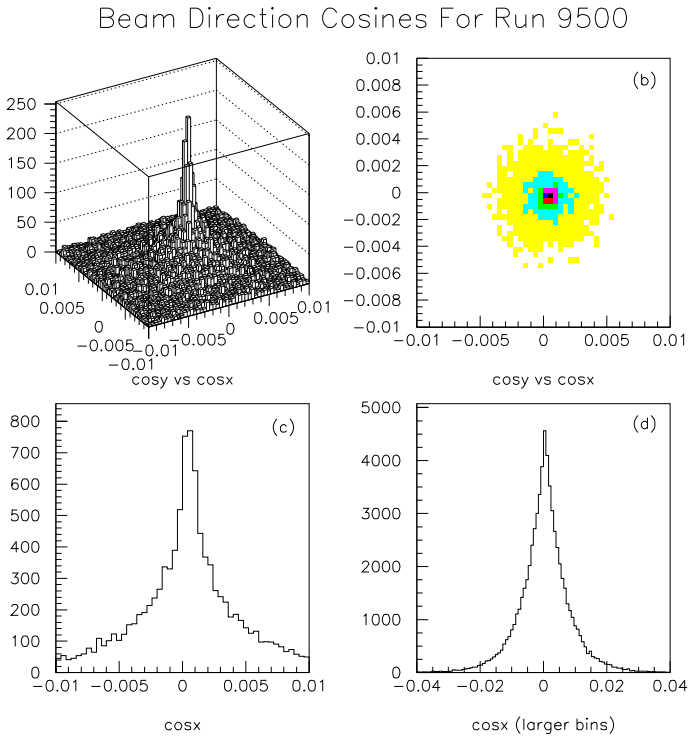

Figure 5.5: Estimating the uncertainty in the beam direction. (a) The x direction cosine versus the y direction cosine for the momenta of all events in run number 9500. (b) The same shown as a color plot. (c) The same projected onto the x-axis. (d) The same with larger bin sizes. The beam direction resolution is estimated to be 0.001 in both the x and y direction cosines, which is the width of the narrow spike appearing in the center of the distribution.

Chapter 6

Monte Carlo Studies of the Detector

An event of the type $\gamma N \to XN$, where X subsequently decays into two bodies (e.g., $X \to K^+K^-$) or undergoes a series of two body decays (e.g., $X \to K^*K$ and then $K^* \to K\pi$), can be completely described kinematically by the beam energy (E_{BEAM}), the mass of X (M_X), the transverse momentum (p_T) of X (averaging over the physically meaningless azimuthal angle of the X momentum)[1], and two decay angles for each two body decay (the polar and azimuthal angles, θ and ϕ). Thus, an event of the type $\gamma N \to XN \to K^+K^-N$ is completely described by five variables: E_{BEAM}, M_X, p_T, $\cos\theta_X$, and ϕ_X; and an event of the type $\gamma N \to XN \to K^*KN \to K_SK^\pm\pi^\mp N$ is

[1] Sometimes it is desirable to use $p_T^2 \approx t'$ rather than p_T. Of course, either can be treated as one of the fundamental kinematic variables. For more detailed information on the kinematics of photoproduction, see appendix B.

described by seven: E_{BEAM}, M_X, p_T, $\cos\theta_X$, ϕ_X, $\cos\theta_{K^*}$, and ϕ_{K^*}. If these parameters are treated as the fundamental parameters of the analysis, then it becomes important to understand the way they are measured within the detector and reconstructed by the analysis programs. This chapter will describe the general characteristics of the resolutions and efficiencies of the detector as studied by Monte Carlo simulations.

6.1 Monte Carlo Studies of the Resolution

The resolution of a given parameter corresponds to the accuracy with which it can be measured, or the statistical error associated with the measurement. Estimates of the statistical errors of given parameters can often be obtained through Monte Carlo simulations of the detector, where events with known parameters are processed through a full detector simulation program and are then reconstructed and analyzed in the same way the actual physical data is reconstructed and analyzed. Comparing the initial "generated" events (the events before they have been touched by the detector simulation) with the "reconstructed" events (the events after they have been sent through the simulated detector and reconstructed) gives a sense of the way the parameters of interest are measured within the detector and reconstructed by the reconstruction algorithms. The statistical errors associated with the reconstructed events can then be applied to the "raw" data, the real physical data that has been gathered in the actual experiment.

6.1.1 The K^+K^- Mass Resolution

In order to confidently study the mass and width of the $K^+K^-(1750)$ resonance (to be presented in chapter 7), it is first necessary to understand the resolution with which the K^+K^- mass spectrum has been measured. This K^+K^- mass resolution has been studied by generating 100,000 Monte Carlo events with a K^+K^- mass of $1750\,\mathrm{MeV/c^2}$, beam energy flat between 10 and 160 GeV, and the transverse momentum (p_T) of the K^+K^- system flat between 0.0 and 0.3 GeV/c. These events were sent through the detector simulation program and then reconstructed with the same analysis code as was used in the K^+K^- analysis. Figure 6.1 shows reconstructed mass distributions for various regions of beam energy. The resolution is the width of the Gaussian fit to the reconstructed Monte Carlo data. While the mass resolution has been found to be independent of the cut on p_T, the mass resolution is $8.89 \pm 0.13\,\mathrm{MeV/c^2}$ for the lowest beam energy range (between 10 and 40 GeV, figure 6.1.a) and rises to $12.49 \pm 0.29\,\mathrm{MeV/c^2}$ for the highest beam energy range (between 130 and 160 GeV, figure 6.1.b).

Figure 6.2.a shows the effects of 72 different cut combinations on the K^+K^- mass resolution at a mass of $1750\,\mathrm{MeV/c^2}$. The cut variations represent four ranges of p_T: cuts 1 – 18, p_T less than 0.30 GeV/c; cuts 19 – 36, p_T less than 0.10 GeV/c; cuts 37 – 54, p_T less than 0.15 GeV/c; and cuts 55 – 72, p_T less than 0.20 GeV/c. Within these there are six ranges of beam energy: (1) 10 – 160 GeV; (2) 10 – 40 GeV; (3) 40 – 70 GeV; (4) 70 – 100 GeV; (5) 100 – 130 GeV; and (6) 130 – 160 GeV. Within these there are three ranges of particle ID cuts: (1) kaonicity greater than 1.4 for both kaons;

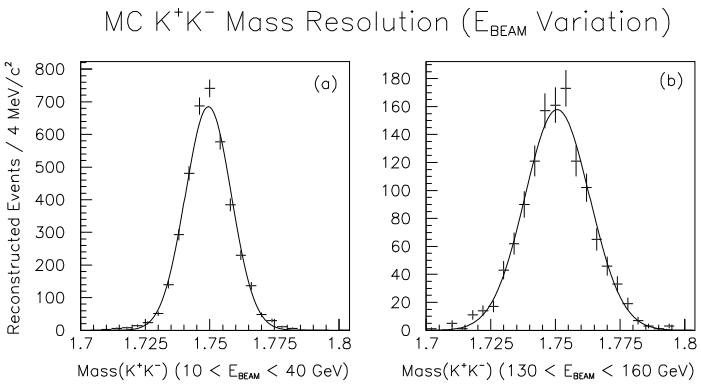

Figure 6.1: Reconstructed Monte Carlo K^+K^- mass distributions. Two different ranges of beam energy are shown (with the loosest particle ID requirements, and p_T flat between 0.0 and 0.15 GeV/c). The events were generated at a single mass value of 1750 $\mathrm{MeV/c^2}$. The mass resolution for a given set of cuts is the width of the Gaussian fit to the reconstructed mass spectrum. (a) For beam energies between 10 and 40 GeV, the mass resolution is $8.89 \pm 0.13\,\mathrm{MeV/c^2}$. (b) For beam energies between 130 and 160 GeV, the mass resolution is $12.49 \pm 0.29\,\mathrm{MeV/c^2}$.

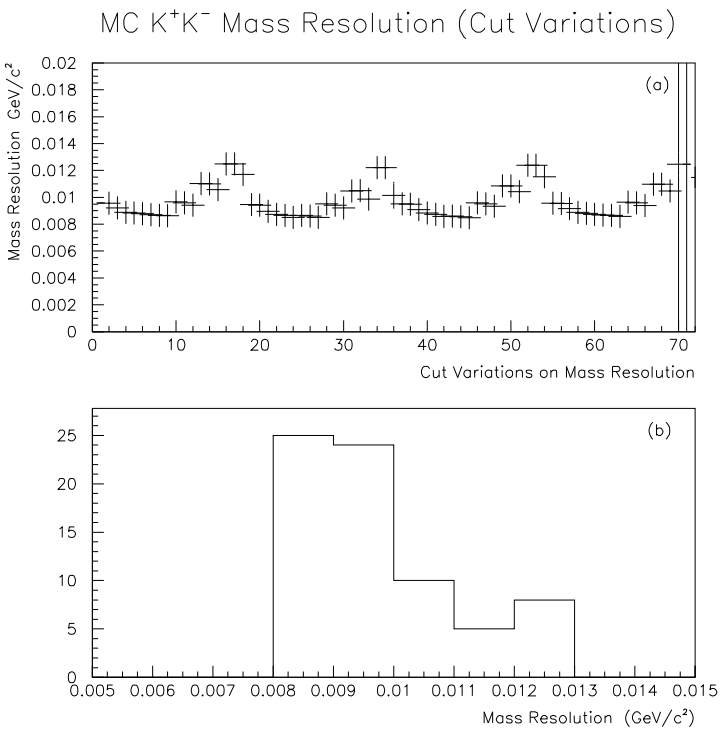

Figure 6.2: Cut variations for the K^+K^- mass resolution. The 72 different cut combinations are listed in the text. (a) The mass resolution as a function of cut combination. (b) A histogram of the mass resolutions for each of the 72 different cut combinations. Based on this study, we conclude that the mass resolution is around 10 MeV/c^2 for K^+K^- events with a mass of 1750 MeV/c^2.

(2) kaonicity greater than 2.0 for both kaons; and (3) kaonicity greater than 2.6 for both kaons. Figure 6.2.b shows a histrogram of the measured mass resolutions for the different cut combinations. Based on this, we can conclude that the mass resolution is consistently around $10\,\mathrm{MeV/c^2}$ for K^+K^- events with a mass of $1750\,\mathrm{MeV/c^2}$.

This mass resolution of around $10\,\mathrm{MeV/c^2}$ agrees well with previous Monte Carlo studies performed on the D^0 mass resolution in the decay $D^0 \to K^+K^-$ [94]. This agreement is expected because of the similar masses of the D^0 meson and the $K^+K^-(1750)$. As will be shown in chapter 7, the width of the $K^+K^-(1750)$ is significantly larger than the mass resolution in this region, so the mass resolution will play a minimal role in the analysis.

Figure 6.3 shows the effects of the same 72 cut combinations listed above on the reconstructed mass (the mean of the Gaussian fit to the reconstructed Monte Carlo mass spectrum). Any systematic shift of the central value of the mass distribution away from $1750\,\mathrm{MeV/c^2}$ would indicate a further systematic error. Figure 6.3.b is a histogram of the reconstructed mass for the different cut combinations. Fitting this histogram with a Gaussian gives a central mass value of $1750.2 \pm 0.5\,\mathrm{MeV/c^2}$ and a width of $0.68 \pm 0.08\,\mathrm{MeV/c^2}$, showing that any systematic deviations from $1750\,\mathrm{MeV/c^2}$ are negligible.

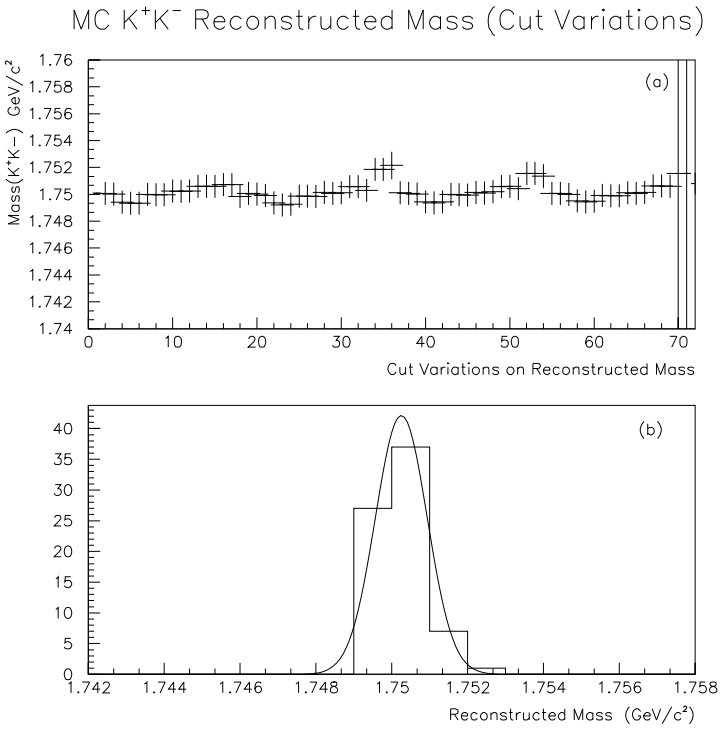

Figure 6.3: Cut variations for the reconstructed K^+K^- mass. The 72 different cut combinations are listed in the text. (a) The mass values as a function of cut combination. (b) A histogram of the mass values for each of the 72 different cut combinations. The histogram has been fit with a Gaussian with a mean of $1750.2 \pm 0.5\,\mathrm{MeV/c^2}$ and width of $0.68 \pm 0.08\,\mathrm{MeV/c^2}$.

6.1.2 The Resolution of t'

The t' distribution in peripheral particle production[2] can typically be fit as an exponential distribution, $ae^{-bt'}$, or two exponentials, $a_1e^{-b_1t'} + a_2e^{-b_2t'}$, in the case of simultaneous production mechanisms. Different production mechanisms can often be distinguished by the exponential slope of their t' distributions. Processes such as diffraction or pion exchange have characteristically shallower slopes than the Primakoff effect (photon exchange), for instance, which is characterized by an extremely steep slope [43]. Thus, especially when dealing with the steep slopes of peripheral production, having a good resolution in measuring t' is crucial if t' distributions are going to be used for distinguishing between production mechanisms.

Since the t' distribution is roughly a measure of how much scattering takes place during resonance production (in fact, for high energy beams $t' \approx p_T^2$), good resolution in t' depends on a good understanding of the beam direction. As explained in chapter 5, an inaccurate determination of the beam direction leads to a t' slope that is underestimated, i.e., too shallow. Section 5.4 provided an estimate for the uncertainty in the beam direction. Using this estimate, a Monte Carlo simulation has been performed to study the effect of this uncertainty in beam direction on the measured t' distribution.

Monte Carlo K^+K^- events were generated at the $\phi(1020)$ mass and at $1750\,\mathrm{MeV/c^2}$ for beam energies flat between 50 and 100 GeV and with a t' distribution of $e^{-1000t'}$. The events were generated with a beam direction varying around the z-axis according to the

[2] See appendix B for a definition of the t' variable.

estimated uncertainty of 0.001 for the x and y direction cosines (see section 5.4). That is, the x and y direction cosines were assumed to be Gaussian with standard deviations of 0.001. The Monte Carlo events were then reconstructed as if the beam direction were constant along the z-direction. The slope of the reconstructed t' distributions is then a measure of the t' resolution.

Figure 6.4 shows generated and reconstructed t' distributions at the $\phi(1020)$ mass for two different ranges of beam energy. For the lower beam energy range ($50 < E_{BEAM} < 75\,\mathrm{GeV}$) the reconstructed slope is $112.3 \pm 2.6\,\mathrm{GeV}^{-2}\mathrm{c}^2$, and for the higher beam energy range ($75 < E_{BEAM} < 100\,\mathrm{GeV}$) it is $61.1 \pm 2.5\,\mathrm{GeV}^{-2}\mathrm{c}^2$. The same pattern holds in the $1750\,\mathrm{MeV/c}^2$ mass region (figure 6.5), where the low beam energy range has a t' slope of $108.4 \pm 1.5\,\mathrm{GeV}^{-2}\mathrm{c}^2$ and the high beam energy range has a slope of $60.6 \pm 1.2\,\mathrm{GeV}^{-2}\mathrm{c}^2$. These reconstructed slopes represent the limits with which the t' slopes of the raw data can be measured.

When this study is compared to trends in the actual data, we find that our measurements of the t' distributions are consistent with the resolution. Figure 6.6 shows the measured t' slope of the $\phi(1020)$ production for different beam energies. The same shallowing of the slope is seen in the data as in the Monte Carlo, from around $85\,\mathrm{GeV}^{-2}\mathrm{c}^2$ for beam energies around 50 GeV to around $70\,\mathrm{GeV}^{-2}\mathrm{c}^2$ for beam energies near 100 GeV. This suggests that the t' measurement of the data is only a measure of our resolution, and the actual slope of the production process is likely steeper. The same trend also holds in the $1750\,\mathrm{MeV/c}^2$ mass region (figure 6.7). Thus, the resolution in t' prohibits

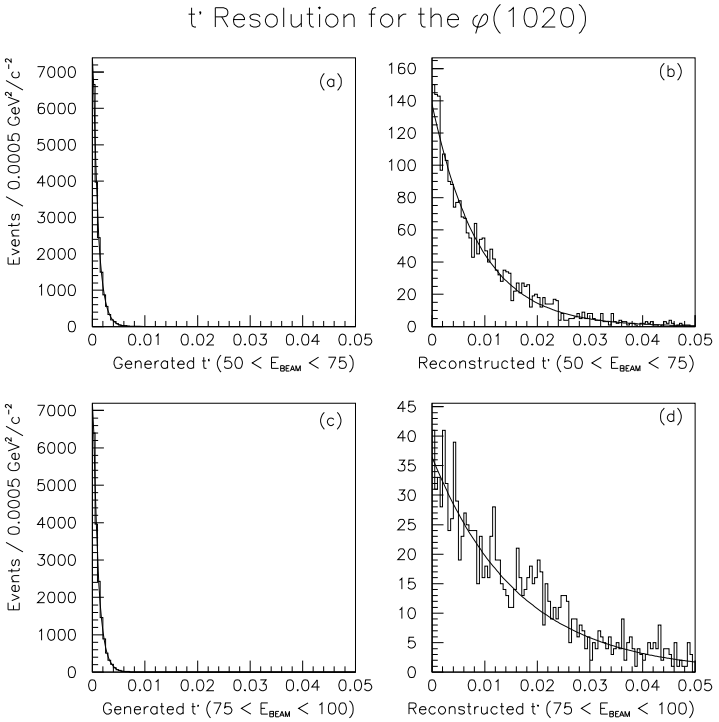

Figure 6.4: The effect of the uncertainty in beam direction on the t' distribution of the $\phi(1020)$. Shown are generated and reconstructed t' distributions for Monte Carlo K^+K^- events in the $\phi(1020)$ mass region for different ranges of beam energy.

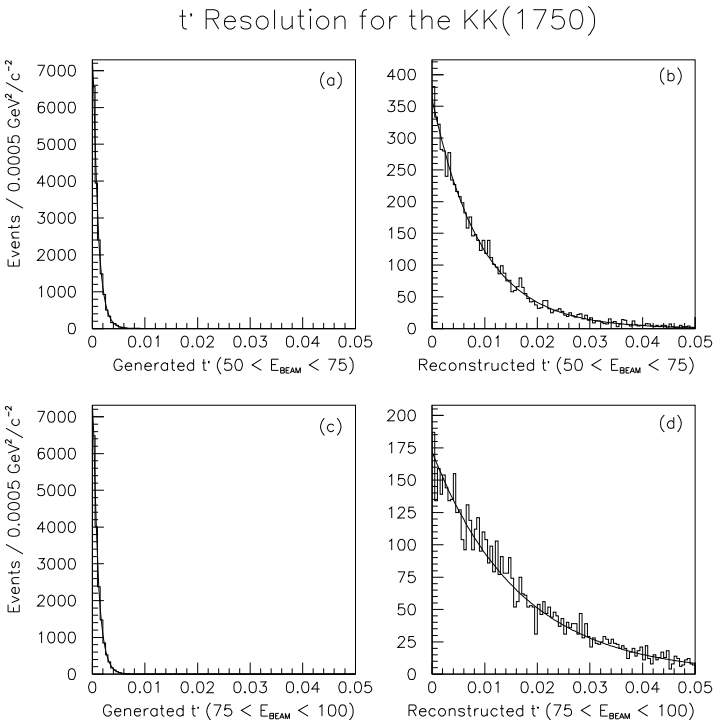

Figure 6.5: The effect of the uncertainty in beam direction on the t' distribution of the $K^+K^-(1750)$. Shown are generated and reconstructed t' distributions for Monte Carlo K^+K^- events in the $K^+K^-(1750)$ mass region for different ranges of beam energy.

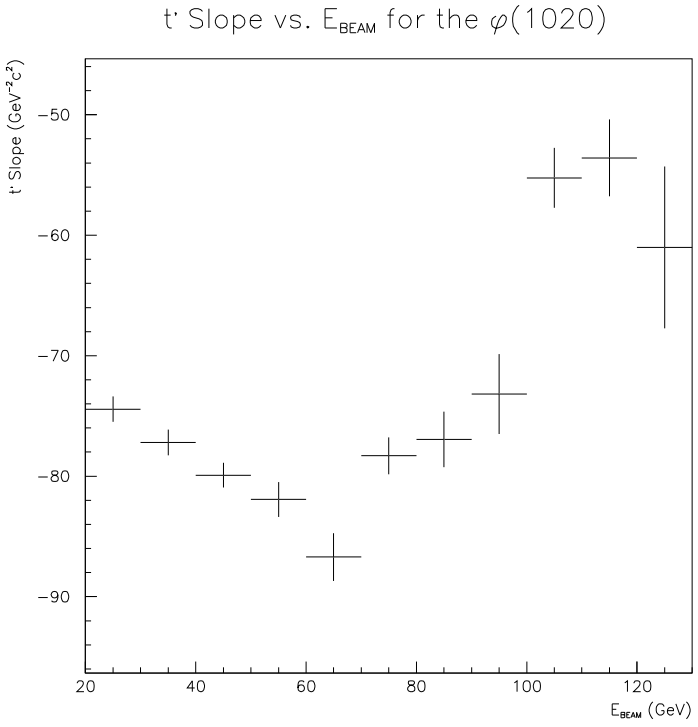

Figure 6.6: The fitted $\phi(1020)$ t' slope as a function of beam energy. The t' distribution is fit with the sum of two exponentials, $a_1 e^{-b_1 t'} + a_2 e^{-b_2 t'}$. The steeper of the two slopes is plotted.

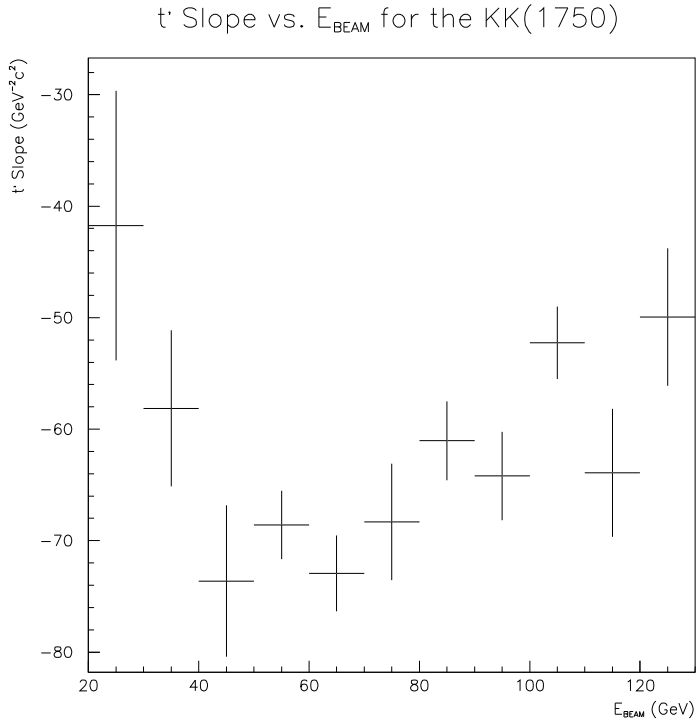

Figure 6.7: The fitted $K^+K^-(1750)$ t' slope as a function of beam energy.

us from distinguishing between the t' slope of diffraction and something that could be steeper, e.g., the Primakoff effect.

6.1.3 Decay Angle Resolution

Besides affecting the slope of the t' distribution, the uncertainty in beam direction also influences the precision with which the decay angles of a resonance can be measured. In the Gottfried-Jackson coordinate system of resonance decays, the z-axis is defined as the beam direction in the resonance rest frame, the x-axis is the cross product of the beam direction and the resonance direction in the overall center of mass, and the y-axis is the cross product of the z and x axes. The uncertainty in beam direction has little effect on the θ (polar) decay angle. Since θ is measured with respect to the beam direction, the uncertainty in θ is on the same order as the uncertainty in the beam direction, i.e., the polar angle has an uncertainty of around 0.001 radians. The ϕ (azimuthal) angle, on the other hand, becomes poorly defined since the x and y directions of the decay coordinate system are defined through the cross product of the beam direction and resonance direction, which are nearly parallel for low-p_T events. The small uncertainty in the beam direction can have a dramatic effect on the outcome of this cross product. Thus, the uncertainty has a tendency to smear angular distributions in ϕ.

This smearing of the angular distribution has been noticed in the raw data. For example, the angular distribution for $\phi(1020)$ events with $p_T > 0.15$ GeV/c shows roughly the correct ϕ dependence (figure 6.8.a). Notice the clear separation between the two peaks in ϕ (compare to figure 9.1). In contrast, the $\phi(1020)$ events with $p_T <$

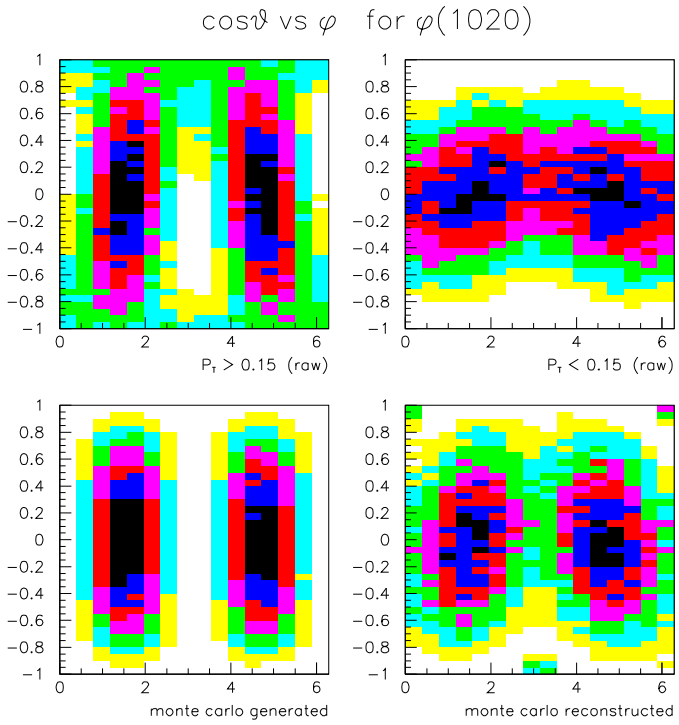

Figure 6.8: Decay angular distributions for the $\phi(1020)$ in the Gottfried-Jackson coordinate system. (a) The (uncorrected) angular distribution for high-p_T $\phi(1020)$ events. (b) The (uncorrected) angular distribution for low-p_T $\phi(1020)$ events. (c) Generated $\phi(1020)$ Monte Carlo events. (d) Reconstructed $\phi(1020)$ Monte Carlo events. The Monte Carlo beam direction was smeared as described in the text. Notice the smearing of the ϕ angle that takes place between figures (a) and (b) and between figures (c) and (d).

0.15 GeV/c appear smeared in ϕ (figure 6.8.b). This is due to the poorly defined production plane in low-p_T events that results from the uncertainty in beam direction.

The same effect can be reproduced in Monte Carlo events. $\phi(1020)$ Monte Carlo events were generated with the proper decay angles (figure 6.8.c) and with a beam direction smeared in the x and y direction cosines according to the 0.001 uncertainty in the beam direction. The same Monte Carlo events were then reconstructed with an unsmeared beam direction. The resulting angular distribution (figure 6.8.d) shows the smearing effect on the ϕ angle. Notice the similarity in the angular distributions of the raw data with $p_T > 0.15\,\mathrm{GeV/c}$ and the generated Monte Carlo on the one hand (figures 6.8.a and 6.8.c), and the raw data with $p_T < 0.15\,\mathrm{GeV/c}$ and the reconstructed Monte Carlo data on the other (figures 6.8.b and 6.8.d).

This severe smearing of the ϕ decay angle poses problems for a detailed angular analysis that have not yet been fully resolved. For all of the angular analyses to be presented in chapter 9, the ϕ decay angle has been averaged over, and emphasis has been placed on the $\cos\theta$ distributions.

6.2 Monte Carlo Studies of Efficiency

The efficiency at some value of a parameter is the percent chance that an event with that value will be properly reconstructed. To say that a K^+K^- event with a K^+K^- mass of $1750\,\mathrm{MeV/c^2}$ has an efficiency of 0.35, for example, is to say that given a K^+K^- event with mass $1750\,\mathrm{MeV/c^2}$ there is a 35% chance that the event will be reconstructed.

Efficiencies are primarily sculpted by three different aspects of the FOCUS detector. First, the vertical slit in H×V causes the most forward events and the events where the decay products are sent through the slit to be missed. Second, the Cerenkov detectors have thresholds that are set in such a way as to give good kaon-pion separation at only certain ranges of kaon momentum (see section 4.4.2). Third, events occasionally can escape the acceptance region of the detector altogether, e.g., a kaon can leave the detector before a minimum number of PWC stations have been hit. These three effects have been studied extensively and show large effects in the efficiency calculations that follow.

6.2.1 General K^+K^- Efficiencies

As explained in the introduction to this chapter, an event of the type $\gamma N \to XN \to K^+K^-N$ can be described by five parameters: E_{BEAM}, M_X, p_T, $\cos\theta_X$, and ϕ_X. For a general study of the mass and width of any resonance, the decay angle efficiencies are inconsequential. This section will describe the general characteristics of the efficiencies of the E_{BEAM}, M_X, and p_T variables for K^+K^- events.

Monte Carlo K^+K^- events have been generated according to $\gamma N \to XN \to K^+K^-N$ with beam energies generated flat between 10 and 160 GeV, p_T flat between 0.0 and 0.3 GeV/c, M_X flat between twice the $K^\pm$ mass and 2.8 GeV/c^2, and decay angles flat in $\cos\theta$ and ϕ. The efficiency distribution for a given variable is then just the reconstructed distribution divided by the generated distribution.

Figure 6.9 shows the K^+K^- mass efficiencies for different ranges of beam energy.

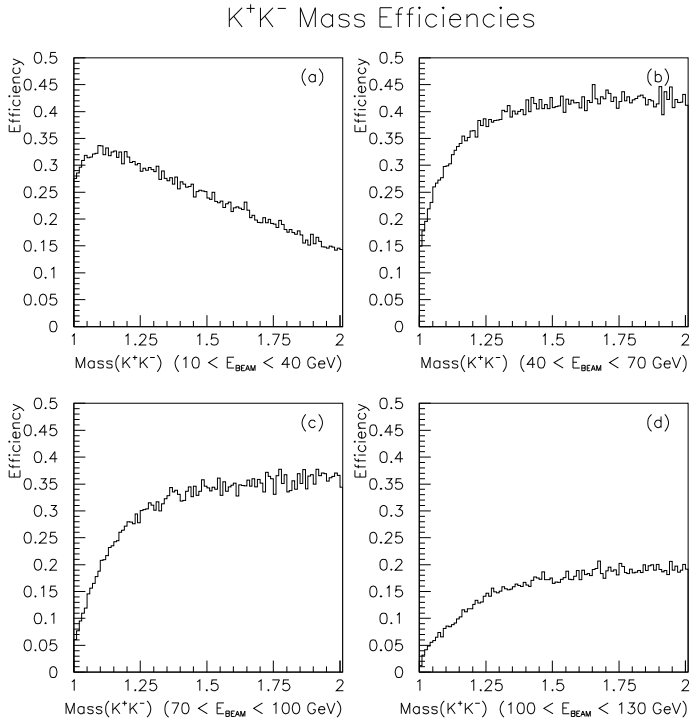

Figure 6.9: The efficiency as a function of mass for K^+K^- events in different beam energy bins. (a) $10 < E_{BEAM} < 40$ GeV; (b) $40 < E_{BEAM} < 70$ GeV; (c) $70 < E_{BEAM} < 100$ GeV; and (d) $100 < E_{BEAM} < 130$ GeV.

The distributions are well-behaved above 1500 MeV/c^2 and show a drop in efficiency around the $\phi(1020)$ mass. The drop at low masses is due to the higher momenta of the K^+K^- final state when less energy is used up in the creation of the resonance. The higher resonance momentum makes the decay products (K^+K^-) more likely to pass through the slit in H$\times$V.

Figure 6.10 shows the beam energy efficiency of K^+K^- events with different ranges of K^+K^- invariant mass. The distributions are relatively similar in the $K^+K^-(1750)$ region and its sidebands, but the beam energy efficiency peaks at a lower beam energy in the $\phi(1020)$ region. Again, this is due to the slit in H$\times$V. The efficiency drops to zero at larger beam energies due to the Cerenkov counter thresholds. Higher beam energy means higher kaon momenta, and when the kaon momenta pass a threshold the kaons become indistinguishable from pions and events are rejected.

Compared to the more dramatic variation in efficiencies in the mass and beam energy, the p_T efficiencies are flat and smooth. Figure 6.11 shows that for all beam energies and all K^+K^- masses the p_T efficiency is flat from 0.0 to at least 0.3 GeV/c.

6.2.2 Comparing K^+K^- and K^*K Efficiencies

In order to calculate the relative branching ratio of $K^+K^-(1750) \to K^*K$ relative to $K^+K^-(1750) \to K^+K^-$ the relative efficiencies of the K^+K^- and $K_SK^\pm\pi^\mp$ final states must be understood. Since the spin of the $K^+K^-(1750)$ has not yet been conclusively determined, several different angular distributions of the $K^+K^-(1750)$ decay have been simulated. In order to set the most conservative upper limit on $\Gamma(K^+K^-(1750) \to$

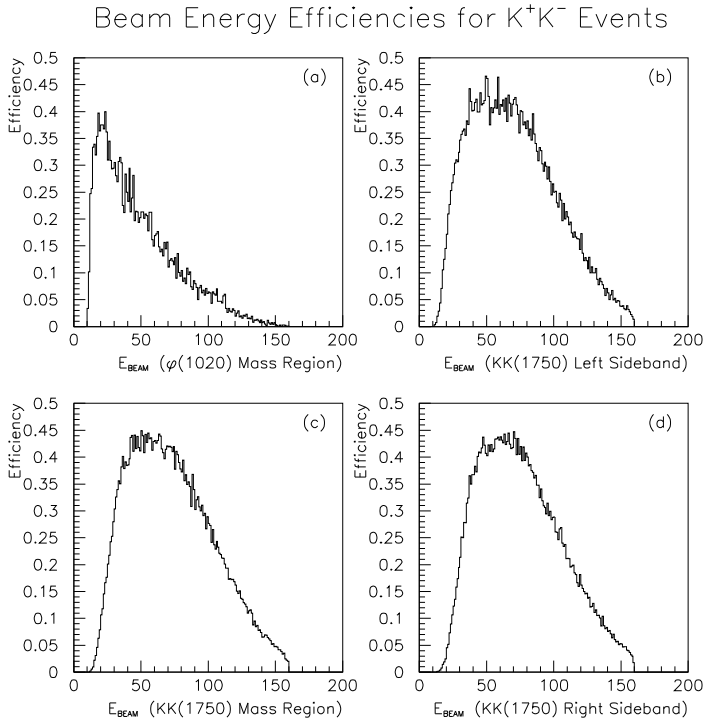

Figure 6.10: The efficiency as a function of beam energy for K^+K^- events in different bins of mass. (a) The $\phi(1020)$ region; (b) the $K^+K^-(1750)$ left sideband; (c) the $K^+K^-(1750)$ signal region; and (d) the $K^+K^-(1750)$ right sideband.

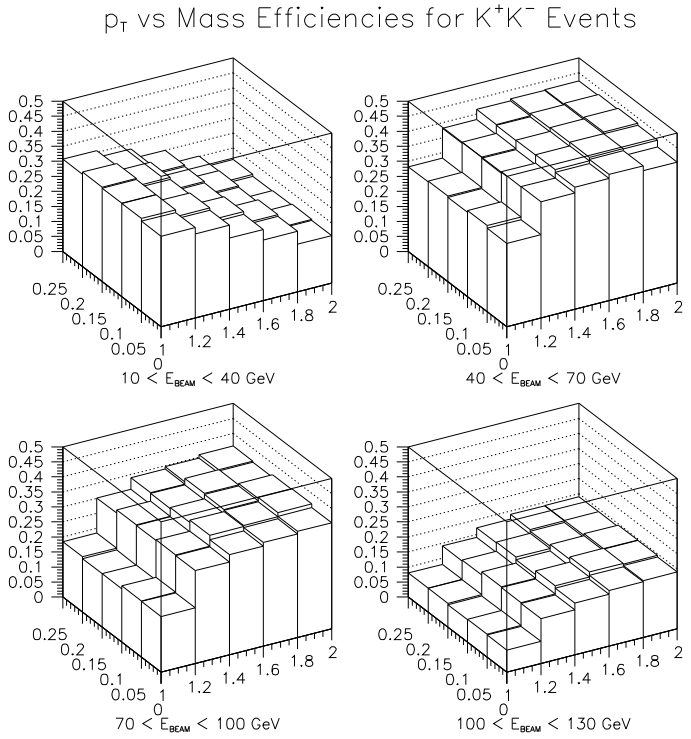

Figure 6.11: The efficiency as a function of mass and transverse momentum (p_T) for K^+K^- events in different beam energy bins. (a) $10 < E_{BEAM} < 40$ GeV; (b) $40 < E_{BEAM} < 70$ GeV; (c) $70 < E_{BEAM} < 100$ GeV; and (d) $100 < E_{BEAM} < 130$ GeV. The p_T efficiency is flat in all mass and beam energy bins.

$K^*K)/\Gamma(K^+K^-(1750) \rightarrow K^+K^-)$, the decay distribution with the largest efficiency was used for $K^+K^-(1750) \rightarrow K^+K^-$ and the smallest was used for $K^+K^-(1750) \rightarrow K^*K$.

The K^+K^- efficiencies were determined by generating 8 million Monte Carlo K^+K^- events with $\cos^2\theta$, $\sin^2\theta$, and flat distributions in the θ decay angle. The beam energy was generated flat between 10 and 160 GeV, the mass was flat from twice the $K^\pm$ mass to 2.8 $\mathrm{GeV/c^2}$, and p_T was flat between 0.0 and 0.3 GeV/c.

Two different K^*K distributions were generated corresponding to the two different K^* combinations possible in the $K_S K^\pm \pi^\mp$ final state. The initial K^*K was generated with the K^*K decaying according to $\cos^2\theta$, $\sin^2\theta$, or flat distributions in the θ decay angle, as in the K^+K^- final state. The K^* was then allowed to decay according to the same variety of distributions. The kinematic regions were the same as in the K^+K^- case.

Figure 6.12 compares the mass efficiencies for the $K^{*0}K_S$, $K^{*\pm}K^\mp$, and K^+K^- decay modes. The efficiency of the K^+K^- mode is nearly a factor of five higher than either of the K^*K modes. Since we have seen that the K^+K^- efficiency in beam energy varies dramatically from beam energy to beam energy (figure 6.10), it becomes important to also understand the way the K^*K efficiency depends on beam energy. Figure 6.13 shows the beam energy efficiency for the two different K^*K modes. It can be seen that the two modes are rather consistent with each other, but the efficiency peaks at higher beam energy than the K^+K^- case. This is entirely due to the Cerenkov

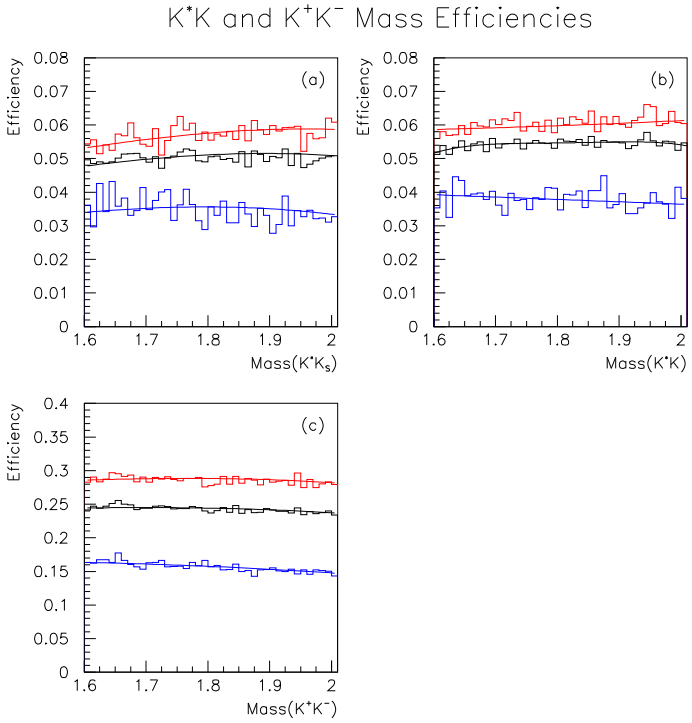

Figure 6.12: The K^+K^- and $K_SK^\pm\pi^\mp$ efficiencies as a function of mass for different angular distributions. (a) $K^{*0}K_S$ events, (b) $K^{*\pm}K^\mp$ events, and (c) K^+K^- events. Red is for $\sin^2\theta$ decay distributions; blue is for $\cos^2\theta$ decay distributions; and black is for isotropic decays. Beam energies from 10 to 160 GeV are included.

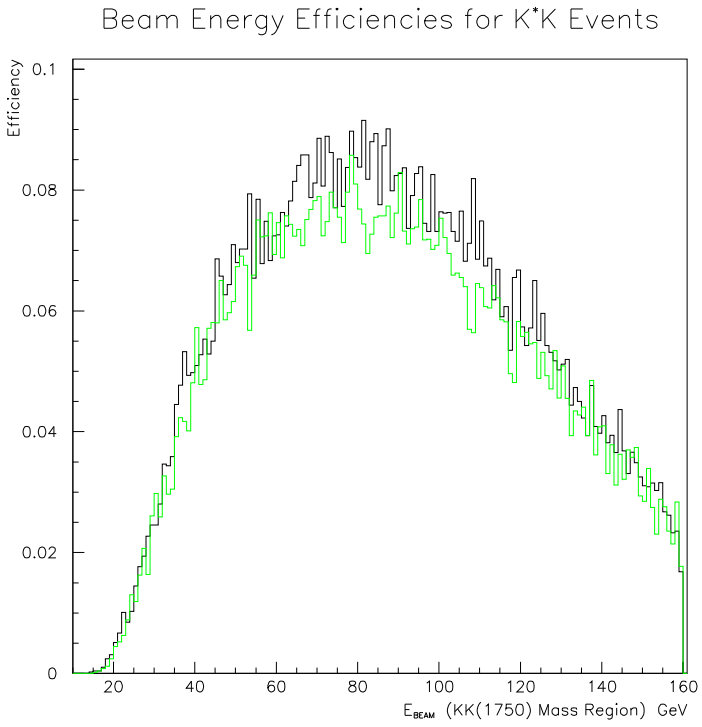

Figure 6.13: The efficiency as a function of beam energy for K^*K events in the $K^+K^-(1750)$ mass region. The black is for $K^{*\pm}K^{\mp}$ and the green is for $K^{*0}K_S$.

requirements. The kaons in the K^+K^- final state have higher momenta than that in the $K_S K^{\pm}\pi^{\mp}$ final state.

When calculating relative efficiencies between the K^+K^- mode and the two K^*K modes, the efficiencies have been averaged over beam energies in order to take out the effect of the differences in beam energy efficiencies. This will be described in more detail in section 7.4.

6.2.3 Event by Event Acceptance Corrections

Parts of the limited angular analyses of chapter 9 as well as the comparisons between $\phi(1020)$ and $K^+K^-(1750)$ production in chapter 8 will require acceptance weighting on an event by event basis. To calculate the weights a matrix was formed with the following divisions: 25 divisions in K^+K^- mass between 1.0 and 2.0GeV/c^2; 5 divisions in E_{BEAM} between 50 and 100 GeV; 40 divisions in $\cos\theta$; and 16 divisions in ϕ. Approximately 10,000 events were generated in each bin.

There is a large variation in the shapes of the $\cos\theta$ efficiencies. Figure 6.14 shows the $\cos\theta$ efficiencies for different mass and beam energy regions. The sculpted shapes are due to the Cerenkov thresholds and the slit in H$\times$V.

Because of the variation in beam energy efficiency, even in the limited region of 50 to 100 GeV (figure 6.10), and the variation in $\cos\theta$ efficiency, a two dimensional interpolation was done between bins of beam energy and $\cos\theta$ to calculate the weight for a given event. The ϕ distributions are averaged over, and are relatively unimportant anyway due to the large smearing phenomenon explained earlier.

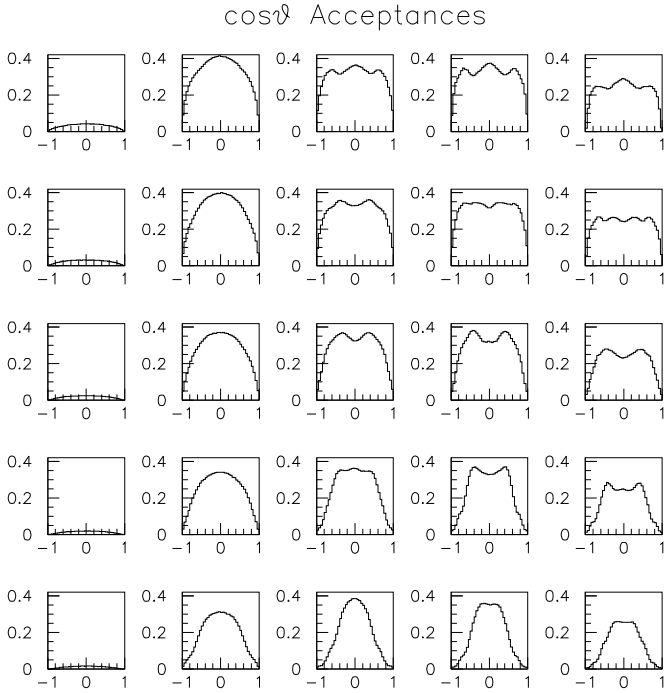

Figure 6.14: K^+K^- efficiencies as a function of $\cos\theta$. The five columns are for different mass regions: (1) the $\phi(1020)$ mass region; (2) the $\phi(1020)$ right sideband; (3) the $K^+K^-(1750)$ left sideband; (4) the $K^+K^-(1750)$ signal region; and (5) the $K^+K^-(1750)$ right sideband. The five rows are for different beam energy requirements: (1) $50 < E_{BEAM} < 60\,\mathrm{GeV}$; (2) $60 < E_{BEAM} < 70\,\mathrm{GeV}$; (3) $70 < E_{BEAM} < 80\,\mathrm{GeV}$; (4) $80 < E_{BEAM} < 90\,\mathrm{GeV}$; and (5) $90 < E_{BEAM} < 100\,\mathrm{GeV}$.

6.2.4 Note on the $K_S K_S$ Efficiency

Observing a signal corresponding to the $K^+K^-(1750)$ in the $K_S K_S$ final state would be a powerful way of limiting the possible quantum numbers of the $K^+K^-(1750)$, since only states with J^{PC} of 0^{++}, 2^{++}, etc. can decay to $K_S K_S$. Unfortunately, the efficiency in $K_S K_S$ has been found to be too small to be sensitive to any such signal, primarily because of the trigger requirement that there be a coincidence in TR1 and TR2 (see section 4.4.3), but also because four tracks (a $\pi^+\pi^-$ pair for each K_S) must be detected rather than just two. Since K_S travel some distance before they decay to $\pi^+\pi^-$, many K_S decay beyond the TR1 triggering element, which was placed immediately after the last target element, and these events are never triggered. This has proved fatal for any analysis of the exclusive $K_S K_S$ final state.

Chapter 7

Observation of the $K^+K^-(1750)$

Using the FOCUS spectrometer with photon beam energies between 20 and 160 GeV, we confirm the existence of a low-p_T photoproduced enhancement in K^+K^- at a mass of 1750 MeV/c^2 with nearly 100 times the statistics of previous experiments[1]. Assuming this enhancement to be a single resonance with a Breit-Wigner mass shape, we determine its mass to be $1753.5 \pm 1.5 \pm 2.3$ MeV/c^2 and its width to be $122.2 \pm 6.2 \pm 8.0$ MeV/c^2. We find no corresponding enhancement at 1750 MeV/c^2 in K^*K, and again neglecting any possible interference effects we place limits on the ratio $\Gamma(K^+K^-(1750) \to K^*K)/\Gamma(K^+K^-(1750) \to K^+K^-)$. Our results are consistent with previous photoproduction experiments, but, because of the much greater statistics, challenge the common interpretation of this enhancement as the $\phi(1680)$ seen in e^+e^- annihilation experiments.

[1] The initial observation of this state by the FOCUS collaboration has been published in [95].

7.1 Motivation

Previous photoproduction experiments [79, 84, 58] have consistently observed an enhancement in K^+K^- at a mass near $1750\,\mathrm{MeV/c^2}$, which we refer to as the "$K^+K^-(1750)$." However, with signals consisting of only around 100 events and with a statistical significance of the enhancement of, at best, only $3.5\,\sigma$ over background, these experiments have suffered from a lack of statistics. Due to the large statistical errors on the mass of the enhancement, and assuming that the $K^+K^-(1750)$ is a diffractively photoproduced meson with $J^{PC} = 1^{--}$, this enhancement has been identified with the $\phi(1680)$ seen in e^+e^- annihilation [75, 68, 85, 81], which is a candidate radial excitation of the $\phi(1020)$. The present analysis challenges this interpretation of the $1750\,\mathrm{MeV/c^2}$ signal on two grounds.

First, assuming the enhancement is a single resonance, we determine its mass to be $1753.5 \pm 1.5 \pm 2.3\,\mathrm{MeV/c^2}$ from our sample of more than 10,000 signal events, which is clearly inconsistent with $1680\,\mathrm{MeV/c^2}$. One previous photoproduction experiment [79], using less than 50 signal events and guided by e^+e^- annihilation results, presented a mass of $1690 \pm 10\,\mathrm{MeV/c^2}$ after an analysis based on a model including interference and Deck-like effects. With orders of magnitude more statistics, we are unable to reproduce this result.

Second, although e^+e^- annihilation experiments report the dominant decay mode of the $\phi(1680)$ to be K^*K [81], as expected theoretically for the radial excitation of the $\phi(1020)$ [14, 96, 97], we find no evidence for a photoproduced enhancement in K^*K

corresponding to the photoproduced enhancement in K^+K^-. We put a tight upper limit on the ratio $\Gamma(K^+K^-(1750) \to K^*K)/\Gamma(K^+K^-(1750) \to K^+K^-)$.

7.2 Data Sample

The K^+K^- and $K_SK^\pm\pi^\mp$ data samples used in this analysis require a single vertex in the target, no electromagnetic energy apart from that associated with the reconstructed tracks, and require all tracks to be singly linked between the upstream and downstream tracking systems. Events with additional reconstructed tracks are rejected, making the data samples as exclusive as possible[2]. The Cerenkov identification of the kaons in both diffractive final states limits the photon energy range to $\leq 160\,\mathrm{GeV}$.

7.3 Mass and Width Measurement

7.3.1 Observation

Our sample of K^+K^- events, selected using the criteria described above, shows a large $\phi(1020)$ signal dominating the spectrum (figure 7.1). The diffractive component of the production of the $\phi(1020)$ shows up as a peak in the p_T spectrum (figure 7.2.a). Cutting around this peak by requiring $p_T < 0.15\,\mathrm{GeV/c}$, we select a low-$p_T$ sample of K^+K^- events[3], in which a clear enhancement appears in the mass spectrum near $1750\,\mathrm{MeV/c^2}$

[2]Further exclusivity could be guaranteed by requiring the missing mass of the final state to equal the mass of the scattered nucleon, but the beam energy resolution of the FOCUS detector is inadequate (see chapter 5).

[3]Since $t' \approx p_T^2$ for the high energies of the FOCUS beam, the cut $p_T < 0.15\,\mathrm{GeV/c}$ corresponds to a cut in t', $t' < 0.0225\,\mathrm{GeV^2/c^2}$.

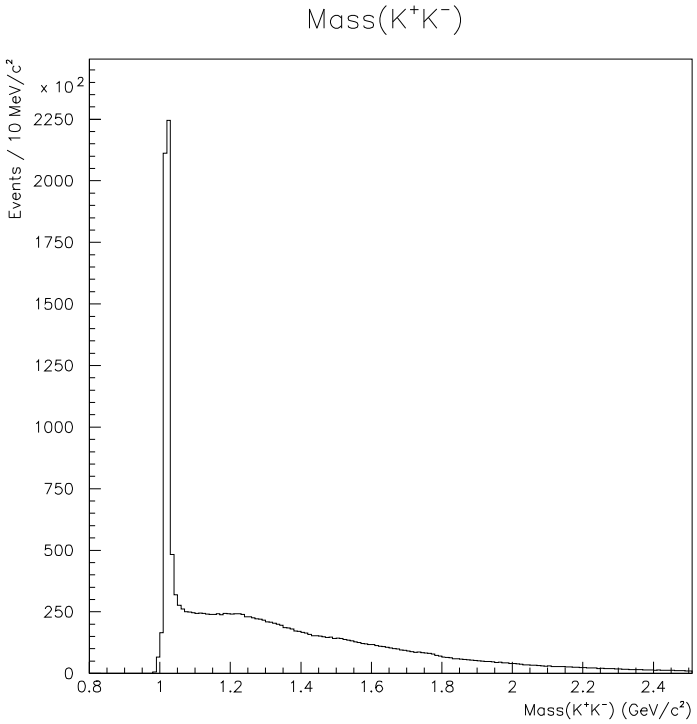

Figure 7.1: The FOCUS K^+K^- mass spectrum with no cut on p_T. The narrow peak is the $\phi(1020)$ signal.

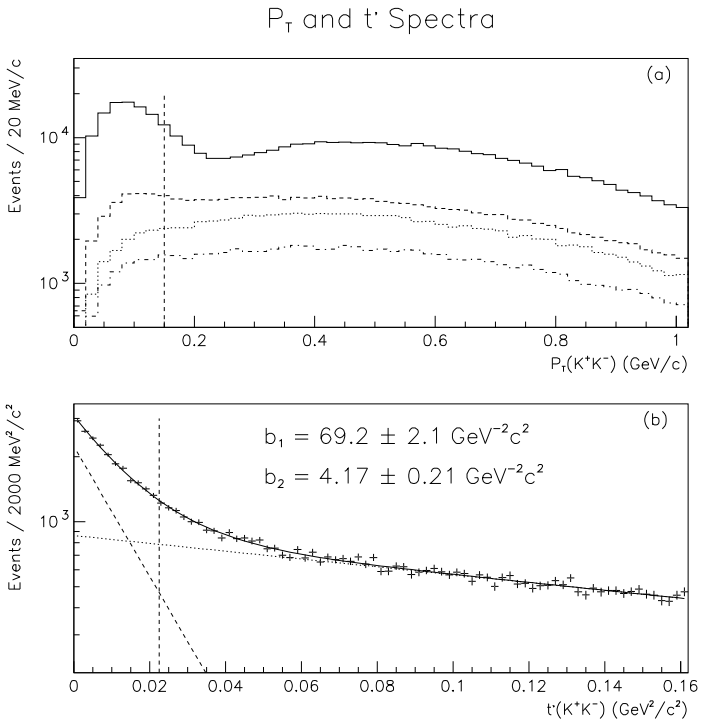

Figure 7.2: The K^+K^- p_T and t' spectra for various mass regions. (a) The K^+K^- p_T spectra. The solid line is the p_T spectrum for the $\phi(1020)$. The top dotted line is the p_T spectrum for K^+K^- masses between 1640 and 1860 $\mathrm{MeV/c^2}$; the middle is for the left sideband (1500–1600 $\mathrm{MeV/c^2}$); and the bottom is for the right sideband (1900–2100 $\mathrm{MeV/c^2}$). (b) The t' spectrum for K^+K^- masses between 1640 and 1860 $\mathrm{MeV/c^2}$ fit using two exponentials, $a_1 e^{-b_1 t'} + a_2 e^{-b_2 t'}$. In each plot, the vertical line represents the p_T cut used in this analysis.

(figure 7.3). This enhancement is what we refer to as the $K^+K^-(1750)$.

The dashed line of figure 7.4.b, showing events with $p_T > 0.15\,\mathrm{GeV/c}$, and with no evidence of any enhancement at $1750\,\mathrm{MeV/c^2}$, confirms that the enhancement appears only at low p_T. Figure 7.2.a shows the p_T spectra in the 1750 region (1640–1860 $\mathrm{MeV/c^2}$) and in the two sideband regions (1500–1600 $\mathrm{MeV/c^2}$ and 1900–2100 $\mathrm{MeV/c^2}$); it is seen that the 1750 region has a peak in the p_T spectrum in nearly the same place as the $\phi(1020)$ peak, but the sideband regions have significantly smaller p_T peaks, indicating that the background under the $K^+K^-(1750)$ signal is largely non-diffractive.

The t' spectrum[4] for K^+K^- masses between 1640 and 1860 $\mathrm{MeV/c^2}$ has been fit with two exponentials (figure 7.2.b). The steeper of the two exponentials for this region has a slope of $69.2 \pm 2.1\,\mathrm{GeV^{-2}c^2}$ and the background exponential has a slope of $4.17 \pm 0.21\ \mathrm{GeV^{-2}c^2}$. For comparison, the $\phi(1020)$ signal has a diffractive slope of $77.71 \pm 0.59\ \mathrm{GeV^{-2}c^2}$ and a background slope of $1.71 \pm 0.14\ \mathrm{GeV^{-2}c^2}$. While steep slopes are characteristic of exclusive diffractive photoproduction off of nuclear targets, these slopes cannot be taken as evidence that the $K^+K^-(1750)$ is being produced diffractively. Chapter 8 will discuss this point in much greater detail.

Fitting the $1750\,\mathrm{MeV/c^2}$ mass region with a non-relativistic Breit-Wigner distribution and a quadratic polynomial background, we find

$$\text{Yield} = 11{,}700 \pm 480 \text{ Events}$$

[4] $t' \equiv |t| - |t|_{min} \approx p_T^2$ and $t \equiv (P_{BEAM} - P_{KK})^2$, where P_{BEAM} and P_{KK} are the four-momenta of the photon beam and the K^+K^- system, respectively.

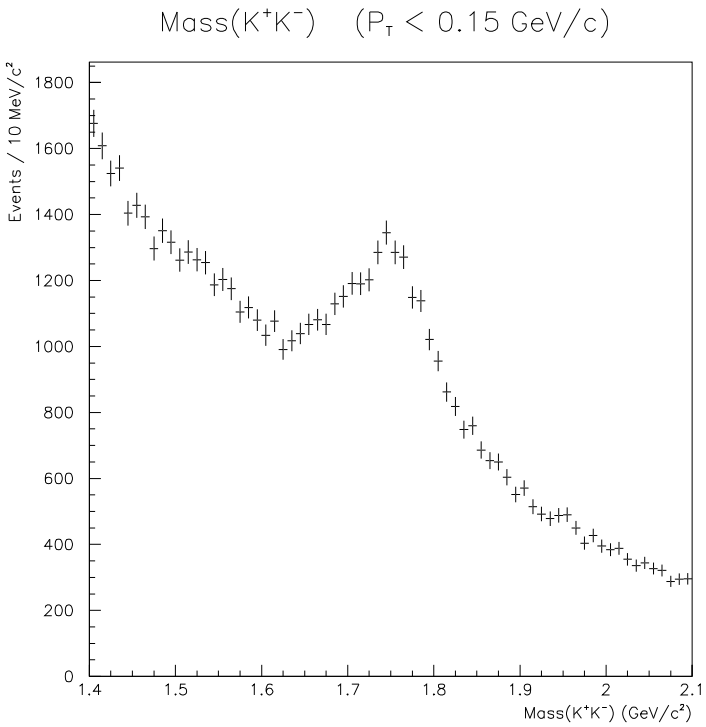

Figure 7.3: The K^+K^- mass spectrum with the requirement that $p_T < 0.15\,\mathrm{GeV/c}$. The large enhancement is the $K^+K^-(1750)$ signal.

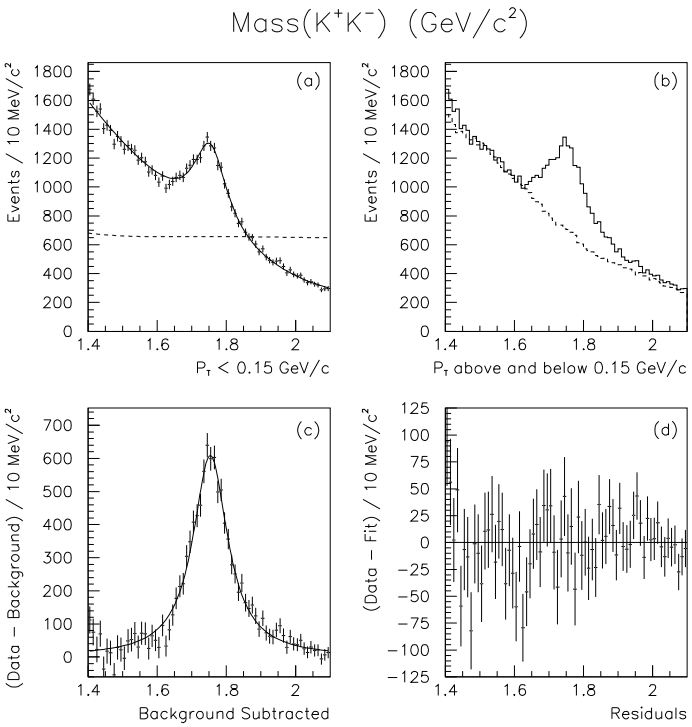

Figure 7.4: The $K^+K^-(1750)$ mass fit. (a) The K^+K^- mass spectrum with the requirement that $p_T < 0.15\,\mathrm{GeV/c}$. The spectrum is fit with a non-relativistic Breit-Wigner distribution and a quadratic background. The dotted line is the Monte Carlo efficiency on a scale from 0 to 100%. (b) The $K^+K^-(1750)$ is produced only at low-p_T: the solid line is the K^+K^- mass spectrum with the requirement that $p_T < 0.15\,\mathrm{GeV/c}$, and the dotted line is the K^+K^- mass spectrum with $p_T > 0.15\,\mathrm{GeV/c}$ scaled to the size of the low-p_T spectrum for comparison. (c) The data and fit after subtracting the quadratic polynomial background shape. (d) The residuals, i.e., the data minus the fit.

$$M = 1753.5 \pm 1.5 \pm 2.3\,\mathrm{MeV/c^2}$$

$$\Gamma = 122.2 \pm 6.2 \pm 8.0\,\mathrm{MeV/c^2}.$$

Because the acceptance of the detector is flat in this region, as determined by a full Monte Carlo simulation, the fit was performed on the uncorrected mass spectrum. Further, since Monte Carlo studies of the detector have shown that the K^+K^- mass resolution in the $1750\,\mathrm{MeV/c^2}$ region is around $10\,\mathrm{MeV/c^2}$ (see section 6.1.1), which is much less than the width of the $K^+K^-(1750)$, resolution effects have been neglected in the fit.

7.3.2 Mass and Width Systematic Errors

The systematic errors were determined by varying the p_T cut, the Cerenkov cuts, the form of the Breit-Wigner shape (non-relativistic, and relativistic L = 0,1,2), and the form of the background shape, and include the systematic uncertainty in the FOCUS mass scale ($1.2\,\mathrm{MeV/c^2}$ [94]). Figure 7.5 shows fits with different Breit-Wigner forms: non-relativistic, relativistic L = 0, relativistic L = 1, and relativistic L = 2. The Breit-Wigner form has little impact on the mass and width values.

Figure 7.6 shows the effects of 144 different cut combinations on the mass. The systematic error on the mass is taken to be the width of the Gaussian in figure 7.6.b, $2.0\,\mathrm{MeV/c^2}$, added in quadrature to the mass scale uncertainty, $1.2\,\mathrm{MeV/c^2}$, to give a total systematic error of $2.3\,\mathrm{MeV/c^2}$. Figure 7.7 shows the effects of the same 144 cut combinations on the $K^+K^-(1750)$ width. The width of the Gaussian in figure 7.7.b

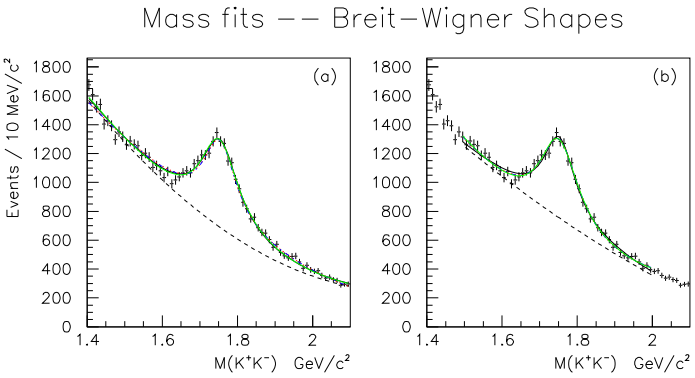

Figure 7.5: A comparison of four different Breit-Wigner forms: non-relativistic (black); relativistic L = 0 (red); relativistic L = 1 (blue); and relativistic L = 2 (green). There is very little difference between the four fits. (a) The mass spectrum is fit between K^+K^- masses of 1400 and 2100 MeV/c^2. (b) The mass spectrum is fit between 1500 and 2000 MeV/c^2.

leads to the systematic error on the width of the $K^+K^-(1750)$, 8.0 MeV/c^2.

The 144 different cut combinations correspond to the following variations. Cuts 1–36: non-relativistic Breit-Wigner; cuts 37–72: relativistic L = 0 Breit-Wigner; cuts 73–108: relativistic L = 1 Breit-Wigner; and cuts 109–144: relativistic L = 2 Breit-Wigner. Within each of these there are two fit ranges: (1) mass fit between 1400 and 2100 MeV/c^2; and (2) mass fit between 1500 and 2000 MeV/c^2. Within these there are two background shapes: (1) 2nd degree polynomial; and (2) 3rd degree polynomial. Within these there are three sets of p_T cuts: (1) $p_T < 0.10$ GeV/c; (2) $p_T < 0.15$ GeV/c; and (3) $p_T < 0.20$ GeV/c. Within these there are three sets of Cerenkov cuts: (1) kaonicity greater than 1.4 for both kaons; (2) kaonicity greater than 2.6 for both kaons;

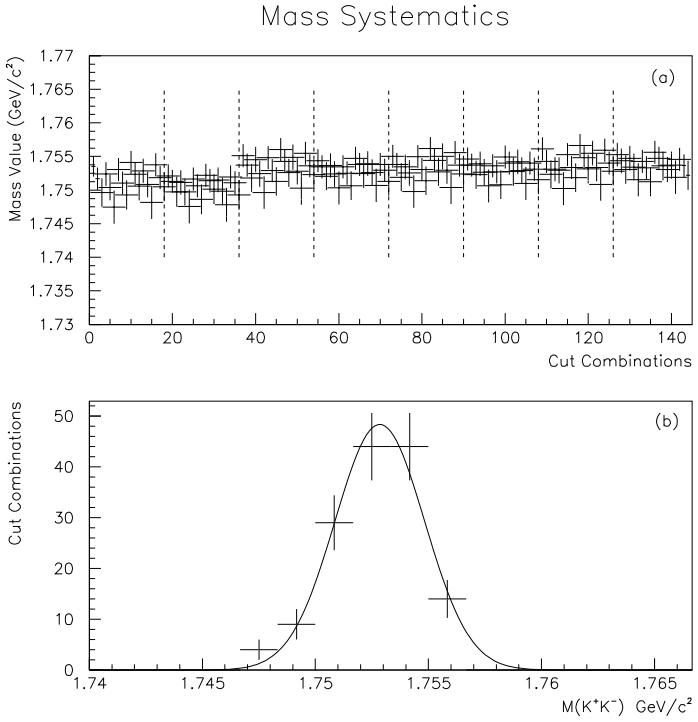

Figure 7.6: The systematic error on the $K^+K^-(1750)$ mass. (a) The measured mass value as a function of cut combination. The 144 different cut combinations are described in the text. (b) A histogram of the measured mass values for the 144 different cut combinations. The width of the Gaussian fit, 2.0 MeV/c^2, combined with the systematic uncertainty in the mass scale, 1.2 MeV/c^2, gives the total systematic error on the $K^+K^-(1750)$ mass, 2.3 MeV/c^2.

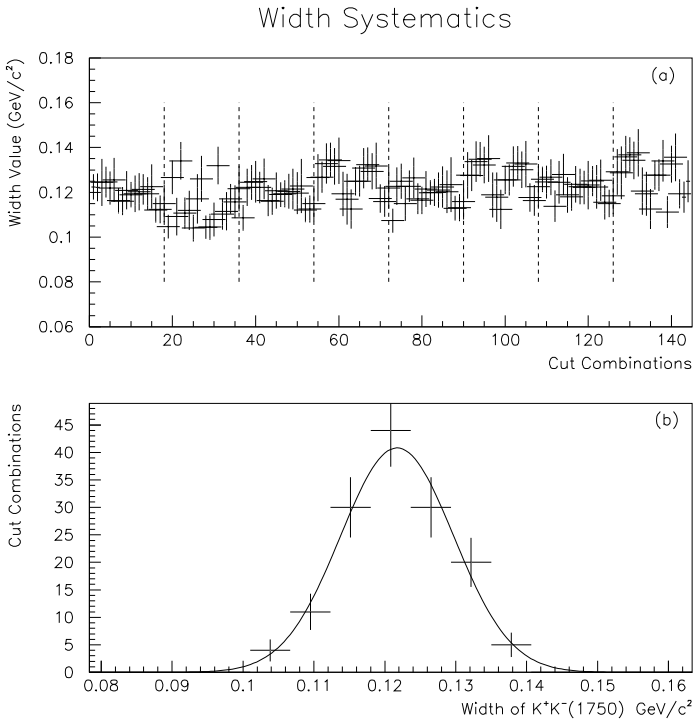

Figure 7.7: The systematic error on the $K^+K^-(1750)$ width. (a) The measured width value as a function of cut combination. The width was measured for the same 144 cut combinations as were used to measure the mass. (b) A histogram of the measured width values for the 144 different cut combinations. The width of the Gaussian fit, $8.0\,\mathrm{MeV/c^2}$, is taken to be the systematic error on the $K^+K^-(1750)$ width.

and (3) kaonicity greater than 6.0 for both kaons.

7.3.3 Interference Scenarios

There is a region near 1600 MeV/c^2 where there is some discrepancy in our fit to the K^+K^- mass spectrum. The residuals show that the statistical significance of this discrepancy is not strong (figure 7.4.d). It has been found that several different interference scenarios can improve the fit. These include interference with the K^+K^- continuum and interference between the $K^+K^-(1750)$ and a second resonance with lower mass. The goodness of the fits, however, does not allow us to discriminate between solutions, and we find no physics motivation for picking one solution over another. In all scenarios, the mass of the $K^+K^-(1750)$ exceeds 1747 MeV/c^2. For this reason, our mass and width measurements and our determination of systematic errors assume the production of a single, non-interfering resonance.

Figure 7.8 shows 4 distinct solutions (all with good χ^2/dof) that allow the Breit-Wigner to interfere with the second degree polynomial background. The fraction of the Breit-Wigner amplitude allowed to interfere with the background is varied in each.

Figure 7.9 considers the possibility that there is a second resonance interfering with the $K^+K^-(1750)$. The nine plots represent nine different initial values for the fit. All the results have good χ^2/dof, but the properties of the second Breit-Wigner vary wildly, from a 10 MeV/c^2 wide resonance to one 400 MeV/c^2 wide.

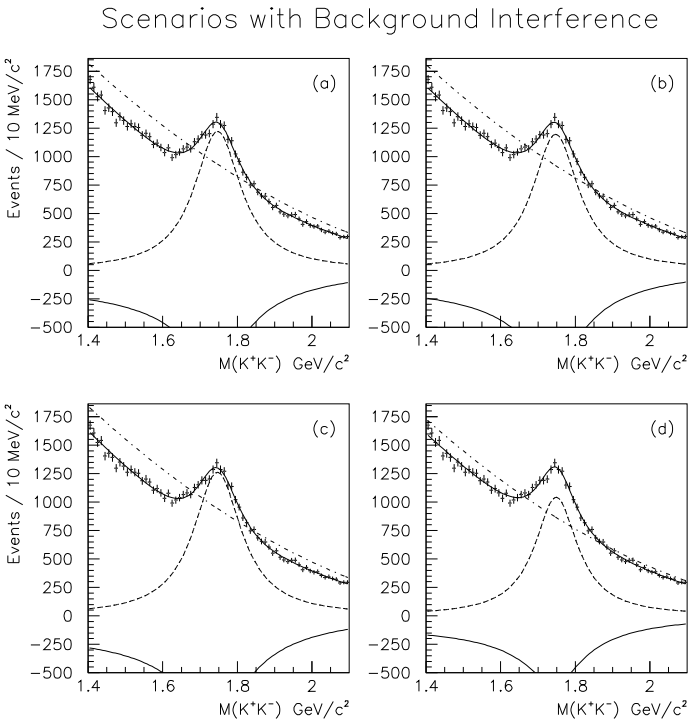

Figure 7.8: Scenarios where the $K^+K^-(1750)$ is allowed to interfere with the background. The Breit-Wigner interferes with the second degree polynomial background. (a) Interference of the Breit-Wigner with 100% of the background. (b) The amount of background interfering with the Breit-Wigner is allowed to vary. The solution has $\approx 50\%$ of the background interfering with the Breit-Wigner. (c) The amplitude of the interfering polynomial is limited to 25%. (d) The amplitude of the interfering polynomial is limited to 10%. The dashed lines are the Breit-Wigner and the polynomial background; the solid line below the data is the interference term; and the solid line passing through the data is the sum of all three terms. The $K^+K^-(1750)$ mass value never drops below $1747\,\mathrm{MeV/c^2}$.

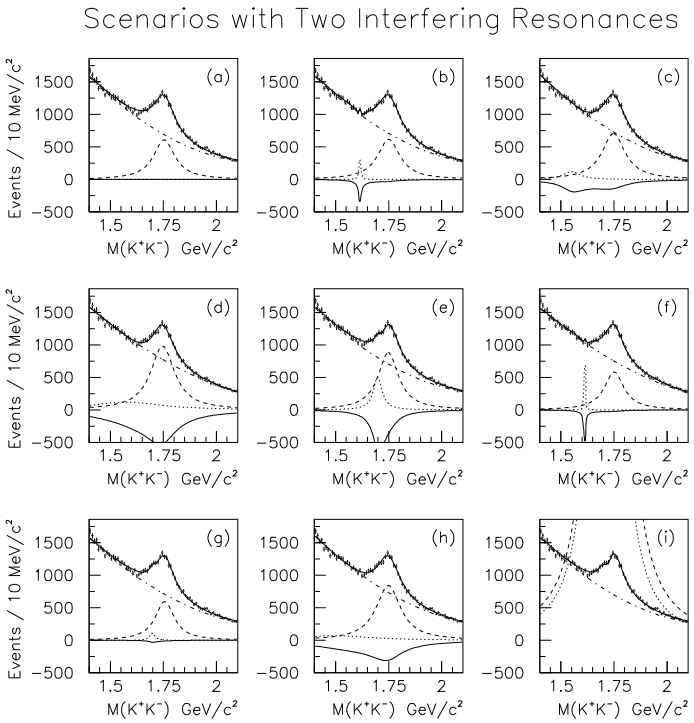

Figure 7.9: Interference scenarios involving two interfering Breit-Wigners. The fit is highly unstable. The nine different plots correspond to nine different initial values for the mass and width of the interfering Breit-Wigner. The dotted lines are the two Breit-Wigners and the polynomial background; the solid line below the data is the interference term; and the solid line passing through the data is the sum of all four terms. Again, the $K^+K^-(1750)$ mass value never drops below $1747\,\mathrm{MeV/c^2}$, except in figure (i), which is clearly unphysical.

7.4 Branching Ratio

In order to study the K^*K/K^+K^- branching ratios of the $K^+K^-(1750)$, we start with a sample of $K_SK^\pm\pi^\mp$ events. Figure 7.10 shows the mass spectrum of our $K_SK^\pm\pi^\mp$ sample and the two K^* combinations. Before imposing a cut on p_T, the $K_SK^\pm\pi^\mp$ mass spectrum shows the classic "D" and "E" regions [13].

After requiring $p_T < 0.15\,\mathrm{GeV/c}$ (the same p_T cut imposed on the K^+K^- sample), and requiring a K^*, two distinct K^*K spectra were fit individually (figure 7.11). The first corresponds to $K^{*0}K_S$ with K^{*0} decaying to $K^\pm\pi^\mp$; the second is $K^{*\pm}K^\mp$ with $K^{*\pm}$ decaying to $K_S\pi^\pm$. There is no $K^+K^-(1750)$ signal in either of the two K^*K modes. In order to place upper limits on the K^*K/K^+K^- branching ratios of the $K^+K^-(1750)$, an estimate of the background is needed. The presence of a slight enhancement somewhat below the $\phi(1680)$ region introduces some ambiguity in estimating the background in the $K^+K^-(1750)$ region. In order to make a conservative estimate of the background, we have used a fit which includes a second, unconstrained, non-interfering resonance in the $1630\,\mathrm{MeV/c^2}$ region as well as the $K^+K^-(1750)$ with mass and width fixed from the fit to the K^+K^- mode. The size of the $K^+K^-(1750)$ resonant component was unconstrained. These fits provide an estimate of the number of events above background in the $K^+K^-(1750)$ region, -123 ± 120 events in the $K^{*0}K_S$ mode and 106 ± 117 in the $K^{*\pm}K^\mp$ mode.

The efficiencies of the K^+K^- and K^*K final states were determined by Monte Carlo simulations in bins of p_T, beam energy, and mass (see section 6.2.2). As the spin of

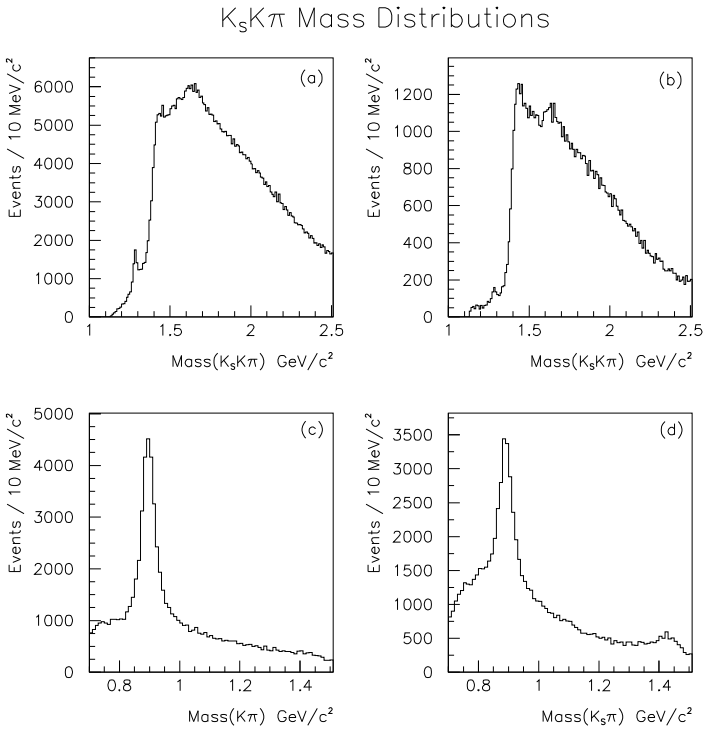

Figure 7.10: The $K_S K^{\pm}\pi^{\mp}$ mass distributions. (a) The $K_S K^{\pm}\pi^{\mp}$ sample with no cut on p_T. (b) The $K_S K^{\pm}\pi^{\mp}$ sample with $p_T < 0.15\,\mathrm{GeV/c}$. (c) The $K^{\pm}\pi^{\mp}$ mass from (b) showing a large K^{*0} component. (d) The $K_S\pi^{\pm}$ mass from (b) showing a large $K^{*\pm}$ component.

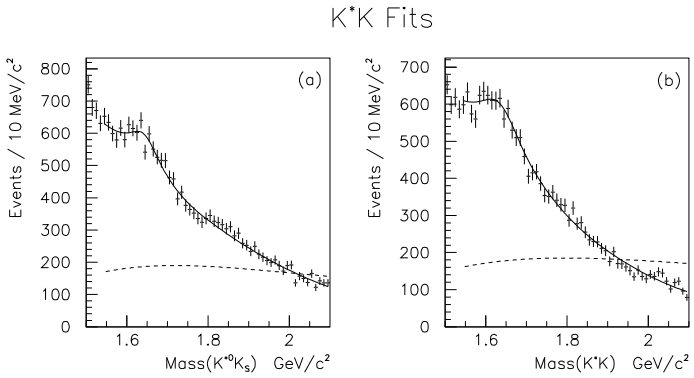

Figure 7.11: Fits to the K^*K mass spectra. The fits use a Breit-Wigner distribution for the $K^+K^-(1750)$ mass region with mass and width fixed from the fit to K^+K^-, a second non-interfering Breit-Wigner distribution with a mass around 1630 MeV/c^2, and a quadratic background. No signal is seen at a mass of 1750 MeV/c^2. The dotted lines are the Monte Carlo efficiencies on a scale from 0 to 20%. (a) $K^{*0}K_S$ with K^{*0} decaying to $K^\pm\pi^\mp$. (b) $K^{*\pm}K^\mp$ with $K^{*\pm}$ decaying to $K_S\pi^\pm$.

the $K^+K^-(1750)$ is still uncertain, several decay angular distributions were simulated. Using the highest efficiency for K^+K^- (figures 6.12 and 7.4.a) and the lowest for K^*K (figures 6.12 and 7.11) and correcting for the K_S unseen decay mode, we have found an upper limit on the following relative branching ratios

$$\frac{\Gamma(K^+K^-(1750) \to \overline{K}^{*0}K^0 \to K^-\pi^+K_S + c.c.)}{\Gamma(K^+K^-(1750) \to K^+K^-)} < 0.065 \text{ at } 90\% \text{ C.L.}$$

$$\frac{\Gamma(K^+K^-(1750) \to K^{*+}K^- \to K_S\pi^+K^- + c.c.)}{\Gamma(K^+K^-(1750) \to K^+K^-)} < 0.183 \text{ at } 90\% \text{ C.L.}$$

The confidence limits were set using the Feldman-Cousins methodology [98]. The two relative branching ratios were measured to be -0.083 ± 0.081 and 0.065 ± 0.072, respec-

tively.

7.5 Discussion

Because of the large discrepancies in mass and relative branching fractions to K^+K^- and K^*K, it is unreasonable to identify the $K^+K^-(1750)$ with the $\phi(1680)$. In fact, because the mass of the $K^+K^-(1750)$ is significantly higher than all known vector mesons, the most massive of which are the $\omega(1650)$, $\phi(1680)$, and $\rho(1700)$, an interpretation claiming the $K^+K^-(1750)$ is some combination of interfering vector mesons also seems highly unlikely. The next few chapters will open the door to a new interpretation.

Chapter 8

Production Characteristics of the $K^+K^-(1750)$

So far, it has been established that a resonance decaying to K^+K^- is photoproduced at a mass near $1750\,\mathrm{GeV/c^2}$. By measuring its mass and width, and by showing that it has no observable branching fraction to K^*K, we have shown that the $K^+K^-(1750)$ is not the same resonance as the $\phi(1680)$, as was previously thought. Further information about the $K^+K^-(1750)$ can be gathered by studying the mechanism through which it is produced. With the FOCUS spectrometer, two routes are open for this study. First, we can measure the t' dependence of $K^+K^-(1750)$ production, which roughly corresponds to the forwardness of production, i.e., how much the resonance is scattered with respect to the beam direction. Second, we can study the dependence of production

on the energy of the beam, which is directly related to $\sqrt{s}$, the center of mass energy[1]. In general, different production mechanisms show different dependences on t' and on $\sqrt{s}$, ideally providing a method of distinguishing between them. Furthermore, different production mechanisms provide different constraints on the types of resonances that can be produced. Thus, information on the way the $K^+K^-(1750)$ is produced leads to information about the nature of the $K^+K^-(1750)$ itself.

8.1 The t' Dependence of Production

Ideally, the t' distribution of the production of a particle can be used to distinguish between different production mechanisms[2]. For example, in the Primakoff effect [44], where the incoming photon interacts with photons of the nuclear Coulomb field, the t' distribution is expected to fall extraordinarily fast with increasing t', while in diffraction [43], where a phenomenological Pomeron is exchanged, the t' distribution is expected to fall slightly less steeply. Distinguishing between diffraction and the Primakoff effect, to name two possibilities, could lead to valuable information about the nature of the resonance produced. In diffraction, the resonance is likely to keep the quantum numbers of the original photon, $J^{PC} = 1^{--}$, while in Primakoff production (the same as a $\gamma\gamma$ collision, see section 2.5.4), the resonance must have even C-parity, in particular 0^{++} and 2^{++} are allowed and 1^{--} is not.

[1] The center of mass energy, $\sqrt{s}$, of photoproduction is given by $\sqrt{s} = (M_N^2 + 2M_N E_{BEAM})^{\frac{1}{2}}$, where M_N is the mass of the nucleon and E_{BEAM} is the energy of the photon beam (see Appendix B).

[2] Recall $t' \equiv |t| - |t|_{min} \approx p_T^2$, where $t \equiv (P_{BEAM} - P_{KK})^2$.

Unfortunately, two problems arise when using the t' distribution. First, despite years of study, the mechanism of photoproduction is yet to be understood satisfactorily. No reliable, quantitative predictions or measurements really exist for the t' distributions arising in photoproduction. Second, as discussed in section 6.1.2, the FOCUS detector cannot measure a t' distribution that falls faster than around $e^{-70t'}$. The t' resolution of the detector is limited by the uncertainty of the photon direction on an event by event basis.

While the FOCUS detector is incapable of distinguishing between t' distributions of $e^{-70t'}$ and anything steeper, the detector can at least distinguish between t' distributions that are steep and those that are shallow, shallow meaning a distribution falling something like $e^{-5t'}$. In general, the K^+K^- t' distributions of FOCUS can be fit with two exponentials, one with a steep slope and one with a shallow slope.

Figures 8.1 and 8.2 show the t' distributions for K^+K^- masses in the $\phi(1020)$ region and in the $K^+K^-(1750)$ region, respectively. Fitting with two exponentials, $a_1e^{-b_1t'} + a_2e^{-b_2t'}$, we find $b_1 = 77.71 \pm 0.59\,\mathrm{GeV}^{-2}\mathrm{c}^2$ and $b_2 = 1.71 \pm 0.14\,\mathrm{GeV}^{-2}\mathrm{c}^2$ for the $\phi(1020)$ region. Similarly, in the $K^+K^-(1750)$ region we find $b_1 = 69.2 \pm 2.1\,\mathrm{GeV}^{-2}\mathrm{c}^2$ and $b_2 = 4.17 \pm 0.21\,\mathrm{GeV}^{-2}\mathrm{c}^2$. The steep slopes cannot be taken literally since they are consistent with the resolution of the detector. Furthermore, the fits are performed on data that has not been corrected for efficiency. While the efficiency does not depend on t' for low-t' (see figure 6.11 of section 6.2.1), this may not be the case for higher t'. Thus, the exact values for the shallow slopes cannot be trusted either. Even with

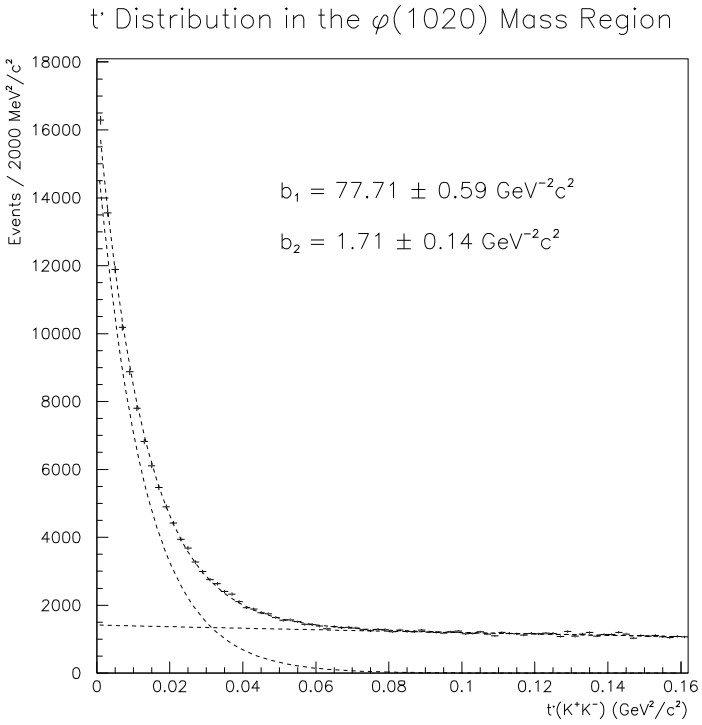

Figure 8.1: The t' distribution for the $\phi(1020)$ mass region. The distribution is fit with two exponentials, $a_1 e^{-b_1 t'} + a_2 e^{-b_2 t'}$. The steep slope is $b_1 = 77.71 \pm 0.59\,\mathrm{GeV}^{-2}\mathrm{c}^2$ and the shallow slope is $b_2 = 1.71 \pm 0.14\,\mathrm{GeV}^{-2}\mathrm{c}^2$.

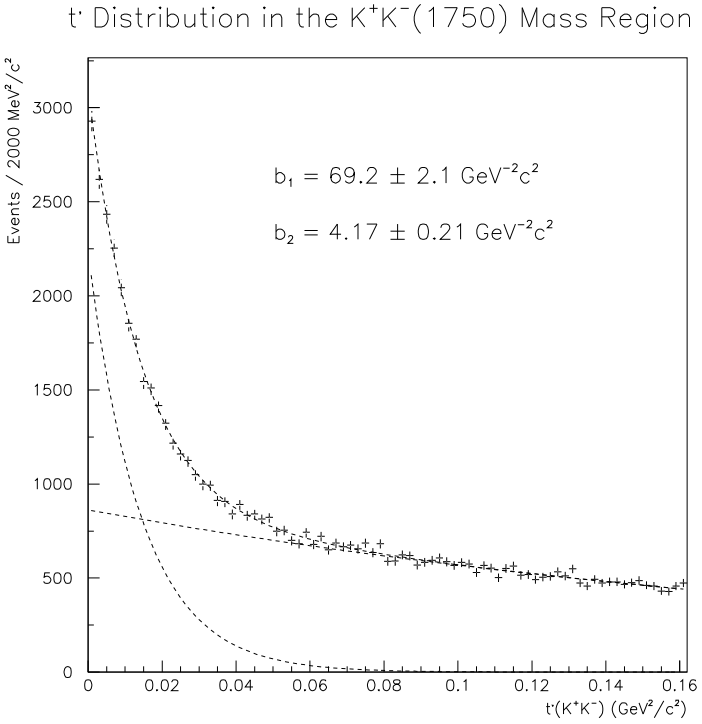

Figure 8.2: The t' distribution for the $K^+K^-(1750)$ mass region. The distribution is fit with two exponentials, $a_1 e^{-b_1 t'} + a_2 e^{-b_2 t'}$. The steep slope is $b_1 = 69.2 \pm 2.1\,\mathrm{GeV}^{-2}\mathrm{c}^2$ and the shallow slope is $b_2 = 4.17 \pm 0.21\,\mathrm{GeV}^{-2}\mathrm{c}^2$.

these caveats, however, figures 8.1 and 8.2 do show that the FOCUS detector is capable of effectively distinguishing between two broad categories of production mechanisms, those with a steep slope and those with a shallow slope.

Taking advantage of the two different exponentials of the t' distribution, events may be weighted according to their values of t'. Weighting events with the factor

$$W_{steep} = \frac{a_1 e^{-b_1 t'}}{a_1 e^{-b_1 t'} + a_2 e^{-b_2 t'}} \tag{8.1}$$

will isolate the steep part of the production. Similarly, weighting with the factor

$$W_{shallow} = \frac{a_2 e^{-b_2 t'}}{a_1 e^{-b_1 t'} + a_2 e^{-b_2 t'}} \tag{8.2}$$

will isolate the shallow part. The t' distributions were fit separately for 25 bins of K^+K^- mass between 1.0 and 2.0GeV/c^2. These fit results were then used to weight events with both the steep weight and the shallow weight, given above. The results of this weighting on the K^+K^- mass distribution are shown in figure 8.3. In figures 8.3.c and 8.3.d, one sees dramatic evidence that the $K^+K^-(1750)$ is only produced with the steeper slope. By contrast, figures 8.3.a and 8.3.b suggest that the $\phi(1020)$ is produced dominantly with a steep t' distribution, but may contain some small shallow component in addition. The uncertainties in measuring t' are too large to be able to do any further analysis, such as giving a ratio of the steep $\phi(1020)$ production to the shallow production.

Ideally, one could also use this method of weighting to weight angular distributions,

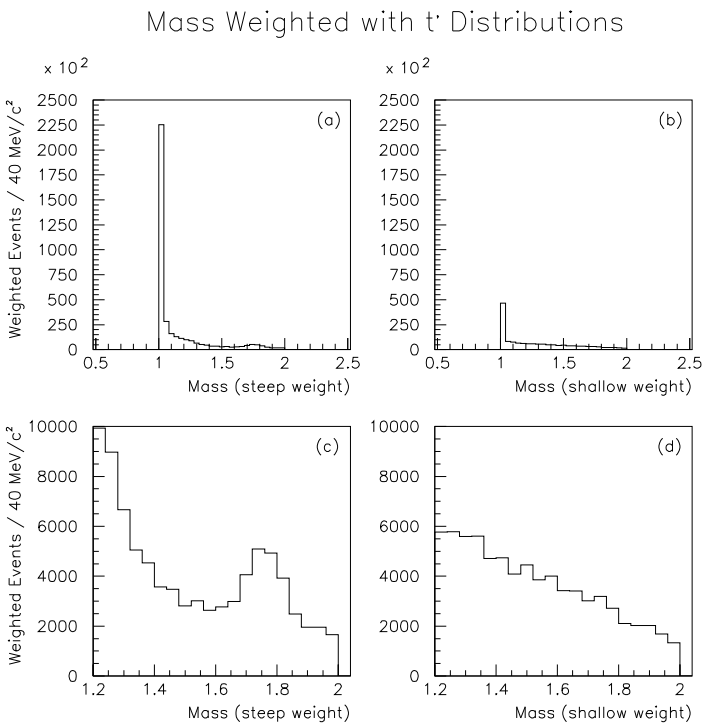

Figure 8.3: The K^+K^- mass distribution weighted by t' distribution fits. Events are weighted by the results of t' fits in 25 mass bins from 1.0 to 2.0 GeV/c^2. (a) The mass distribution in the $\phi(1020)$ region weighted with the steep slope. (b) The mass distribution in the $\phi(1020)$ region weighted with the shallow slope. (c) The $K^+K^-(1750)$ region with the steep slope weighting. (d) The $K^+K^-(1750)$ region with the shallow slope weighting.

thus separating the angular distribution of K^+K^- pairs produced steeply in t' and those produced shallowly. However, because of the complicated angular acceptances (see sections 6.1.3 and 6.2.3), the angular distributions can only be studied for events with $p_T < 0.15\,\mathrm{GeV/c}$, the standard cut of this analysis. Such a sharp cut in p_T, which corresponds to a sharp cut in t', severely limits the effectiveness of any weighting based on t'.

8.2 The Beam Energy Dependence of Production

In addition to the t' dependence of the production of a resonance, the dependence on the beam energy (or $\sqrt{s}$ in the center of mass) can also be used to shed light on the production mechanism. To gain perspective on the beam energy dependence of the production of the $K^+K^-(1750)$, the production of the $K^+K^-(1750)$ will be compared to $\phi(1020)$ production, which is presumed to occur predominantly through VDM and diffraction[3]. All 1^{--} mesons produced diffractively at high energies have roughly the same dependence on beam energy (see figure 3.1). If the $K^+K^-(1750)$ were also 1^{--} and were produced diffractively, we would expect the ratio of $\phi(1020)$ production to $K^+K^-(1750)$ production to be flat as a function of beam energy. This is not what is found.

Figures 8.4 and 8.5 show acceptance-corrected K^+K^- mass plots for various ranges of beam energy in the $\phi(1020)$ and $K^+K^-(1750)$ mass regions, respectively. The

[3]That is, we presume the photon, through VDM, acts as a $\phi(1020)$ meson. The exchanged Pomeron of diffraction then provides the energy necessary to materialize the photon.

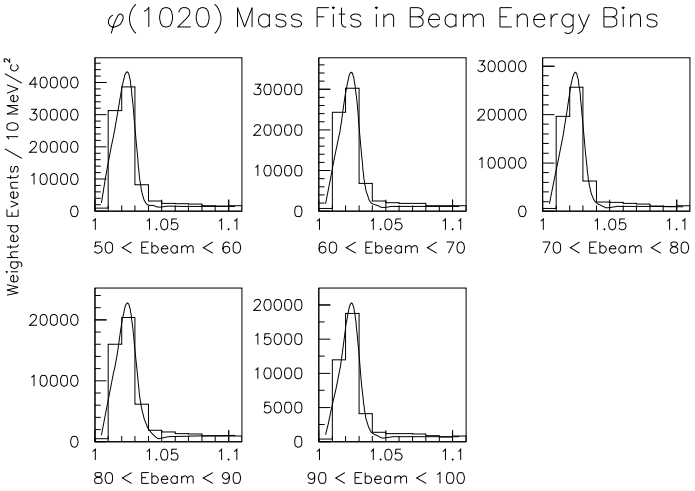

Figure 8.4: Fits to the $\phi(1020)$ signal for different ranges of beam energy.

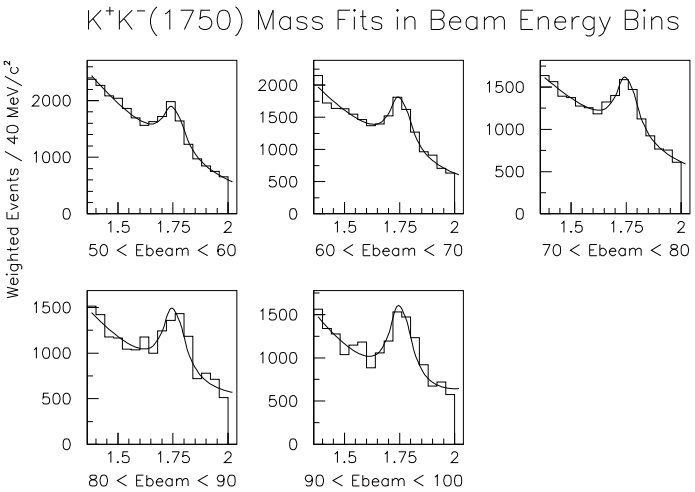

Figure 8.5: Fits to the $K^+K^-(1750)$ signal for different ranges of beam energy.

range from 50 to 100 GeV was chosen for the beam energy for two reasons. First, the $K^+K^-(1750)$ signal is relatively clean in this region. Second, the efficiencies as a function of beam energy for the $\phi(1020)$ and $K^+K^-(1750)$ are most similar in this region (see figure 6.10 of section 6.2.1), and since the ratio between $\phi(1020)$ and $K^+K^-(1750)$ production will be used, this similarity in efficiencies will minimize systematic errors due to uncertainty in the Monte Carlo simulations of the efficiency. The beam energy bin sizes were chosen to be 10 GeV in order to have adequate statistics in each bin, and in order to be well above the beam energy resolution of around 1 GeV (see section 5.2). The acceptance corrections were done on an event by event basis according to the K^+K^- mass, the beam energy, and the $\cos\theta$ of the decay of each event. The event by event corrections are described in section 6.2.3.

The $\phi(1020)$ mass distributions have been fit with a second degree polynomial background and a Gaussian for the signal (figure 8.4). Bin sizes are 10 MeV/c^2 in this region. The $K^+K^-(1750)$ mass distributions were fit with a second degree polynomial background and a Breit-Wigner distribution for the signal (figure 8.5). The mass and width of the Breit-Wigner were fixed to the values measured in chapter 7. Bin sizes are 40 MeV/c^2. Notice that the $K^+K^-(1750)$ production differs from the production of the background; the signal over background increases significantly as a function of beam energy.

The results of the fits were combined to calculate a production ratio for the $\phi(1020)$ over the $K^+K^-(1750)$, shown in figure 8.6. Notice that the $K^+K^-(1750)$ production

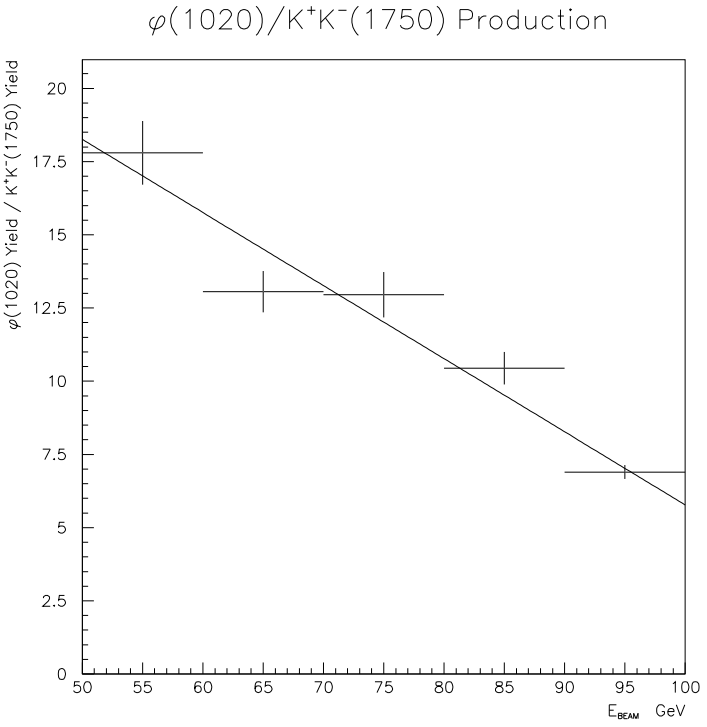

Figure 8.6: The ratio of $\phi(1020)$ production to $K^+K^-(1750)$ production as a function of beam energy. The solid line is a straight line fit.

grows significantly with respect to the $\phi(1020)$ production as a function of beam energy. The pattern is similar to the signal over background for the $K^+K^-(1750)$. The ratio can be fit rather well with a straight line. The fact that the ratio of production is not flat with beam energy indicates that the $K^+K^-(1750)$ is not being produced diffractively in the same manner as the ρ, ω, and ϕ mesons, and widens the possibility that the $K^+K^-(1750)$ has a J^{PC} other than 1^{--}.

8.3 Discussion

From the above analyses of the production of the $K^+K^-(1750)$, two things can be concluded. First, the t' distribution corresponding to $K^+K^-(1750)$ production falls faster than $ae^{-bt'}$ with $b = 69.2 \pm 2.1\ \mathrm{GeV}^{-2}\mathrm{c}^2$. Second, the energy dependence of the $K^+K^-(1750)$ production differs significantly from the production of the $\phi(1020)$. Since all of the vector mesons known to be photoproduced have roughly the same dependence on beam energy, the second conclusion allows one to begin to question the widely held assumption that the $K^+K^-(1750)$ has a $J^{PC} = 1^{--}$.

Chapter 9

Angular Analysis of the $K^+K^-(1750)$ Decay

9.1 Theoretical Overview

By evoking the conservation of angular momentum, the spin of a decaying particle can often be inferred from the angular distribution of its decay products[1]. In spectroscopy, it is usually the case that the spins of all the final particles are known (e.g., kaons or pions), and it is the spin of the decaying particle that is of interest. The angular distribution provides information on the orbital angular momentum between the decay products. Combining the orbital angular momentum with the known intrinsic angular momenta (spins) of the decay products leads to constraints on the spin of the decaying

[1] For an introduction to the methods of angular analyses, see references [99, 100, 101]. For detailed examples using these methods, see [102, 103]

particle through the conservation of angular momentum. If two particles are in the final state, the conservation of angular momentum takes the form:

$$\vec{J} = \vec{L} + \vec{S}_1 + \vec{S}_2, \tag{9.1}$$

where J is the spin of the decaying particle, L is the orbital angular momentum between the decay products, and S_1 and S_2 are the spins of the two decay products, respectively. If S_1 and S_2 are zero, as in the case of a decay to two kaons, then the spin of the decaying particle is simply the orbital angular momentum between the decay products.

The basic idea of any angular analysis can be expressed in the following example. Suppose a particle with unknown spin J is at rest and carries M units of angular momentum along the $+z$ direction, i.e., the particle is in the state $|JM\rangle$. If the particle decays to two spin-0 particles, then the original intrinsic angular momentum of the parent particle must translate into orbital angular momentum between the two decay particles. Since orbital angular momentum is described by the spherical harmonics, Y_L^M, the wavefunction of the final two-particle system will contain a factor $Y_J^M(\theta, \phi)$, where θ and ϕ are the polar and azimuthal angles, respectively, of one of the decay products measured relative to the z direction. The angular distribution will then be:

$$I(\theta, \phi) \propto |Y_J^M(\theta, \phi)|^2. \tag{9.2}$$

If the parent particle were in the state $|JM\rangle = |11\rangle$ (as would be the case for a polarized

$\phi(1020)$ decaying to K^+K^-) then the angular distribution of the decay products would be:

$$I(\theta,\phi) \propto |Y_1^1(\theta,\phi)|^2 = \frac{3}{8\pi}\sin^2\theta. \tag{9.3}$$

If, on the other hand, the parent particle were in the state $|JM\rangle = |21\rangle$ (to take a random example) then the angular distribution would be

$$I(\theta,\phi) \propto |Y_2^1(\theta,\phi)|^2 = \frac{15}{8\pi}\sin^2\theta\cos^2\theta. \tag{9.4}$$

Thus, by measuring the angular distributions of the decay products, one can distinguish between different possibilities for the spin of the decaying particle.

For an angular analysis to work, it is essential that the decaying particle be produced in some polarization state, otherwise the decay would be isotropic regardless of the particle's spin. Furthermore, we must have some idea of the axis along which the particle is polarized. In diffractive photoproduction, it is most often assumed that the resonance will be produced with its polarization along the photon beam direction. This assumption is called s-Channel Helicity Conservation (SCHC) [49] and stems from the fact that real photons are always polarized along the direction of their velocity. When SCHC is assumed, the Gottfried-Jackson coordinate system is appropriate [104]. The z-axis is the photon beam direction in the rest frame of the decaying particle; the y-axis is the cross product of the beam direction and the resonance direction in the overall center of mass (i.e., normal to the production plane); and the x-axis is $\hat{y} \times \hat{z}$. The

Gottfried-Jackson coordinate system is used throughout this analysis[2].

In the general case, rather than just producing an isolated resonance as in the example above, a superposition of interfering resonances are present in any final state, and the result is a more complicated angular distribution. To analyze angular distributions where more than one resonance is present, the angular distribution is expanded in a set of basis functions. One way this can be done is to expand the amplitude before squaring it[3]:

$$I(\Omega) = |\sum_{lm} V_{lm} A_{lm}(\Omega)|^2. \tag{9.5}$$

The $A_{lm}(\Omega)$ are referred to as the decay amplitudes, and the V_{lm} are the production amplitudes. The decay amplitudes are known functions forming an orthonormal basis that can be chosen in different ways. The spherical harmonics are often used, as in the example above. In photoproduction, it is more convenient to use a basis closely related to the spherical harmonics, the reflectivity basis, described later. The production amplitudes are unknown complex numbers that indicate how much of each wave is present and are measured by fitting the angular distribution with the above expansion. The advantage of expanding the amplitude (rather than the intensity, $I(\Omega)$) is that the A_{lm} then correspond to the physically meaningful partial waves, in which case each

[2]The other popular coordinate system, the helicity frame, takes the z-axis to be the resonance direction in the center of mass. For the subsequent analysis, the helicity frame and the Gottfried-Jackson frame are not substantially different due to the tight low-p_T requirement. That is, the resonance direction is not substantially different from the beam direction.

[3]The angular distribution itself can also be expanded, $I(\Omega) = \sum_i \alpha_i F_i(\Omega)$, where the $F_i(\Omega)$ form a basis of orthonormal functions, and the α_i are the expansion coefficients. This method will be used in analyzing moments.

$|V_{lm}|^2$ indicates how much of that wave is present, and the complex parts of the different V_{lm} contain information about the interference structure. The disadvantage is that the expansion is often not unique, and the more waves that are included in the expansion, the more ambiguous solutions there will be. To solve the uniqueness problem, further assumptions and expectations must be incorporated.

The reflectivity basis uses a set of functions ${}^{\epsilon}A_{lm}(\Omega)$ as the basis functions, which are defined in a way that takes advantage of the conservation of parity in the production process [105]:

$$ {}^{\epsilon}A_{lm}(\Omega) \equiv \Theta(m)[Y_l^m(\Omega) - \epsilon(-1)^m Y_l^{-m}(\Omega)], \tag{9.6} $$

where

$$ \Theta(m) \equiv \begin{cases} \frac{1}{\sqrt{2}}, & m > 0; \\ \frac{1}{2}, & m = 0; \\ 0, & m < 0. \end{cases} \tag{9.7} $$

The reflectivity, ϵ, can be either + or −, and is related to the parity of the particle exchanged during production[4]. The distinction between positive and negative reflectivity will be unimportant for what follows. The expansion of the angular distribution now takes the following form:

$$ I(\Omega) = |\sum_{\epsilon lm} {}^{\epsilon}V_{lm}\, {}^{\epsilon}A_{lm}(\Omega)|^2. \tag{9.8} $$

Making the restrictions $l \leq 2$ and $m \leq 1$, seven decay amplitude functions are

[4]The reflectivity is identical to the naturality of the exchanged particle. A particle of spin J has positive reflectivity if its parity $P = (-1)^J$ and negative reflectivity otherwise.

present in the expansion [106]:

$$^{-}A_{00}(\Omega),\ ^{-}A_{10}(\Omega),\ ^{-}A_{11}(\Omega),\ ^{-}A_{20}(\Omega),\ ^{-}A_{21}(\Omega),\ ^{+}A_{11}(\Omega),\ \text{and}\ ^{+}\mathrm{A}_{21}(\Omega),$$

which correspond to seven production amplitudes:

$$^{-}V_{00},\ ^{-}V_{10},\ ^{-}V_{11},\ ^{-}V_{20},\ ^{-}V_{21},\ ^{+}V_{11},\ \text{and}\ ^{+}\mathrm{V}_{21}.$$

Using S, P, and D for $l = 0, 1, 2$, respectively, the seven production amplitudes can be renamed:

$$S_0,\ P_0,\ P_-,\ D_0,\ D_-,\ P_+,\ \text{and}\ \mathrm{D}_+.$$

These seven waves will be used in describing the K^+K^- angular analysis that follows.

If only a P_- wave were present in the final state, for example, the angular distribution would take the form:

$$I(\Omega) = |^{-}A_{11}(\Omega)|^2 = \frac{3}{4\pi}\sin^2\theta\sin^2\phi. \tag{9.9}$$

Figure 9.1 shows the angular distributions corresponding to the P_- wave, the P_+ wave, a combination of the P_- and P_+ waves, and the P_0 wave. Figure 9.2 shows the same thing for D-waves. The S_0 wave simply produces an isotropic angular distribution and is not shown.

Since FOCUS is unable to precisely determine the ϕ angle due to uncertainty in the

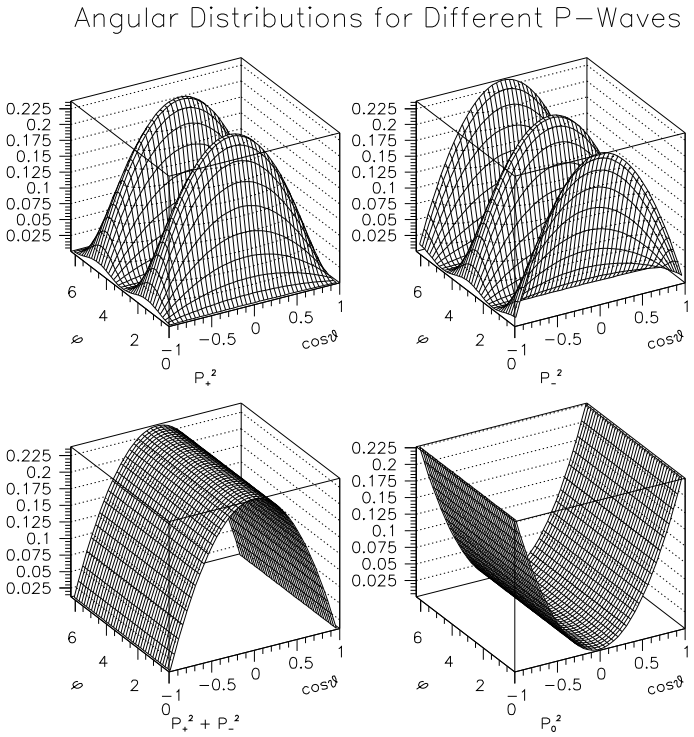

Figure 9.1: Theoretical angular distributions for P-waves. The distributions correspond to $|^{+}A_{11}(\Omega)|^2$, $|^{-}A_{11}(\Omega)|^2$, $|^{+}A_{11}(\Omega)|^2 + |^{-}A_{11}(\Omega)|^2$, and $|^{-}A_{10}(\Omega)|^2$. (see equation 9.6).

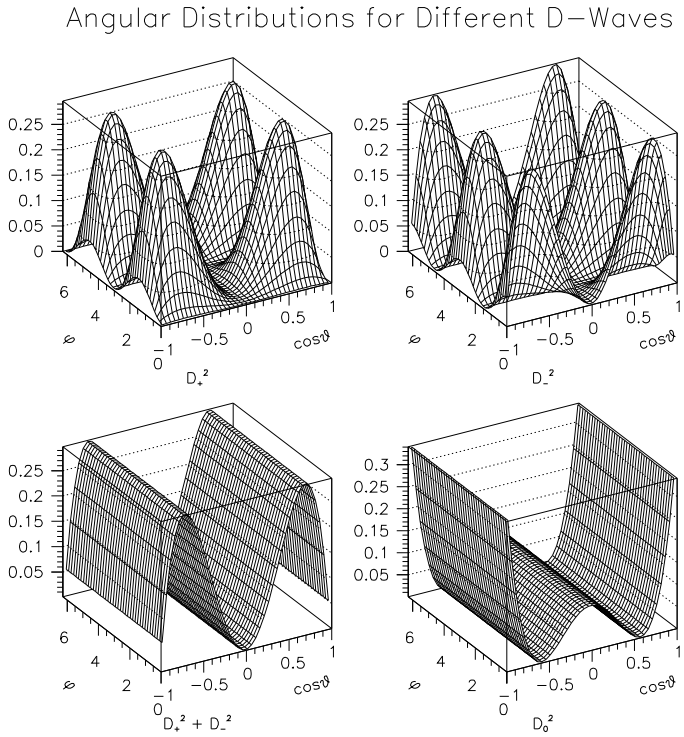

Figure 9.2: Theoretical angular distributions for D-waves. The distributions correspond to $|^{+}A_{21}(\Omega)|^2$, $|^{-}A_{21}(\Omega)|^2$, $|^{+}A_{21}(\Omega)|^2 + |^{-}A_{21}(\Omega)|^2$, and $|^{-}A_{20}(\Omega)|^2$. (see equation 9.6).

beam direction (see section 6.1.3), the experiment is unable to distinguish between P_- and P_+ waves or between D_- and D_+ waves. This inhibits a full partial wave analysis to be performed on the K^+K^- system, but still allows us to distinguish between P-waves and D-waves using only the $\cos\theta$ distributions if we combine the P_- and P_+ waves and the D_- and D_+ waves as shown in figure 9.3. If a resonance is produced as P_-, for example, and if all ϕ information is lost, then the resonance will be reconstructed as a combination of P_- and P_+ waves, which has the same $\cos\theta$ structure. In the following analysis, only the $\cos\theta$ distributions are studied. The projections of the angular distributions onto the $\cos\theta$ axis (figure 9.3) show that the five scenarios (1) S_0 (not shown because it is simply isotropic), (2) P_0, (3) P_- or P_+, (4) D_0, and (5) D_- or D_+ are clearly distinguishable.

9.2 Acceptance Corrected Angular Distributions

To get a rough idea of the shapes of the angular distributions for various mass regions of the K^+K^- spectrum, each event has been weighted according to its beam energy, mass, $\cos\theta$, and ϕ in order to account for the finite acceptance of the detector. The general method of event by event weighting is described in section 6.2.3. Once the events have been weighted, the resulting angular distributions are plotted (see figure 9.4). This method of accounting for the acceptance is somewhat tenuous due to the very poor acceptances around $\cos\theta = \pm 1$. Events in this region of low acceptances receive a dangerously large weight. Furthermore, only the $\cos\theta$ portion of the distributions are

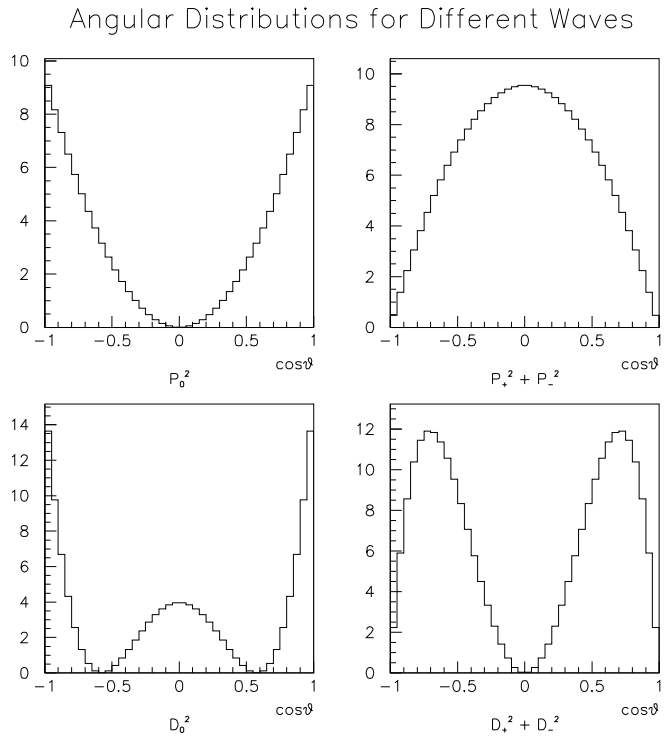

Figure 9.3: A projection of partial waves onto the $\cos\theta$ axis. These combinations of waves do not depend on the azimuthal angle, ϕ, of the decay. There is clear separation between these four combinations of waves. If the $K^+K^-(1750)$ were spin-1 it would decay according to one of the top distributions; if spin-2 the decay would look like one of the bottom two distributions. A spin-0 decay would be isotropic in $\cos\theta$.

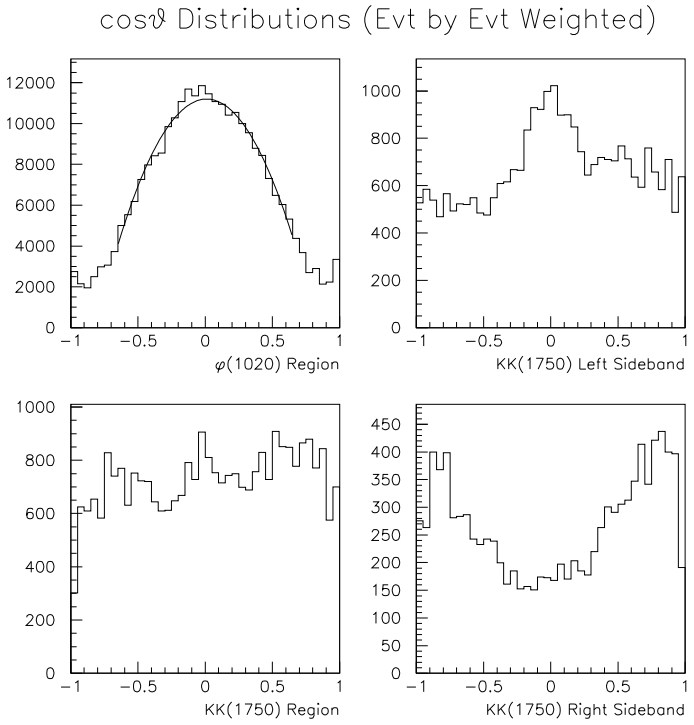

Figure 9.4: Acceptance-corrected $\cos\theta$ distributions. The distributions are for (a) the $\phi(1020)$ region; (b) the $K^+K^-(1750)$ left sideband; (c) the $K^+K^-(1750)$ signal region; and (d) the $K^+K^-(1750)$ right sideband. The middle region of the $\cos\theta$ distribution for the $\phi(1020)$ has been fit with a $\sin^2\theta$ curve.

plotted because of the poor ϕ resolution (see section 6.1.3).

The $\phi(1020)$ angular distribution has been extensively studied historically by previous photoproduction experiments, and it has been found that the $\phi(1020)$ is photoproduced polarized along the photon beam direction, agreeing with the SCHC assumption. The resulting angular distribution is then proportional to $\sin^2\theta$ (see equation 9.3). Thus, the FOCUS $\phi(1020)$ angular distribution can serve as a benchmark. Figure 9.4.a shows the angular distribution for the $\phi(1020)$ mass region. The distribution has been fit with a $\sin^2\theta$ curve. The fit is excellent from $-0.7 < \cos\theta < 0.7$, but becomes poor in the extremities of $\cos\theta$. This is due to the poor acceptances in this region and the resulting difficulty in accounting for the acceptance on an event by event basis. This distrust of the $\cos\theta$ distribution around the extremities carries over into the $K^+K^-(1750)$ analysis.

Figures 9.4.b, 9.4.c, and 9.4.d show the acceptance corrected $\cos\theta$ distributions for the $K^+K^-(1750)$ left sideband, signal region, and right sideband, respectively. It is hard to conclude anything from these distributions due to the complexity of the sidebands and the fact that the sidebands differ from each other so radically.

9.3 The Angular Distribution from Mass Fits

Assuming there is little or no interference between the $K^+K^-(1750)$ signal and the background beneath it, the $K^+K^-(1750)$ angular distribution can be isolated from the background by performing mass fits in bins of $\cos\theta$, and plotting the yield of $K^+K^-(1750)$ events in each bin as a function of $\cos\theta$. To accomplish this, the K^+K^- events have

been divided into ten bins of $\cos\theta$. The acceptance-corrected mass distributions are shown in figure 9.5 in order of increasing $\cos\theta$. Notice that the $K^+K^-(1750)$ clearly has a different angular structure from the background beneath it. Mass fits have been performed with Breit-Wigner distributions with mass and width fixed to the final values of chapter 7, and with second degree polynomials for the background shapes.

Figure 9.6 shows the resulting angular distribution. Again, it should be remembered that the extremes of $\cos\theta$ are unreliable. The center of the distribution, however, which can be trusted, shows a clear dip that is entirely inconsistent with $J^{PC} = 1^{--}$. Comparing the angular distribution to the theoretical curves (figure 9.3), the spin-2 distribution appears most similar. The fact that the distribution does not look precisely spin-2 could be due to interference with the background, or perhaps the polarization direction is somewhat inaccurate. The general structure of the $K^+K^-(1750)$ angular distribution, however, is indicative of a $J^{PC} = 2^{++}$ resonance.

9.4 Moments

9.4.1 Defining Moments

Further information about the angular structure of a system can be gained through a moments analysis [106]. The idea is to expand the angular distribution in bins of mass and beam energy using a set of $D^l_{m0}(\Omega)$ as the basis functions:

$$I(\Omega) = \sum_{lm} \frac{2l+1}{4\pi} \tau(m) t_{lm} \mathrm{Re}\{\mathrm{D}^{\mathrm{l}}_{\mathrm{m0}}(\Omega)\}, \tag{9.10}$$

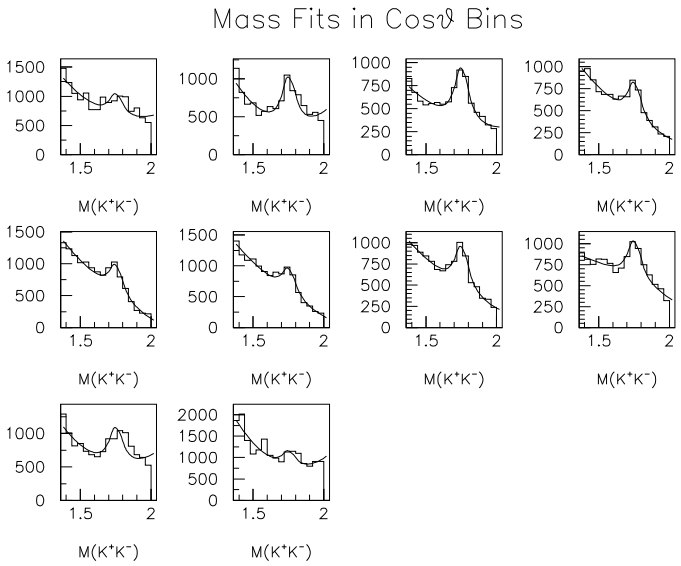

Figure 9.5: Mass fits of the $K^+K^-(1750)$ in bins of $\cos\theta$. The ten $\cos\theta$ bins from -1.0 to 1.0 are shown in increasing order from left to right, top to bottom. Notice that the signal to background changes from bin to bin, indicating that the $K^+K^-(1750)$ has a different angular structure from the background.

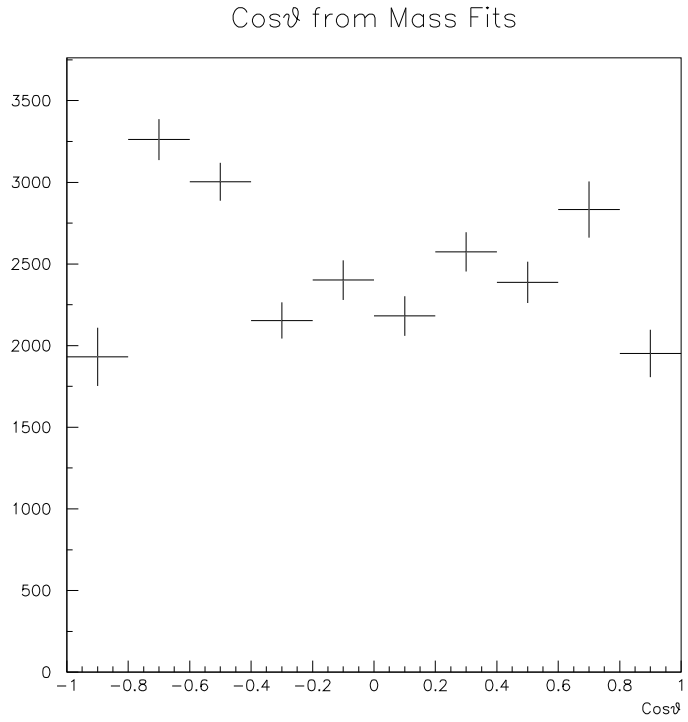

Figure 9.6: The $K^+K^-(1750)$ $\cos\theta$ distribution obtained from mass fits. The yield from each of the ten mass fits is plotted as a function of $\cos\theta$. Compare this figure to figure 9.3. The distribution is indicative of a $J^{PC} = 2^{++}$ for the $K^+K^-(1750)$.

where

$$\tau(m) \equiv \begin{cases} 2, & m > 0; \\ 1, & m = 0; \\ 0, & m < 0. \end{cases} \quad (9.11)$$

The real expansion coefficients, t_{lm}, are referred to as the moments. Every mass and beam energy bin will have its own set. The first index, l, can be any integer greater than or equal to zero; the second, m, is an integer between zero and l. The basis functions $D^l_{m0}(\Omega)$ are chosen by convention and are related to the familiar spherical harmonics through

$$D^l_{m0}(\Omega) \equiv \sqrt{\frac{4\pi}{2l+1}} Y_l^{m*}(\Omega). \quad (9.12)$$

Individual moments can be picked out of the expansion by utilizing the orthogonality of the $D^l_{m0}(\Omega)$:

$$t_{lm} = \int I(\Omega) D^l_{m0}(\Omega) d\Omega. \quad (9.13)$$

An expansion in terms of moments is significantly simpler than the partial wave expansion described earlier in this chapter. In particular, the moment expansion is unique. By contrast, in the partial wave formalism the amplitude is expanded before it is squared, leading to nonlinearity and ambiguities among the expansion coefficients. What is sacrificed in a moment expansion is the direct physical insight of the partial waves, but much can still be learned from the moments.

If we assume only seven partial waves are present in the angular distribution (S_0, P_0, P_-, D_0, D_-, P_+, and D_+), then twelve moments are needed in the moment expansion.

This corresponds to the number of free parameters in the partial wave expansion since each of the seven waves is complex and two of the phases can be fixed arbitrarily. The twelve moments are nonlinear functions of the partial wave amplitudes:

$$t_{00} = S_0^2 + P_0^2 + P_-^2 + D_0^2 + D_-^2 + P_+^2 + D_+^2$$

$$t_{10} = \frac{1}{\sqrt{3}} S_0 P_0 + \frac{2}{\sqrt{15}} P_0 D_0 + \frac{1}{\sqrt{5}} (P_- D_- + P_+ D_+)$$

$$t_{11} = \frac{1}{\sqrt{6}} S_0 P_- + \frac{1}{\sqrt{10}} P_0 D_- - \frac{1}{\sqrt{30}} P_- D_0$$

$$t_{20} = \frac{1}{\sqrt{5}} S_0 D_0 + \frac{2}{5} P_0^2 - \frac{1}{5} (P_-^2 + P_+^2) + \frac{2}{7} D_0^2 + \frac{1}{7} (D_-^2 + D_+^2)$$

$$t_{21} = \frac{1}{\sqrt{10}} S_0 D_- + \frac{1}{5} \sqrt{\frac{3}{2}} P_0 P_- + \frac{1}{7\sqrt{2}} D_0 D_-$$

$$t_{22} = \frac{1}{5} \sqrt{\frac{3}{2}} (P_-^2 - P_+^2) + \frac{1}{7} \sqrt{\frac{3}{2}} (D_-^2 - D_+^2)$$

$$t_{30} = \frac{3}{7\sqrt{5}} (\sqrt{3} P_0 D_0 - P_- D_- - P_+ D_+)$$

$$t_{31} = \frac{1}{7} \sqrt{\frac{3}{5}} (2 P_0 D_- + \sqrt{3} P_- D_0)$$

$$t_{32} = \frac{1}{7} \sqrt{\frac{3}{2}} (P_- D_- - P_+ D_+)$$

$$t_{40} = \frac{2}{7} D_0^2 - \frac{4}{21} (D_-^2 + D_+^2)$$

$$t_{41} = \frac{1}{7} \sqrt{\frac{5}{3}} D_0 D_-$$

$$t_{42} = \frac{\sqrt{10}}{21} (D_-^2 - D_+^2).$$

A simplified notation has been used in the above, where, for example:

$$S_0^2 \equiv |S_0|^2,$$

and

$$P_0 D_0 \equiv \mathrm{Re}\{\mathrm{P_0 D_0^*}\}.$$

Inverting these equations leads to eight ambiguous sets of solutions for the partial waves. However, a few things can be learned just from inspection. For example, if any signal is present in t_{40}, t_{41}, or t_{42}, then it must be due to a D-wave, since these moments are composed only of D-waves. Furthermore, a strong P_- wave, indicative of diffractive photoproduction with SCHC, will show up strongly in t_{20}.

9.4.2 Measuring Moments

There are two methods for measuring experimental moments when there is a finite acceptance. The simpler of the two methods is to weight each event according to its beam energy, mass, $\cos\theta$, and ϕ. The method is dangerous, however, when there are regions with very low acceptance (as in the FOCUS experiment), because events in this region get exaggerated weights. The second method is to perform a likelihood fit. Here, the finite detector acceptance is handled more rigidly. The two methods provide a cross check for each other.

To find acceptance-corrected moments by correcting each event individually, the

integral in equation 9.13 is simply expanded:

$$t_{lm} = \int I(\Omega) D^l_{m0}(\Omega) d\Omega \approx \sum_{i=1}^{n} D^l_{m0}(\Omega_i) \times wt(\Omega_i), \tag{9.14}$$

where the weight for event i, $wt(\Omega_i)$, is determined by the Monte Carlo simulations described in chapter 6. The sum is over all events in the mass and beam energy bin under consideration.

The likelihood method is more involved. First, start with an extended likelihood function:

$$L = \frac{e^{-\mu}\mu^n}{n!} \prod_{i=1}^{n} \frac{I(\Omega_i)}{\int \eta(\Omega) I(\Omega) d\Omega}, \tag{9.15}$$

where n is the observed number of events in a given mass and beam energy bin, $I(\Omega)$ is the corrected angular distribution to be expanded in moments, and

$$\mu \equiv \int \eta(\Omega) I(\Omega) d\Omega \tag{9.16}$$

is the expected number of events in this mass and beam energy bin. $\eta(\Omega)$ is the efficiency function. The first factor in the expression for the likelihood function is the Poisson probability for observing n events in a bin when μ events are expected. The product is over the probabilities for each event i to have angles Ω_i. This likelihood function will be maximized using the t_{lm} as free parameters.

Maximizing L has the same effect as minimizing $-2 \ln L$. Taking the natural log of

the likelihood function gives:

$$-2\ln L = -2\sum_{i=1}^{n}\ln I(\Omega_i) + 2\int \eta(\Omega)I(\Omega)d\Omega. \tag{9.17}$$

Both occurrences of $I(\Omega)$ are expanded in terms of moments prior to the minimization. The finite acceptance of the detector is entirely accounted for in the second term. Expanding the integral in the second term we can further isolate the effects of the acceptance,

$$\int \eta(\Omega)I(\Omega)d\Omega = \sum_{lm}\frac{2l+1}{4\pi}\tau(m)t_{lm}\int \eta(\Omega)\mathrm{Re}\{\mathrm{D}^{\mathrm{l}}_{\mathrm{m0}}(\Omega)\}\mathrm{d}\Omega. \tag{9.18}$$

The integral on the right hand side of this equation can be evaluated with Monte Carlo simulated events:

$$\int \eta(\Omega)\mathrm{Re}\{\mathrm{D}^{\mathrm{l}}_{\mathrm{m0}}(\Omega)\}\mathrm{d}\Omega \approx \frac{4\pi}{N_{gen}}\sum_{i=1}^{N_{acc}}\mathrm{Re}\{\mathrm{D}^{\mathrm{l}}_{\mathrm{m0}}(\Omega_{\mathrm{i}})\}, \tag{9.19}$$

where N_{gen} and N_{acc} are the number of generated and accepted Monte Carlo events, respectively, in a given bin of mass and beam energy. This sum is performed using the same Monte Carlo events that are used in the event by event corrections, and results in a matrix of values that are calculated prior to any fitting. Substituting these values into the expression for $-2\ln L$, expanding $I(\Omega)$ in terms of moments to be treated as free parameters, and minimizing using MINUIT [107] for each bin of mass and beam

energy results in the desired sets of moments.

The detector acceptances to be used in measuring the moments were determined by a large Monte Carlo simulation consisting of 100 million generated K^+K^- events. Events were generated flat in mass between 1.0 and 2.0 $\mathrm{GeV/c^2}$, flat in p_T between 0.0 and 0.15 $\mathrm{GeV/c}$, and flat in both $\cos\theta$ and ϕ. Two different values of beam energy were used, 55 GeV and 85 GeV.

9.4.3 A Test Case

To test the above methods for measuring moments, a small Monte Carlo simulation was performed. Known partial waves and moments were generated and sent through the simulated detector, and then the fitting routines and acceptance corrections were employed on the reconstructed data to check that the measured moments match those that were generated. Approximately 600,000 K^+K^- events were generated with beam energy flat between 80 and 90 GeV, and p_T flat between 0.0 and 0.15 $\mathrm{GeV/c}$. Three waves were generated: 70% of the total events were in an S_0 wave with a mass of 1500 $\mathrm{MeV/c^2}$ and width of 500 $\mathrm{MeV/c^2}$; 15% were in a P_- wave with a mass of 1100 $\mathrm{MeV/c^2}$ and width of 50 $\mathrm{MeV/c^2}$; and the remaining 15% were in a D_+ wave with a mass of 1700 $\mathrm{MeV/c^2}$ and width of 150 $\mathrm{MeV/c^2}$. The generated mass distribution is shown in figure 9.7.

The generated moments are the solid black lines of figure 9.8. As an intermediate step in the test case, the generated moments were fit using the likelihood method with perfect detector acceptance ($\eta(\Omega) = 1$). The blue points are the results of the likelihood fits and their agreement with the generated moments verifies that the fitting routines

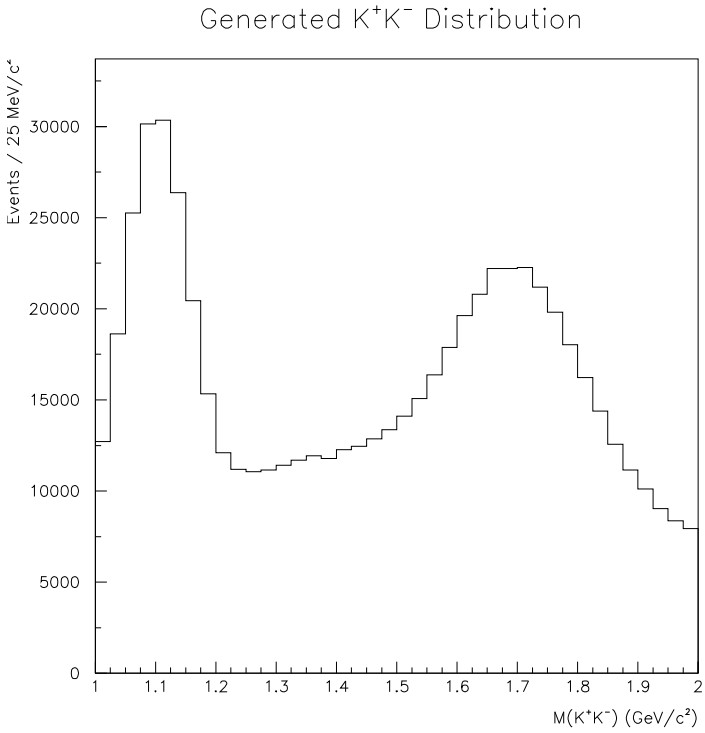

Figure 9.7: A Monte Carlo generated mass distribution to test the methods for measuring moments. The distribution was generated with 70% S_0 wave with mass 1500 MeV/c^2 and width 500 MeV/c^2; 15% P_- wave with mass 1100 MeV/c^2 and width 50 MeV/c^2; and 15% D_+ wave with mass of 1700 MeV/c^2 and width 150 MeV/c^2.

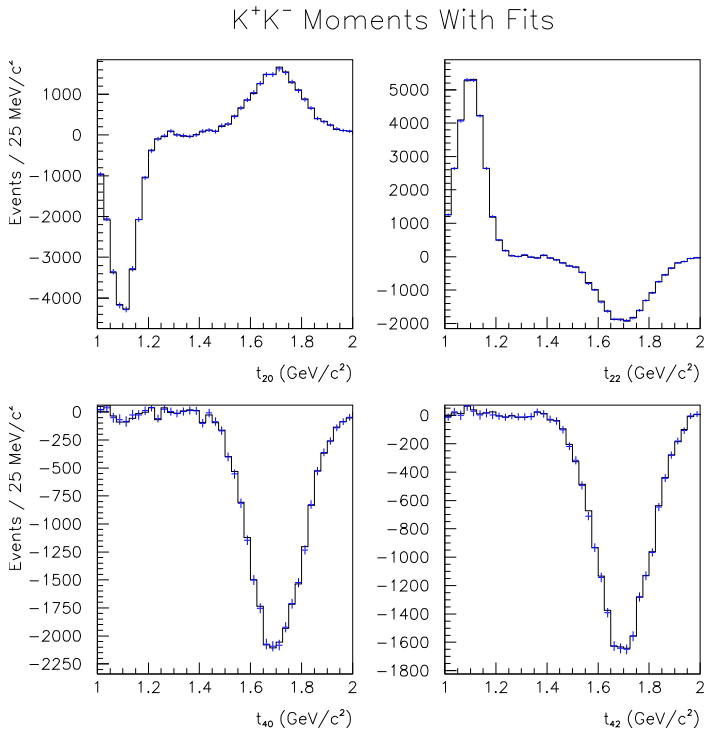

Figure 9.8: The generated moments corresponding to the K^+K^- test events. The blue points are the results of a likelihood fit with perfect detector acceptance.

reproduce the moments well.

Sending the generated K^+K^- events through the detector and reconstructing the events using the same reconstruction routines as were used for the ordinary data, one can get a sense of the effects of the detector acceptance on the moments. Figure 9.9 shows the moments as they were reconstructed. Notice the dramatic effects of the detector acceptance (compare figures 9.8 and 9.9).

The moments of the reconstructed data were now measured using both the event by event correction method and the likelihood fits. The results are shown in figure 9.10. Both methods (the red and blue points) result in moments that agree well with the generated moments (the solid black line). The fact that the magnitudes of the measured moments fall somewhat short of the magnitudes of the generated moments in places is due to the poor acceptance regions of the detector where no events at all were reconstructed. Events need to be present in all regions of the detector for the acceptance corrections to be most accurate. Nonetheless, the match between the measured moments and the generated moments appears sufficient. Events were also generated with a lower beam energy (50 to 60 GeV), and the end result of the fitting is comparable.

9.4.4 The Measured Moments

Turning to the actual data and measuring moments by the two methods described above, six moments are found to be nonzero: t_{00}, t_{11}, t_{20}, t_{21}, t_{40}, and t_{60}. Figures 9.11 and 9.12 show the results for K^+K^- events with beam energies between 70 and 100 GeV. The blue points are the results of the likelihood fit and the red points are obtained by

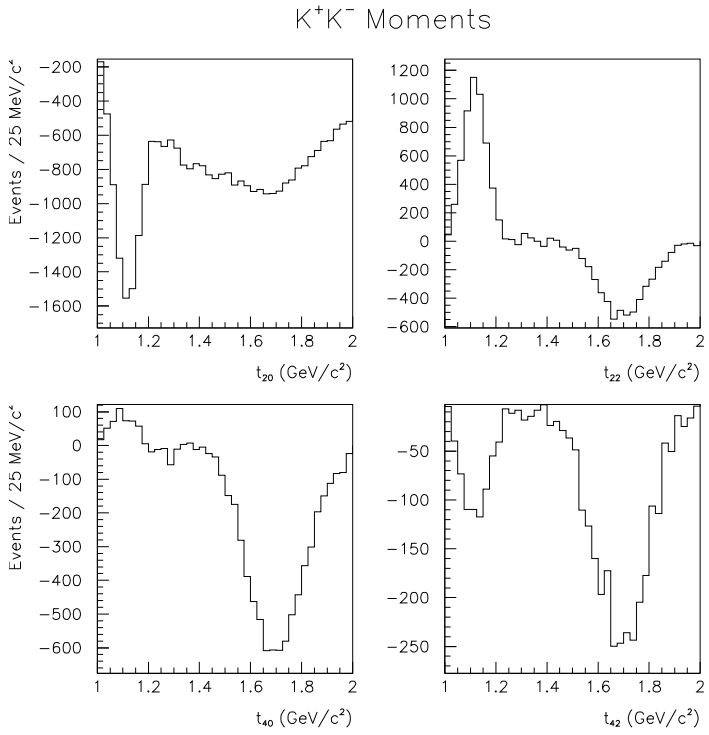

Figure 9.9: The reconstructed moments of the test simulation. This figure shows the dramatic effects of the finite detector acceptance (compare to figure 9.8).

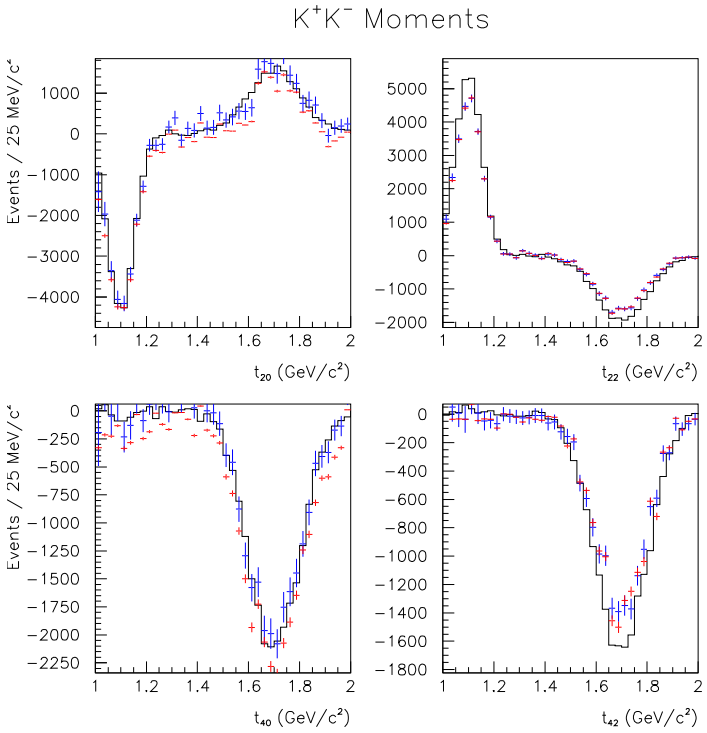

Figure 9.10: The measured moments of the test simulation. The solid black lines are the generated moments; the red points are the results of event by event acceptance corrections; and the blue points are the results of the likelihood fits. There is good agreement between the measured moments and the generated moments. The discrepancies are due to acceptance regions with no reconstructed events.

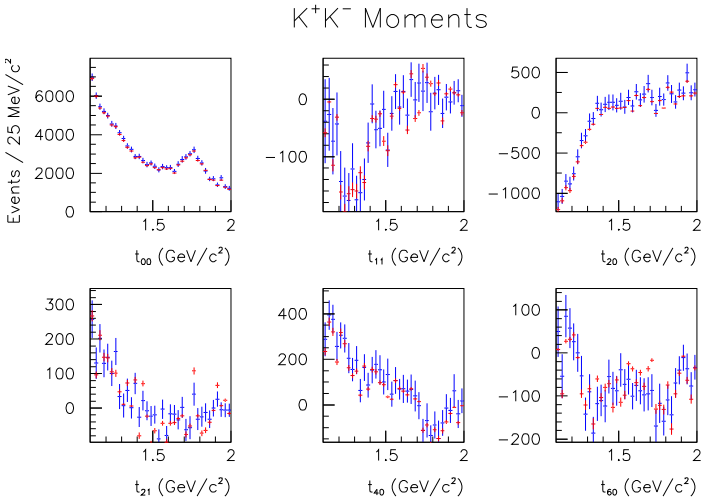

Figure 9.11: Moments of the K^+K^- data in the beam energy bin from 70 to 100 GeV. The red points are event by event corrected moments; the blue points are the moments resulting from the likelihood fit.

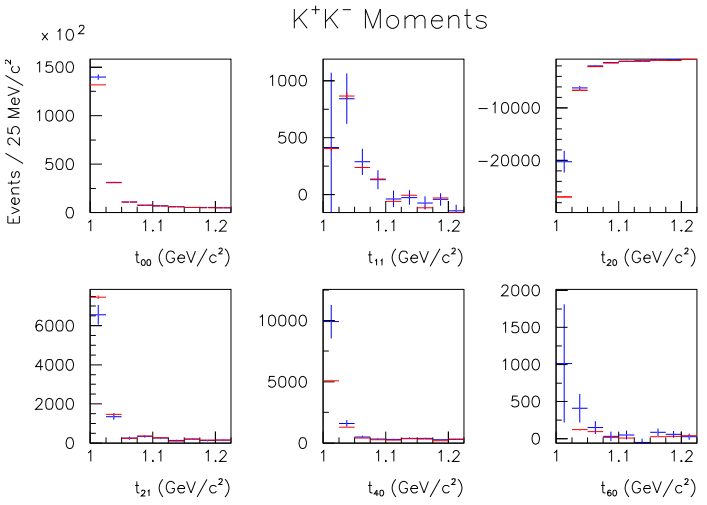

Figure 9.12: Moments of the K^+K^- data in the beam energy bin from 70 to 100 GeV showing the $\phi(1020)$ mass region. The red points are event by event corrected moments; the blue points are the moments resulting from the likelihood fit.

weighting each event. The two methods agree nicely.

Several things should be noticed. First, the t_{20} moment, where a spin-1 object should be most prominent, goes to zero above masses of around 1400 MeV/c^2. There is certainly no signal around 1750 MeV/c^2. Second, the t_{40} moment, which ought to consist of only spin-2 waves, contains definite structure. In fact, the $K^+K^-(1750)$ signal appears clearly here. The sign of the signal indicates that the $K^+K^-(1750)$ is composed of the wave $D^2_- + D^2_+$ (see the above equation for t_{40}). Third, there is structure in t_{60}. This moment, however, corresponds to the spherical harmonic $Y^0_6 \propto \cos^6\theta$, which peaks sharply in the extremes of $\cos\theta$, i.e., $\cos\theta = \pm 1$. It is precisely in this region that the acceptance is unreliable, and thus there is good reason to believe the structure in t_{60} is a spurious effect of the detector acceptance. The above observations point most towards a $J^{PC} = 2^{++}$ interpretation of the $K^+K^-(1750)$, agreeing with the conclusion of section 9.3.

Looking at the $\phi(1020)$ signal in these same moments by extending the mass range of the plots (see figure 9.12) serves as a reminder of our acceptance difficulties. While the $\phi(1020)$ appears very clearly in the t_{20} moment as it ought to, there is also feed-through into the t_{40} moment, which ought to contain nothing spin-1. Still, the $\phi(1020)$ does appear prominently in the nominal moment. The signal in the t_{40} moment at 1750 MeV/c^2 is likely not due to feed-through since no structure at all is observed in t_{20}.

Summing up the fitted moments according to the expansion of the angular distribu-

tion (equation 9.10), one can look at the resulting $\cos\theta$ distributions. These distributions can be compared to the $\cos\theta$ distribution obtained from event by event weighting. The comparison is shown in figure 9.13, where the blue points are from the summed fitted moments and the red points are obtained from event by event weighting.

The same procedures for measuring moments can be followed for K^+K^- events with beam energies between 40 and 70 GeV. The results are shown in figures 9.14, 9.15, and 9.16. The basic structure of the moments (figure 9.14) is substantially the same as in the higher beam energy bin, although the $K^+K^-(1750)$ signal in the t_{40} moment is much less clear, and there is also structure in the t_{20} moment. The signal, however, is cleanest in the beam energy bin from 70 to 100 GeV; the signal to background is best in this region (see chapter 8); and the efficiency as a function of beam energy is most constant in this region (see chapter 6). Thus, there are good reasons to give priority to the moments with beam energies from 70 to 100 GeV over those from 40 to 70 GeV.

Figure 9.15 shows that the $\phi(1020)$ problems persist in the lower beam energy bin. Figure 9.16 shows the $\cos\theta$ distributions in the lower beam energy bin. Notice the substantial difference in $\cos\theta$ distributions in the $K^+K^-(1750)$ sidebands between the lower and higher beam energy bins (figures 9.16 and 9.13), indicating that the sideband production is changing with beam energy.

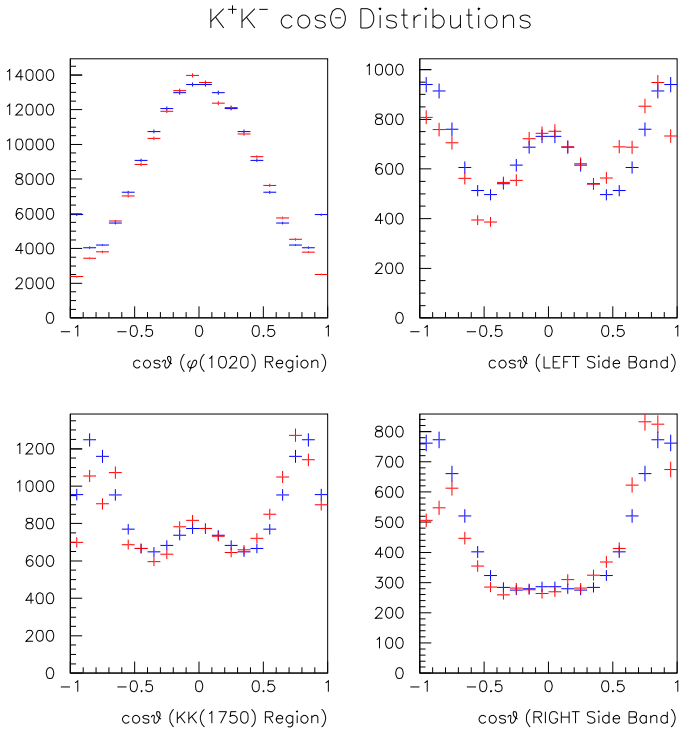

Figure 9.13: The $\cos\theta$ distributions in the beam energy bin from 70 to 100 GeV. The red points are event by event corrected distributions; the blue points are obtained by summing the fitted moments according to equation 9.10.

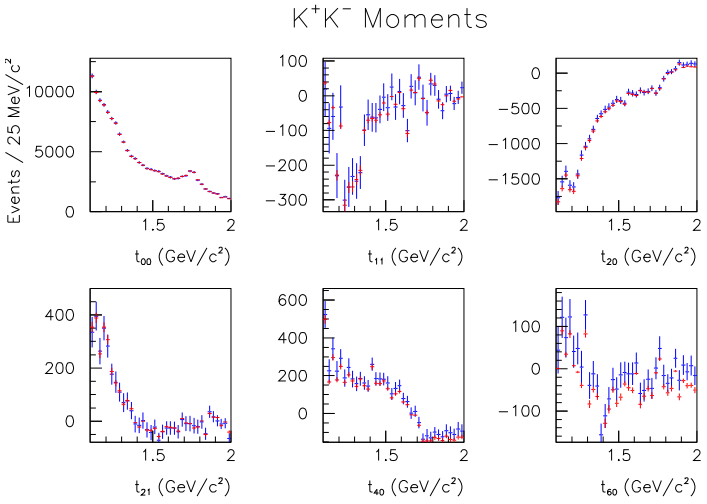

Figure 9.14: Moments of the K^+K^- data in the beam energy bin from 40 to 70 GeV. The red points are event by event corrected moments; the blue points are the moments resulting from the likelihood fit.

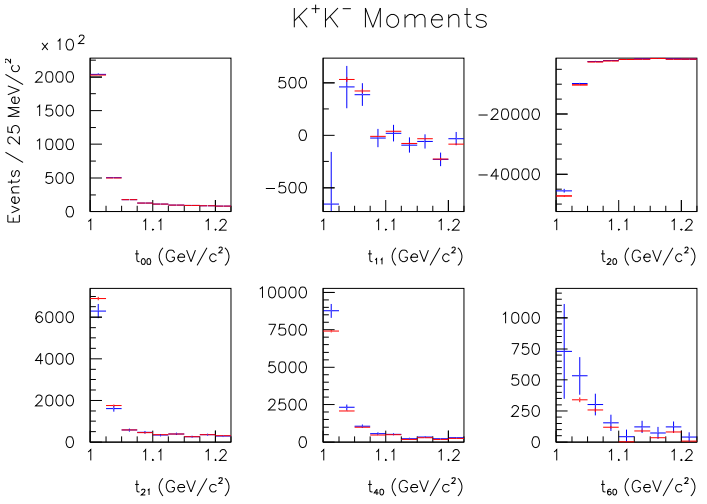

Figure 9.15: Moments of the K^+K^- data in the beam energy bin from 40 to 70 GeV showing the $\phi(1020)$ mass region. The red points are event by event corrected moments; the blue points are the moments resulting from the likelihood fit.

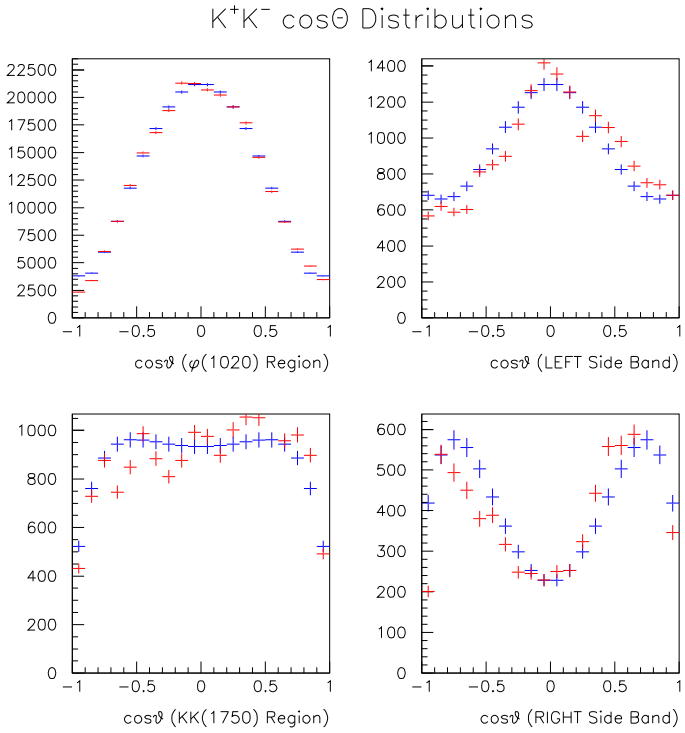

Figure 9.16: The $\cos\theta$ distributions in the beam energy bin from 40 to 70 GeV. The red points are event by event corrected distributions; the blue points are obtained by summing the fitted moments according to equation 9.10.

9.5 Discussion

While uncertainties in the beam direction and non-uniform acceptances in the FOCUS detector have rendered a full partial wave analysis of the K^+K^- final state impossible, several suggestive results have come from a more limited angular analysis. The $\cos\theta$ distribution obtained by fitting the $K^+K^-(1750)$ signal in different $\cos\theta$ bins (figure 9.6) indicates a $J^{PC} \neq 1^{--}$ for the $K^+K^-(1750)$, and in fact points towards a 2^{++} interpretation. This conclusion is backed up by a moments analysis (figure 9.11), where the $K^+K^-(1750)$ appears most strongly in the t_{40} moment, a moment that consists entirely of D-waves. The t_{20} moment, where P-waves are expected to be prominent, appears to die away for masses greater than $1500\,\mathrm{MeV/c^2}$.

Chapter 10

Conclusion

The FOCUS photoproduction experiment at Fermilab has observed a low-p_T enhancement at a mass near 1750 MeV/c^2 in the exclusive photoproduction of K^+K^- pairs. Using a large data sample that included a $K^+K^-(1750)$ yield of $11{,}700 \pm 480$ events, we have made the most accurate determination of the mass and width of the $K^+K^-(1750)$ to date:

$$\mathrm{M} = 1753.5 \pm 1.5 \pm 2.3\,\mathrm{MeV/c^2}$$

$$\Gamma = 122.2 \pm 6.2 \pm 8.0\,\mathrm{MeV/c^2}.$$

We have also placed tight limits on the $K^+K^-(1750)$ branching ratio to two different K^*K final states:

$$\frac{\Gamma(K^+K^-(1750) \to \overline{K}^{*0}K^0 \to K^-\pi^+K_S + c.c.)}{\Gamma(K^+K^-(1750) \to K^+K^-)} < 0.065 \text{ at } 90\% \text{ C.L.}$$

$$\frac{\Gamma(K^+K^-(1750) \to K^{*+}K^- \to K_S\pi^+K^- + c.c.)}{\Gamma(K^+K^-(1750) \to K^+K^-)} < 0.183 \text{ at } 90\% \text{ C.L.}$$

Studying the production of the $K^+K^-(1750)$, we have found the t' distribution to fall exponentially, $ae^{-bt'}$, with a slope steeper than:

$$b = 69.2 \pm 2.1\,\text{GeV}^{-2}\text{c}^2.$$

Backed by nearly two orders of magnitude more signal events than any previous observation, we have argued that the interpretation of this $K^+K^-(1750)$ state must be reconsidered. The standard interpretation, that it is the $\phi(1680)$, cannot hold for two reasons. First, the FOCUS $K^+K^-(1750)$ mass of $1753.5 \pm 1.5 \pm 2.3$ MeV/c^2 is dramatically inconsistent with 1680 MeV/c^2. Second, the $\phi(1680)$ decays dominantly to K^*K, whereas FOCUS finds the $K^+K^-(1750)$ dominantly in K^+K^-.

In addition to questioning the usual interpretation of the $K^+K^-(1750)$, we have been able to make significant progress in laying the groundwork for a future interpretation, despite several limitations imposed by the FOCUS detector. First, we have shown that the energy dependence of the production of the $K^+K^-(1750)$ differs from the energy dependence associated with diffractively photoproduced vector mesons. The ratio of $K^+K^-(1750)$ to $\phi(1020)$ production more than doubles between photon beam energies of 50 and 100 GeV. Second, two independent angular analyses are both inconsistent with a $J^{PC} = 1^{--}$ assignment for the quantum numbers of the $K^+K^-(1750)$. While neither can be taken as definitive, both point towards a 2^{++} assignment. Furthermore,

a $J^{PC} \neq 1^{--}$ is consistent with the non-observation of any enhancement in K^+K^- at $1750\,\mathrm{MeV/c^2}$ in e^+e^- annihilation experiments.

The case of the $K^+K^-(1750)$ is one among several instances of exclusive photoproduction that is yet to be understood. It is hoped that this analysis can eventually be combined with others so that a more comprehensive picture of this important production mechanism can begin to emerge.

Bibliography

Bibliography

[1] F. Close, M. Marten, and C. Sutton. *The Particle Odyssey: A Journey to the Heart of Matter.* Oxford University Press, 2002.

[2] D. H. Perkins. *Introduction to High Energy Physics.* Addison-Wesley Publishing Company, Inc., 1987.

[3] G. L. Kane. *Modern Elementary Particle Physics.* Addison-Wesley Publishing Company, Inc., 1993.

[4] M. E. Peskin and D. V. Schroeder. *An Introduction to Quantum Field Theory.* Perseus Books, Cambridge, Massachusetts, 1995.

[5] C. Quigg. *Gauge Theories of the Strong, Weak, and Electromagnetic Interactions.* Advanced Book Program. Addison-Wesley Longman, Inc., Reading, MA, 1997.

[6] M. Riordan. *The Hunting of the Quark: a True Story of Modern Physics.* Simon and Schuster, New York, New York, 1987.

[7] A. Pickering. *Constructing Quarks: A Sociological History of Particle Physics.* Edinburgh University Press, Edinburgh, 1984.

[8] R. N. Cahn and G. Goldhaber. *The Experimental Foundations of Particle Physics.* Cambridge University Press, Cambridge, 1989.

[9] J. J. J. Kokkedee. *The Quark Model.* Benjamin, New York, New York, 1969.

[10] M. Alston et al. Resonance in the $K\pi$ system. *Physical Review Letters*, 6:300, 1961.

[11] M. Gell-Mann and Y. Ne'eman, editors. *The Eightfold Way.* W. A. Benjamin, New York and Amsterdam, 1964.

[12] V. E. Barnes et al. Observation of a hyperon with strangeness minus three. *Physical Review Letters*, 12:204, 1964.

[13] S. Godfrey and J. Napolitano. *Reviews of Modern Physics*, 71:1411, 1999.

[14] S. Godfrey and N. Isgur. *Physical Review D*, 32:189, 1985.

[15] S. Godfrey. *Physical Review D*, 31:2375, 1985.

[16] S. Godfrey and N. Isgur. *Physical Review D*, 34:899, 1986.

[17] J. E. Augustin et al. Discovery of a narrow resonance in e^+e^- annihilation. *Physical Review Letters*, 33:1406, 1974.

[18] J. J. Aubert et al. Experimental observation of a heavy particle J. *Physical Review Letters*, 33:1404, 1974.

[19] R. Brandelik et al. Evidence for planar events in e^+e^- annihilation at high energies. *Physics Letters B*, 86:243, 1979. (TASSO Collaboration).

[20] D. P. Barber et al. Discovery of three-jet events and a test of Quantum Chromodynamics at PETRA. *Physical Review Letters*, 43:830, 1979. (MARK J Collaboration).

[21] Ch. Berger et al. Evidence for gluon bremsstrahlung in e^+e^- annihilation at high energies. *Physics Letters B*, 86:418, 1979. (PLUTO Collaboration).

[22] W. Bartel et al. Observation of planar three-jet events in e^+e^- annihilation and evidence for gluon bremsstrahlung. *Physics Letters B*, 91:142, 1980. (JADE Collaboration).

[23] K. G. Wilson. *Physical Review D*, 10:2445, 1974.

[24] C. Morningstar and M. Peardon. *Physical Review D*, 56:4043, 1997.

[25] C. Morningstar and M. Peardon. hep-lat/9901004, 1999.

[26] T. Barnes. In D. V. Bugg, editor, *Nato Advanced Study Institute on Hadron Spectroscopy and the Confinement Problem*, New York, 1996. Queen Mary and Westfield College London and the University of Swansea, Plenum.

[27] T. Barnes. PhD thesis, Caltech, 1977.

[28] P. Hasenfratz, R. R. Horgan, J. Kuti, and J. M. Richard. *Physics Letters B*, 94:401, 1980.

[29] T. Barnes, F. E. Close, and F. de Viron. *Nuclear Physics B*, 224:241, 1983.

[30] M. S. Chanowitz and S. Sharpe. *Physics Letters B*, 132:413, 1983.

[31] C. DeTar and J. Donoghue. *Annual Review of Nuclear and Particle Science*, 33:325, 1983.

[32] D. Horn and J. Mandula. *Physical Review D*, 17:898, 1978.

[33] N. Isgur, R. Kokoski, and J. Paton. *Physical Review Letters*, 54:869, 1985.

[34] N. Isgur and J. Paton. *Physics Letters B*, 124:247, 1983.

[35] N. Isgur and J. Paton. *Physical Review D*, 31:2910, 1985.

[36] A. Le Yaouanc, L. Oliver, O. Pene, and J. C. Raynal. *Physical Review D*, 8:2223, 1973.

[37] A. Le Yaouanc, L. Oliver, O. Pene, and J. C. Raynal. *Physical Review D*, 9:1415, 1974.

[38] A. Le Yaouanc, L. Oliver, O. Pene, and J. C. Raynal. *Physical Review D*, 11:1272, 1975.

[39] T. Barnes, F. E. Close, P. R. Page, and E. S. Swanson. *Physical Review D*, 55:4157, 1997.

[40] T. Barnes, N. Black, and P. R. Page. *Physical Review D*, 68:054014, 2003.

[41] G. Adams et al. *Physical Review Letters*, 81:5760, 1998. (E852 Collaboration).

[42] D. Barberis et al. *Physics Letters B*, 397:339, 1997. (WA102 Collaboration).

[43] R. P. Feynman. *Photon-Hadron Interactions.* Advanced Book Program. Addison-Wesley Longman, Inc., Reading, MA, 1998.

[44] H. Primakoff. *Physical Review*, 81:899, 1951.

[45] F. V. Murphy and D. E. Yount. *Scientific American*, 225:94, July 1971.

[46] J. J. Sakurai. *Annals of Physics*, 11:1, 1960.

[47] J. J. Sakurai. *Physical Review Letters*, 22:981, 1969.

[48] T. H. Bauer, R. D. Spital, and D. R. Yennie. *Reviews of Modern Physics*, 50(2):261, April 1978.

[49] F. J. Gilman, J Pumplin, A. Schwimmer, and L. Stodolsky. *Physics Letters B*, 31:387, 1970.

[50] A. T. Doyle. Diffraction: QCD effects in colour singlet exchange. In *25th SLAC Summer Institute*, August 1997. (hep-ex/9712027).

[51] J. A. Crittendon. hep-ex/9704009, 1997.

[52] J. Ballam et al. *Nuclear Physics B*, 76:375, 1974.

[53] H. Alvensleben et al. *Physical Review Letters*, 26:273, 1971.

[54] G. Alexander et al. *Physics Letters B*, 57:487, 1975.

[55] D. Aston et al. *Nuclear Instruments and Methods Physics Results*, 197:287, 1982. (Omega Collaboration).

[56] D. P. Barber et al. *Nuclear Instruments and Methods*, 155:353, 1978. (LAMP2 Collaboration).

[57] K. Abe et al. *Physical Review D*, 30:1, 1984. (SLAC Hybrid Collaboration).

[58] J. Busenitz et al. *Physical Review D*, 40:1, 1989. (E401 Collaboration).

[59] D. Aston et al. *Nuclear Physics B*, 189:15, 1981. (Omega Collaboration).

[60] M. Atkinson et al. *Physics Letters B*, 127:132, 1983. (Omega Collaboration).

[61] D. P. Barber et al. *Zeitschrift fur Physik C*, 4:169, 1980. (LAMP2 Collaboration).

[62] D. Aston et al. *Physics Letters B*, 92:215, 1980. (Omega Collaboration).

[63] M. Atkinson et al. *Zeitschrift fur Physik C*, 26:499, 1985. (Omega Collaboration).

[64] A. Donnachie and Mirzaie. *Zeitschrift fur Physik C*, 33:407, 1987.

[65] A. B. Clegg and A. Donnachie. *Zeitschrift fur Physik C*, 34:257, 1987.

[66] A. B. Clegg and A. Donnachie. *Zeitschrift fur Physik C*, 40:313, 1988.

[67] A. B. Clegg and A. Donnachie. *Zeitschrift fur Physik C*, 45:677, 1990.

[68] A. B. Clegg and A. Donnachie. *Zeitschrift fur Physik C*, 62:455, 1994.

[69] A. Antonelli et al. *Physics Letters B*, 212:133, 1988. (DM2 Collaboration).

[70] A. Abele et al. *Physics Letters B*, 391:191, 1997. (Crystal Barrel Collaboration).

[71] D. Aston et al. *Physics Letters B*, 92:211, 1980. (Omega Collaboration).

[72] M. Atkinson et al. *Nuclear Physics B*, 243:1, 1984. (Omega Collaboration).

[73] J. Brau et al. *Physical Review D*, 37:2379, 1988. (SLAC Hybrid Collaboration).

[74] B. R. Kumar. Technical Report RL-80-060, Rutherford Laboratory, 1980.

[75] K. Hagiwara et al. *Physical Review D*, 66:010001, 2002. (Particle Data Group).

[76] M. Atkinson et al. *Nuclear Physics B*, 231:15, 1984. (Omega Collaboration).

[77] M. Atkinson et al. *Nuclear Physics B*, 229:269, 1983. (Omega Collaboration).

[78] A. Antonelli et al. *Zeitschrift fur Physik C*, 56:15, 1992. (DM2 Collaboration).

[79] D. Aston et al. *Physics Letters B*, 104:231, 1981. (Omega Collaboration).

[80] J. C. Bizot et al. In *International Conference on High Energy Physics*, Madison, WI, 1980.

[81] J. Buon et al. *Physics Letters B*, 118:221, 1982. (DM1 Collaboration).

[82] B. Delcourt et al. *Physics Letters B*, 99:257, 1981.

[83] M. Atkinson et al. *Nuclear Physics B*, 231:1, 1984. (Omega Collaboration).

[84] M. Atkinson et al. *Zeitschrift fur Physik C*, 27:233, 1985. (Omega Collaboration).

[85] D. Bisello et al. *Zeitschrift fur Physik C*, 52:227, 1991. (DM2 Collaboration).

[86] D. Bisello et al. *Zeitschrift fur Physik C*, 39:13, 1988. (DM2 Collaboration).

[87] P. L. Frabetti et al. *Nuclear Instruments and Methods Physics Results A*, 320:519, 1992. (E687 Collaboration).

[88] P. Kasper, R. Currier, P. Garbincius, and J. Butler. Wide band to double band upgrade. Technical Report Technical Report TM-1552, Fermilab, 1988.

[89] J. M. Link et al. *Nuclear Instruments and Methods A*, 484:174, 2002. (FOCUS Collaboration).

[90] E. Vaandering. PhD thesis, University of Colorado, Boulder, January 2000.

[91] J. Link. PhD thesis, University of California, Davis, March 2001.

[92] J. M. Link et al. hep-ex/0204023, 2002.

[93] J. M. Link et al. *Nuclear Instruments and Methods A*, 484:270, 2002. (FOCUS Collaboration).

[94] J. M. Link et al. *Physics Letters B*, 491:232, 2000. (FOCUS Collaboration).

[95] J. M. Link et al. *Physics Letters B*, 545:50, 2002. (FOCUS Collaboration).

[96] H. G. Blundell and S. Godfrey. *Physical Review D*, 53:3700, 1996.

[97] H. G. Blundell, S. Godfrey, and B. Phelps. *Physical Review D*, 53:3712, 1996.

[98] G. J. Feldman and R. D. Cousins. *Physical Review D*, 57:3873, 1998.

[99] W. Koch. Some methods of spin analysis in elementary particle physics. In *Lectures given in the Academic Training Programme of CERN*, 1965.

[100] S. U. Chung. Spin formalisms. In *Lectures given in the Academic Training Programme of CERN*, 1971.

[101] M. E. Rose. *Elementary Theory of Angular Momentum.* Dover Publications; Reprint Edition, April 1995.

[102] Jeffrey L. Gunter. *An Analysis of* $\pi^- p \to \pi^0\pi^0 n$ *at 18*GeV/c. PhD thesis, Indiana University, December 1997.

[103] B. C. Earl. *A study of the centrally produced* K^+K^- *system at the CERN Omega Spectrometer.* PhD thesis, University of Birmingham, March 1999.

[104] K. Gottfried and J. D. Jackson. *Il Nuovo Cimento*, 33:309, 1964.

[105] S. U. Chung and T. L. Trueman. *Physical Review D*, 11:633, 1975.

[106] S. U. Chung. *Physical Review D*, 56:7299, 1997.

[107] F. James. *MINUIT: Function Minimization and Error Analysis.* CERN Computing and Networks Divison, Geneva, Switzerland, 94.1 edition, 2000.

Appendix

Appendix A

The Standard Model of Particle Physics

The Standard Model is the currently accepted theory of the fundamental particles and their interactions. Despite sporadic complaints over a few of its unattractive features, like having 18 free parameters, the Standard Model has had success after success over the last twenty years of its existence. This short appendix will simply list its main components.

Within the Standard Model, there are two broad categories of particles. The fundamental fermions (fermions are particles with fractional spin) are considered to be the matter, the stuff of the universe. For example, the quarks in an atomic nucleus and the electrons surrounding it belong to this category. The fundamental bosons (bosons are particles with integer spin), on the other hand, are responsible for the forces between

the matter particles. For example, the quarks in the nucleus are held together by gluons and electrons are bound to the nucleus by photons.

The interactions between matter particles take place through the exchange of the fundamental bosons. These interactions are described by the Lagrangians of the Standard Model, equations that specify rules for calculating things like the probabilities for certain reactions to occur, referred to as cross sections.

A.1 The Fundamental Particles

According to the Standard Model, there are twelve fundamental matter particles (see tables A.1 and A.2) – six quarks (the up, down, strange, charm, bottom and top quarks) and six leptons (the electron, muon, tau, and a neutrino associated with each). All of the elements of the periodic table can be built from combinations of only three of these twelve: the up quark, the down quark, and the electron. An oxygen atom, for example, has eight electrons surrounding a nucleus of eight protons and eight neutrons. Protons are built from two up quarks and one down quark; and neutrons are two down quarks and one up quark.

Because of the strength of the forces between them (the strong force), quarks are confined to exist in composites. A combination of a quark and an antiquark is a meson (e.g., a pion or kaon), and a combination of three quarks is a baryon (e.g., a proton or neutron). While the vast majority of the matter we encounter in everyday life consists only of up and down quarks, the other four quarks are equally as fundamental. The

Table A.1: Properties of the quarks.

Name	Symbol	Mass	Charge
Up Quark	u	$\approx 5\,\mathrm{MeV/c^2}$	$+2/3$
Down Quark	d	$\approx 10\,\mathrm{MeV/c^2}$	$-1/3$
Strange Quark	s	$\approx 100\,\mathrm{MeV/c^2}$	$-1/3$
Charm Quark	c	$\approx 1.5\,\mathrm{GeV/c^2}$	$+2/3$
Bottom Quark	b	$\approx 4.7\,\mathrm{GeV/c^2}$	$-1/3$
Top Quark	t	$\approx 170\,\mathrm{GeV/c^2}$	$+2/3$

Table A.2: Properties of the leptons.

Name	Symbol	Mass	Charge
Electron	e	$0.511\,\mathrm{MeV/c^2}$	-1
Muon	μ	$105.6\,\mathrm{MeV/c^2}$	-1
Tau	τ	$1.777\,\mathrm{GeV/c^2}$	-1
Electron Neutrino	ν_e	$< 3\,\mathrm{eV/c^2}$	0
Muon Neutrino	ν_μ	$< 0.17\,\mathrm{MeV/c^2}$	0
Tau Neutrino	ν_τ	$< 18\,\mathrm{MeV/c^2}$	0

Table A.3: Properties of the gauge bosons.

Name	Symbol	Mass	Charge
Photon	γ	0	0
W Boson	$W^{\pm}$	$80.4\,\mathrm{GeV/c^2}$	± 1
Z Boson	Z^0	$91.19\,\mathrm{GeV/c^2}$	0
Gluon	g	0	0

essential difference is only in their mass.

The lepton category of the fundamental particles consists of three negatively charged particles, of which the electron is prototypical, and their three nearly massless, very weakly interacting neutral partners, the neutrinos. The muon and tau differ from the electron only in mass. Neutrinos are only emitted during weak processes, and are extraordinarily difficult to detect.

A.2 The Fundamental Forces

The fundamental particles interact through four different forces. Probably the most familiar of the forces is gravity, the force of attraction between massive bodies. Because of the smallness of the masses of the fundamental particles, however, the force of gravity between any of them is negligible. It is hoped that gravity will someday be described by a theory unifying it to the other three forces, but the Standard Model does not incorporate it. The forces of the Standard Model are all described by the exchange of force-carrying particles, the gauge bosons (see table A.3).

Electromagnetism is the force responsible for the repulsion between like charges, the

attraction between unlike charges, the deflection of charged particles in magnetic fields, and so on. In the Standard Model, the force is due to the exchange of photons, which interact with any charged body. In addition, in Quantum Electrodynamics (QED), the Standard Model theory of electromagnetism, photons can convert to electrons and positrons, an electron can emit a photon, electrons and positrons can annihilate into photons, etc.

The strong force acts only on quarks, and is due to the exchange of gluons. Like the electric charge for electromagnetism, the strong force proceeds through a charge of its own, the "color" charge. But unlike electromagnetism, where the photon has no electric charge of its own, gluons do carry color charge, allowing them to interact among themselves and thus creating a much more complex situation. The strong force binds quarks tightly into hadrons, so tightly that the quarks never appear unbound. The Standard Model theory of the strong force is Quantum Chromodynamics (QCD).

Finally, the weak force affects all of the fundamental particles. It is carried by the $W^{\pm}$ and Z^0 bosons. Nuclear beta decay is the most familiar example of this force, where one of the down quarks of a neutron converts to an up quark by emitting a W^-, which subsequently decays to an electron and an electron antineutrino. The Standard Model theory of the weak force and QED are united into a single theory, the electroweak theory, by introducing a Higgs Boson. The search for the Higgs Boson, the last of the Standard Model particles to be experimentally undiscovered, is one of the major efforts of contemporary high energy physics.

A.3 Lagrangians

The mathematical structure of the Standard Model is contained in a series of Lagrangians. For example, the QED Lagrangian can be written as:

$$\mathcal{L}_{QED} = \overline{\psi_i}(i\gamma^\mu \partial_\mu - qA_\mu \gamma^\mu - m)\psi - \frac{1}{4}F_{\mu\nu}F^{\mu\nu}, \tag{A.1}$$

where

$$F^{\mu\nu} \equiv \partial^\nu A^\mu - \partial^\mu A^\nu. \tag{A.2}$$

Here, ψ represents a particle with charge q, and A_μ is the photon. The first term describes how the charged particle propagates through space; the second term describes the propagation of the photon; and the last term holds information about how the charged particle and photon interact with each other. By following a series of rules, the Feynman rules, the Lagrangian can be used to calculate cross sections. All of the physics information of the Standard Model is contained in its Lagrangians.

Appendix B

The Kinematics of Exclusive Photoproduction

Several important kinematic variables continuously recur within exclusive photoproduction. This appendix gathers their definitions in one place.

Combining the photon beam energy (E_{BEAM}) with the mass of the stationary target nucleon (M_N) gives a center of mass energy, $\sqrt{s}$:

$$\sqrt{s} = (M_N^2 + 2M_N E_{BEAM})^{\frac{1}{2}}. \tag{B.1}$$

A photon beam of 50 GeV incident upon a proton, for instance, has $\sqrt{s} = 9.73$ GeV, and a photon beam of 100 GeV has $\sqrt{s} = 13.7$ GeV.

The transverse momentum (p_T) of a resonance measured with respect to the photon

beam direction often contains information about the production of the resonance. A related measure of the amount of interaction between the beam and the target is the kinematic variable t:

$$t \equiv (P_{BEAM} - P_{res})^2, \tag{B.2}$$

where P_{BEAM} and P_{res} are the four-momenta of the photon beam and the resonance produced, respectively. As it is defined, t is negative for exclusive photoproduction. For convenience, a new variable t' is calculated in the overall center of mass based on t:

$$t' \equiv |t| - |t|_{min}, \tag{B.3}$$

which, for most production processes, follows an exponential distribution, $ae^{-bt'}$. For high energy photon beams such as the FOCUS beam, this definition of t' reduces to:

$$t' \approx p_T^2. \tag{B.4}$$

For resonance decays, the Gottfried-Jackson coordinate system is often used in exclusive photoproduction (figure B.1). Here, the z-axis is the photon beam direction in the rest frame of the decaying resonance; the y-axis is the cross product of the beam direction and the resonance direction in the overall center of mass (i.e., normal to the production plane); and the x-axis is $\hat{y} \times \hat{z}$. The polar angle (θ) and the azimuthal angle (ϕ) of one of the decay products measured in this coordinate system completely describe a two-body decay.

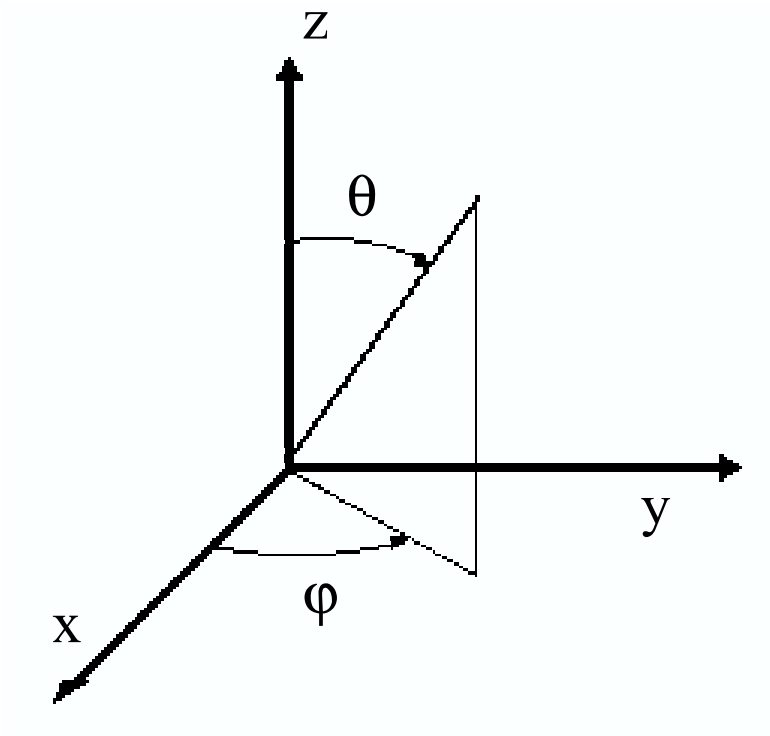

Figure B.1: The Gottfried-Jackson coordinate system for resonance decays. The z-axis is the photon beam direction in the rest frame of the decaying resonance; the y-axis is the cross product of the beam direction and the resonance direction in the overall center of mass (i.e., normal to the production plane); and the x-axis is $\hat{y} \times \hat{z}$.

Vita

Ryan Edward Mitchell was born in Chicago, IL on August 18, 1975. After attending high school in Springfield, IL, he earned a B.S. in mathematics and a B.A. in physics from North Central College in 1997. While attending North Central College, Ryan began conducting research at the Fermi National Accelerator Laboratory, doing his undergraduate honors thesis with Dr. Herman B. White, entitled "Evolution of the Standard Model."

After graduating, Ryan began his graduate studies in physics at the University of Tennessee in the fall of 1997. He passed the doctoral qualifying examinations in the summer of 1999 and became involved in the BTeV and FOCUS high energy particle physics experiments at Fermilab. Ryan contributed to the design of the BTeV tracking system and K_S reconstruction algorithms, performing extensive Monte Carlo detector simulations. In the FOCUS experiment, Ryan soon became interested in the massive light quark sample of events and its potential to contribute to our understanding of photoproduction and light meson spectroscopy. He wrote his doctoral dissertation on this subject at the University of Tennessee in the fall of 2003 under the direction of Dr. Thomas Handler.

Ryan intends to continue his studies of photoproduction and experimental light meson spectroscopy over the next several years.